DEVELOPMENT OF DETECTORS FOR SPACE MISSIONS AND BALLOON FLIGHTS

A Thesis

Submitted for the Degree of

Doctor of Philosophy (Technology)

Submitted by

AMBILY S

Department of Applied Optics & Photonics

University College of Technology

University of Calcutta

November 2018

To my family, friends, and

teachers

List of Publications

1. Refereed journal articles

(a) **Development of data acquisition methods for an FPGA-based photon counting detector** - ***S. Ambily***, *Mayuresh Sarpotdar, Joice Mathew, A. G. Sreejith, K. Nirmal, Ajin Prakash, Margarita Safonova, and Jayant Murthy* , Journal of Astronomical Instrumentation, Volume 6, Issue 1, 1750002, 2017.[1]

(b) **Wide-field ultraviolet imager for astronomical transient studies** - *Joice Mathew,* ***S. Ambily****, Ajin Prakash, Mayuresh Sarpotdar, K. Nirmal, A. G. Sreejith, Margarita Safonova, Jayant Murthy, and Noah Brosch* , Experimental Astronomy, Volume 45, Issue 2, 201-218, 2018.[2]

(c) **Overview of high-altitude balloon experiments at the Indian Institute of Astrophysics**- *Margarita Safonova, Akshata Nayak, A. G. Sreejith, Joice Mathew, Mayuresh Sarpotdar,* ***S. Ambily****, K. Nirmal, Sameer Talnikar, Shripathy Hadigal, Ajin Prakash, and Jayant Murthy*, Astronomical and Astrophysical Transactions, Volume 29, Issue 3, 397-426, 2016.[3]

(d) **The PESIT-IIA Observatory for the Night Sky (PIONS): An ultraviolet telescope to observe variable sources** - ***S. Ambily****, B.G. Nair, M. Sarpotdar, J. Mathew, J. Murthy, V. K. Agrawal, S. Nagabhushanam, S. Jeeragal, Sreejith A. G., D. A. Rao, K. Nirmal, and M. Safonova*, **In preparation**

2. Refereed conference proceedings

(a) **PIONS: a CubeSat imager to observe variable UV sources** - ***S. Ambily****, J. Mathew, M. Sarpotdar, J. Murthy, V. K. Agrawal,*

[1]Presented in Chapter 2
[2]Presented in Chapter 3
[3]Presented in Chapter 3

S. Nagabhushanam, S. Jeeragal, D. A. Rao, K. Nirmal, Sreejith A. G., M. Safonova, and B.G. Nair, Proc. SPIE 10699, Space Telescopes and Instrumentation 2018: Ultraviolet to Gamma Ray, 106993E, 2018.[4]

(b) **Near UV imager with an MCP-based photon counting detector** - ***S. Ambily***, *Joice Mathew, Mayuresh Sarpotdar, A. G. Sreejith, K. Nirmal, Ajin Prakash, Margarita Safonova, and Jayant Murthy*, Proc. SPIE 9905, Space Telescopes and Instrumentation 2016: Ultraviolet to Gamma Ray, 990530, 2016.

(c) **Development of an FPGA based photon counting detector for balloon flights** - ***S. Ambily***, *J. Mathew, M. Safonova, and J. Murthy*, IEEE Xplore: Proceedings on the Workshop on Recent Advances in Photonics, 2015.

(d) **Balloon UV experiments for astronomical and atmospheric observations** - *A. G. Sreejith, Joice Mathew, Mayuresh Sarpotdar, Nirmal K.,* ***Ambily S.****, Ajin Prakash, Margarita Safonova, and Jayant Murthy*, Proc. SPIE 9908, Ground-based and Airborne Instrumentation for Astronomy VI, 99084E, 2016.

3. Journal articles not part of this thesis

(a) **Pointing system for the balloon-borne astronomical payloads** - *K. Nirmal, A. G. Sreejith, Joice Mathew, Mayuresh Sarpotdar,* ***Ambily Suresh****, Ajin Prakash, Margarita Safonova, and Jayant Murthy*, Journal of Astronomical Telescopes, Instruments and Systems, Vol. 02, issue. 04, 047001, 2016.

(b) **A software package for evaluating the performance of a star sensor operation** - *Mayuresh Sarpotdar, Joice Mathew, A. G. Sreejith, K. Nirmal,* ***S. Ambily****, Ajin Prakash, Margarita Safonova, and Jayant Murthy*, Experimental Astronomy, Vol 43, Issue 1, pp 99–117, February 2017.

[4]Presented in Chapter 4

(c) **Prospect for UV observations from the Moon. II. Instrumental design of an ultraviolet imager LUCI** - *Joice Mathew, Ajin Prakash, Mayuresh Sarpotdar, A. G. Sreejith, K. Nirmal,* ***S. Ambily****, Margarita Safonova, Jayant Murthy, and Noah Brosch*, Astrophysics and Space Science, Vol 362, Issue 2, pp 11, February 2017.

(d) **Measurement of limb radiance and trace gases in UV over tropical region by balloon-borne instruments - Flight validation and initial results** - *A. G. Sreejith, Joice Mathew, Mayuresh Sarpotdar, K. Nirmal,* ***S. Ambily****, Ajin Prakash, Margarita Safonova, and Jayant Murthy*, Atmos. Meas. Tech. Discuss., amt-2016-98, 2016.

Abstract

We are developing compact astronomical payloads for ultraviolet (UV) observations from CubeSats and high altitude balloons. It is important to have a highly sensitive, low noise detector in the UV region where the incoming photons are very few. Micro Channel Plate (MCP) based photon counting detectors are widely used in UV astronomy due to their low noise levels, high sensitivity, and large area.

The first part of the thesis describes the design, fabrication, and characterization of a photon counting, intensified CMOS (iCMOS) detector. The detector consists of a Z-stack, 40 mm MCP from Photek with an S20 photocathode and a phosphor screen anode. The readout system uses off-the-shelf components for the focusing optics, image sensor, and backend electronics. The heart of the electronics is a Field Programmable Gate Array (FPGA) board that controls the input signals from the CMOS and interfaces the output data to storage and telemetry. The FPGA performs real-time data processing as well, including the identification of actual photon events and their centroiding with sub-pixel accuracy.

The detector is being used as the back end instrument of two of our UV payloads on a balloon platform above 40 km. One of the instruments is fiber-fed, near UV spectrograph for atmospheric observations in the 250 – 400 nm region. The detector also flies on a wide-field UV imager for observing solar system objects such as comets and asteroids and other bright UV transients. It is an all-refractive 70 mm telescope in the 250 – 350 nm wavelength range with a 10.8° field of view.

One of the space-flight opportunities for the detector is the PESIT-IIA Observatory for the Night Sky (PIONS), a near UV imaging telescope to be flown on a small satellite. The major scientific goals are to detect and characterize transients such as massive star explosions, stellar flares, and tidal disruption events. The camera has a 150 mm primary aperture with a 3° field of view and images the sky in the 180 – 280 nm region with a 13″ resolution. We can observe targets as faint as 21^{st} magnitude in a 1200 seconds exposure.

We are also working on far UV instruments and detectors, by assembling a bare MCP with a custom-coated, semi-transparent photocathode. The photocathode is fabricated by thin film deposition of CsI crystals on an MgF_2 window. I will also briefly describe the future work on the design and fabrication of an FUV imaging spectrograph and associated technologies.

Contents

List of Figures

List of Tables

Chapter 1

Introduction

1.1 Introduction

The ultraviolet (UV) region which extends from 100 to 4000 Å is one of the richest parts of the electromagnetic spectrum. This band consists of a number of atomic and molecular transitions that provide unique diagnostic tools to understand the Universe from its present state to redshifts of z=2, covering over 75 % of the age of the Universe. There are a number of absorption and emission lines in the UV that help us measure multiple elements in their various ionization states, to trace gas from below 10^2 to 10^7 Kelvins (Tumlinson et al., 2012). This makes UV spectroscopy a vital tool for studying the galaxy formation and evolution, protoplanetary and protostellar disks, and the diffuse gases in the interstellar and intergalactic mediums. The Lyman UV region from 912 – 1216 Å is particularly interesting with some of the most powerful tracers to the local universe that help understand some of the compelling problems in astrophysics ranging from the habitability of exoplanets to the re-ionization of the Intergalactic Matter (IGM). Despite its scientific importance, the UV region is also one of the least explored, mainly due to technological limitations and the difficulties in going to space.

UV observations can provide crucial information about the formation and

evolution of galaxies, from their star formation rate to the level of activity in their Active Galactic Nuclei (AGN). Since galaxies are known to have a black hole at the center, our present knowledge of galaxy evolution can be further strengthened by the knowledge on blackhole evolution, i.e., how they accrete matter and grow through cosmic time and how they influence the galaxy. UV observations are essential in understanding the AGN feedback mechanism as well, by characterizing the inflow and outflow of hot gas into the AGN. X-ray emission from young galaxies at high redshifts will also be seen in UV, which can help us understand the origin and evolution of the universe and create accurate cosmological models.

As missions such as Kepler (Borucki et al., 2010) and TESS (Ricker et al., 2015) are primed to discover a large number and variety of exoplanets, the next step for the astrophysical community is to characterize these planets and discover the ones that are 'Earth-like'. Planets orbiting UV bright stars and white dwarfs are yet to be fully explored, although they can help in understanding solar systems in their early stages of formation, and probe planet formation around massive stars. The UV region also consists of spectral lines that enable us to detect and characterize the existence of metals in stellar disks, indicating the formation of rocky planets. UV observations are also vital in atmospheric studies, for understanding the absorption of stellar energy in its various layers. The large (LUV+FUV)/NUV stellar flux ratios in the HZ around M-dwarfs can have a profound effect on the atmospheric oxygen chemistry of Earth-like planets (France et al., 2013). As biosignature species such as O_2, O_3, H_2O, and CO_2 can also be produced by photochemical effects of the EUV and FUV radiation, characterization of the FUV stellar spectrum is important to distinguish these species from biological sources. UV and X-ray spectra can also indicate the atmospheric mass loss from these planets and be used for characterizing the physical parameters of the planet (Vidal-Madjar et al., 2003).

Surveying the UV sky along with optical follow up observations can also play a vital role in understanding the physics and energy of transients. Tradi-

tionally, transient observations have been done in the high energy domains of X-rays and γ rays and in the longer wavelengths of radio and infrared. With the installation of large aperture telescopes and dedicated survey programs on the ground such as the Palomar Transient Factory (Rau et al., 2009) and Pan-STARRS (Kaiser et al., 2002), the rate of detection of transients has increased in the optical wavelengths. Upcoming facilities such as the Zwicky Transient Facility (Smith et al., 2014) and the Large Synoptic Survey Telescope (Ivezić et al., 2008) are also capable of covering large swaths of the sky at a high cadence, to look for variable sources. It is important to complement these observations with space-based observations, as in most cases the UV transient can be observed much ahead in time and can alert the observations from the ground. There are fascinating science questions that can be answered by a wide field UV survey in both NUV and FUV that can detect and/or study transient phenomena such as gamma ray bursts, novae, supernovae, and flare stars (Sagiv et al., 2014). They can complement detections from current and upcoming facilities in high energy and radio, with further monitoring using ground based telescopes.

1.2 UV Missions

The ultraviolet wavelengths became observable midway through the last century when instruments could be deployed above the Earth's atmosphere. While space-based astronomy poses its own challenges, it also helps mitigate some of the problems of ground-based observations such as atmospheric turbulence and light pollution. As the resolving power of a telescope varies inversely with wavelength, space-based telescopes for shorter wavelengths with smaller mirrors can give comparable resolution to that of larger ground-based systems for longer wavelengths. Space observatories can also observe much fainter sources and larger fields of view with diffraction limited resolution, due to their lower sky background and more stable operating environment.

Due to atmospheric absorption, UV astronomy has been carried out by in-

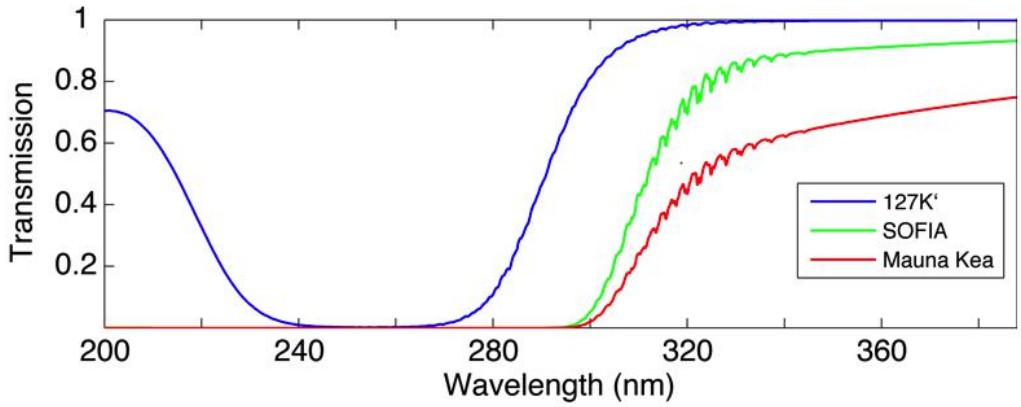

Figure 1.1: Atmospheric transmission for the near UV region at different heights. The blue line is at an altitude of 38000 m, the green line is at 14000 m and the red is at 4200 m. *Image credits: Hibbits et al. (2013)*

struments onboard satellites, sounding rockets, and high altitude balloons. As shown in the image in Fig. 1.1, we need to go well above the Ozone layer in the stratosphere to get access to the near UV. Sounding rocket experiments paved the way for UV spectroscopy and photometry in the 1950s and 60s (Carruthers, 1968; Smith, 1967; Stecher & Milligan, 1962), with the first UV observations of an astronomical object being done by an Aerobee rocket (Byram et al., 1957). Compared to space missions, sounding rockets are less expensive and have much faster response time from concept to launch, which makes them an ideal option for the flight demonstration of the latest technologies for large space missions. The payloads can be recovered and modified for follow-up missions or to observe other objects. The instruments can also be updated between flights, to incorporate the latest advancements in technology. They also provide an opportunity for young researchers to work on all aspects of a mission from planning to launch, enabling them to lead larger missions in the future.

High altitude balloons are another low cost and easily accessible platform for astronomical and atmospheric studies from near space. They can go up to altitudes of up to 50 km (Kumar et al., 2014), which gives us access well into the near UV region. With the help of zero-pressure balloons and favorable wind patterns such as the circumpolar winds, stratospheric balloons can pro-

vide flight times that last many days. Although the scientific outputs of these suborbital platforms may not always be comparable to large space missions, they have their distinct advantages, and there are a number of institutes carrying out UV observations on sounding rockets (Fleming et al., 2013; France et al., 2016) and high altitude balloons all over the world (Milliard et al., 2010).

Although the first space-based telescope was launched in 1968 (Orbiting Astronomical Observatory-2), it was the Hubble Space Telescope (HST), launched in 1990, that revolutionized the field. There were a number of UV telescopes since the 1970s, on various astronomical and planetary missions. These included the Orbiting Astronomical Observatory (Code et al., 1970), Thor-Delta (TD)-1A (Boksenberg et al., 1973), International Ultraviolet Explorer (Boggess et al., 1978), and the Extreme UV Explorer (Bowyer & Malina, 1991). Our knowledge of the far and near UV sky was further advanced by the long-term contributions from the Far Ultraviolet Spectroscopic Explorer (Moos et al., 2000), GALaxy EXplorer (Martin et al., 2005), and the suite of UV instruments on the HST such as the Space Telescope Imaging Spectrograph (Woodgate et al., 1998) and Cosmic Origins Spectrograph (Green et al., 2012). Instruments on-board planetary missions such as the UV Spectrometers on Voyager (Broadfoot et al., 1977) and Juno (Gladstone et al., 2017), ALICE on New Horizons (Stern et al., 2008), and IUVS on MAVEN (McClintock et al., 2015) were instrumental in understanding the atmospheric characteristics of solar system planets and their satellites.

There are a number of space missions with UV instruments planned for next decade. A major one is the World Space Observatory-Ultraviolet (WSO-UV or Spektr-UV) proposed to be launched in 2023. It is a 1.7 m telescope in the 100 –300 nm wavelengths, which will carry out UV sky imaging, high-resolution spectroscopy and long-slit low-resolution spectroscopy (Shustov et al., 2011). The Ultraviolet Transient Astronomy Satellite (ULTRASAT) is a wide-field NUV imaging telescope to detect and monitor transient astrophysical phenomena in the 220 –280 nm (Sagiv et al., 2014). Two of the proposed decadal missions, the Habitable Exoplanet Imaging Mission (Gaudi

et al., 2017) and the Large UV Optical Infrared Mission (Bolcar et al., 2016), also include major UV capabilities. The HabEx mission is more focused on the exoplanet science while being capable of doing general astrophysics as well. The LUVOIR is a general purpose astrophysical observatory with a suite of imaging and spectroscopic along with a coronagraph for exoplanet imaging.

1.3 Astronomy with CubeSats and small satellites

Although there is much scientific interest in the UV domain, there is a dearth of active missions in UV at present. Apart from the HST instruments, the only operational telescopes are the Ultraviolet Imaging Telescope (UVIT) on ASTROSAT (Kumar et al., 2012) and the auxiliary UV telescopes on the Neil Gehrels Swift Observatory (Roming et al., 2005) and XMM-Newton(Mason et al., 2001). One major problem that affects the conception and launch of new space missions is the high cost associated with the intensive testing and documentation prior to building the flight hardware (Brosch, Balabanov & Behar, 2014). There is also a perceived necessity to develop all the hardware by the space agencies, as in the past decades designing and launching space missions was something that only large government agencies could achieve. Since the beginning of the twenty-first century, the scenario has slowly started to change. The induction of private companies such as SpaceX and Blue Origin has started to increase the competency and reduced the costs of launching a satellite. Development of the CubeSat platform with standardized sizes and weights and the use of commercial off-the-shelf components have also helped reduce the time and cost of making small satellites. This has sparked a new wave of interest in using CubeSats and nanosatellites to target specific scientific and technical interests (Shkolnik, 2018). Many universities in India and abroad have an active satellite development program, with the support of ISRO and other space agencies.

Apart from their specific scientific goals, these suborbital and small satel-

lite missions also act as a technology demonstration platform for future large missions. NASA has identified a list of key technological challenges for the decadal missions of the 2030s and beyond, to enable them to achieve their scientific goals such as the detection and characterization of a large sample of habitable exoplanets and answering questions about the origin and evolution of the universe as we know it. CubeSats and SmallSats aim try to bridge this gap in knowledge by testing UV instruments with focused scientific outputs in addition to technology demonstration.

Of the major CubeSats in the past decade, the BRITE (BRIght Target Explorer) constellation (Weiss et al., 2014) was an international collaboration from Canada, Austria, and Poland, to build and launch a constellation of six nanosatellites, designed to do precise stellar photometry. ASTERIA (Arcsecond Space Telescope Enabling Research in Astrophysics) was a CubeSat developed by the JPL and MIT to test whether a CubeSat can perform precise measurements of change in a star's light by achieving better than 5″ pointing stability over a 20-minute observation, and to demonstrate milliKelvin-level temperature stability of the imaging detector (Knapp & Seager, 2015). The first NASA-funded astronomy CubeSat is HaloSat, a 6U CubeSat led by the University of Iowa to measure the soft X-ray emission from the hot halo of Milky Way (Kaaret, 2017). PicSat, a French-led 3U CubeSat was launched into a polar orbit in January 2018, to observe the transit of the young exoplanet Beta Pictoris b in front of its bright and equally young star Beta Pictoris (Nowak et al., 2016). The University of Colorado at Boulder is working on building The Colorado Ultraviolet Transit Experiment (CUTE) by 2020, which is a 6U NUV (2550 – 3300 Å) CubeSat designed to monitor transiting hot Jupiters to quantify their atmospheric mass loss and magnetic fields (Fleming et al., 2018). The Star–Planet Activity Research CubeSat (SPARCS), led by Arizona State University, is a 6U CubeSat devoted to the far and near UV monitoring of flares from low-mass stars (Shkolnik et al., 2018).

1.4 Detectors for UV Astronomy

Astronomical objects often emit 10^4 to 10^8 visible photons for every UV photon in the 100 to 200 nm wavelength region (Joseph, 1995). This makes the development of detectors with good sensitivity and lower noise levels crucial for all UV missions. This section describes the basic working principle of photon counting detectors, the types of commonly used detectors, and their characteristics.

1.4.1 Photon counting technique

The UV photon event rate is very low even in the outer space; therefore we need to have a very sensitive detector to discriminate between the noise and the actual signal. As the amount of incoming flux decreases, the photon distribution becomes more and more discrete as shown in Fig. 1.2. At typical flux levels from UV sources, the input power is so less that single photons can be identified. Under this condition, the amount of flux from the sources can be measured by counting the number of such single photons. This method is called photon counting, which is usually used to detect such weak signal by utilizing pulse discrimination and counting technology to identify and extract individual photons. The number of output pulses in a given time is directly proportional to the amount of incident light, and this pulse counting method has advantages in signal-to-noise (S/N) ratio and stability over the analog mode in which an average of all the pulses is made. Since the detected pulses undergo binary processing for digital counting, the photon counting method is also referred to as the digital mode.

1.4.2 Types of detectors

The detectors used in astronomy fall broadly into three categories: photoemissive, photoconductive, and superconducting devices. Photoemissive devices consist of a photocathode coating that is sensitive to the incoming photons

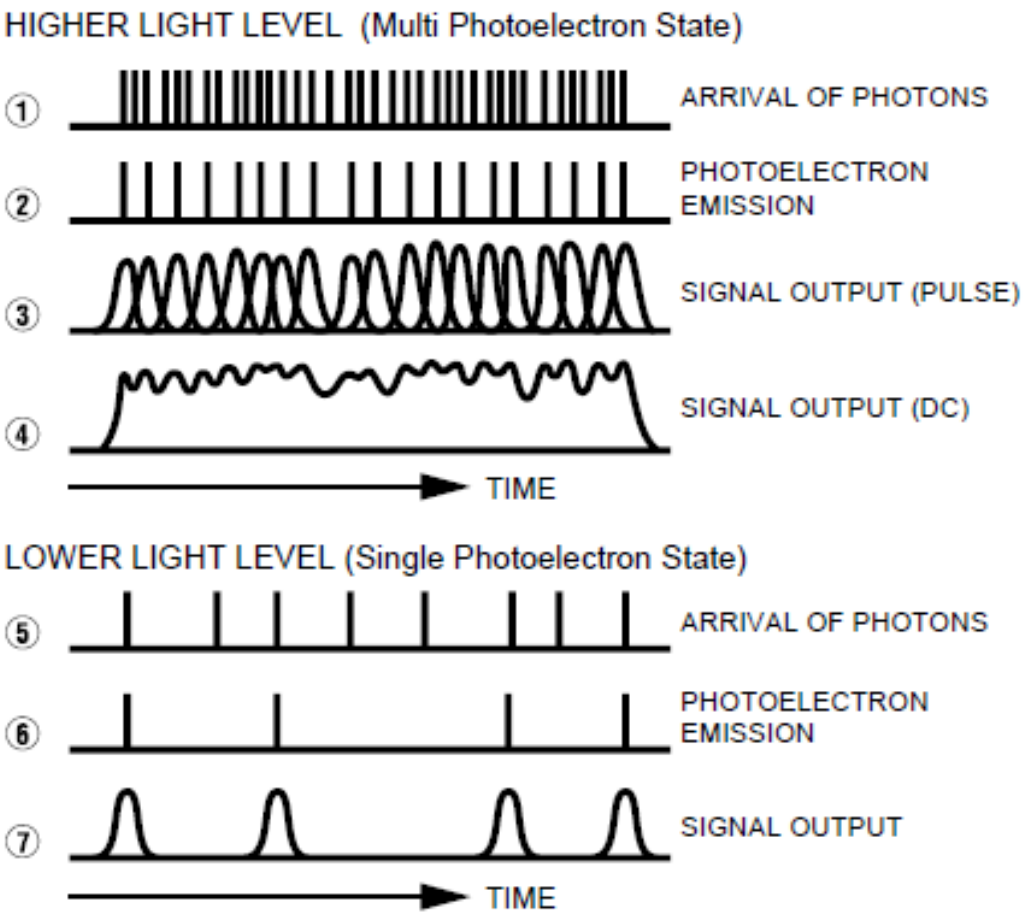

Figure 1.2: Operating principle of photon counting detectors. *Image credits: www.physicsopenlab.org*

and a mechanism to amplify and read out the emitted photoelectrons. They have a tailored response to a particular wavelength region, based on the photocathode coating. Photoconductive devices are typically silicon-based solid state devices which operate by absorbing the incoming photons to the substrate and converting the resulting charge to a voltage. They typically give a broad wavelength coverage. Apart from the wavelength response, there are various other factors to be considered before selecting a detector such as its dynamic range, background, and multiplexing capabilities. Since the size of the optics is severely limited in space, the performance of the detector plays a major part in determining its science capabilities. No single detector technology is capable of meeting all these performance criteria, so trade-offs have to be made based on the science requirements, spacecraft constraints, and the

cost involved.

1.4.2.1 Photoemissive detectors

Photoemissive devices have been the workhorse detectors for past UV space missions due to their low noise levels, long wavelength rejection, and good spatial and temporal resolution. They work on the principle of single photon counting, which means that under faint light levels the incoming UV light can be considered as a discrete number of photons. The detector has to calculate the position and time of arrival for each photon with high resolution and store or transmit this information. Fig. 1.3 shows the typical configuration of a photoemissive detector. The photon in photoemissive devices must have sufficient energy to eject an electron from a photocathode material, typically requiring energies of a few electron volts. These image sensors are therefore natural UV detectors that produce negligible dark backgrounds at room temperature. Photoemissive devices can be constructed to be inherently solar blind as well.

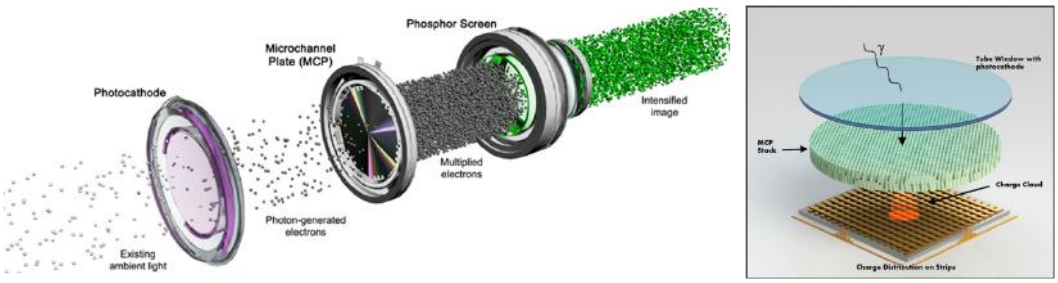

Figure 1.3: *Left*: MCP structure with phosphor screen anode *Image credits: www.photonis.com. Right*: MCP cross section with cross strip anode *Image credits: Siegmund et al. (2014)*

.

As shown in the image in Fig. 1.3, the incoming photons are first converted to photoelectrons at the photocathode. The photocathode may be deposited on a protective window made of MgF_2 or Fused Silica, either in a reflective or transmissive configuration. For Extreme and Far UV applications, there is a lack of suitable window materials with good transmission, in which case it is deposited directly on the MCP front surface, making the photocathode exposed to the environment and prone to contamination. The photocathode

coating is selected to give a good quantum efficiency in the wavelength region of interest. The Fig. 1.4 shows the commonly used photocathodes in the NUV and their spectral coverage.

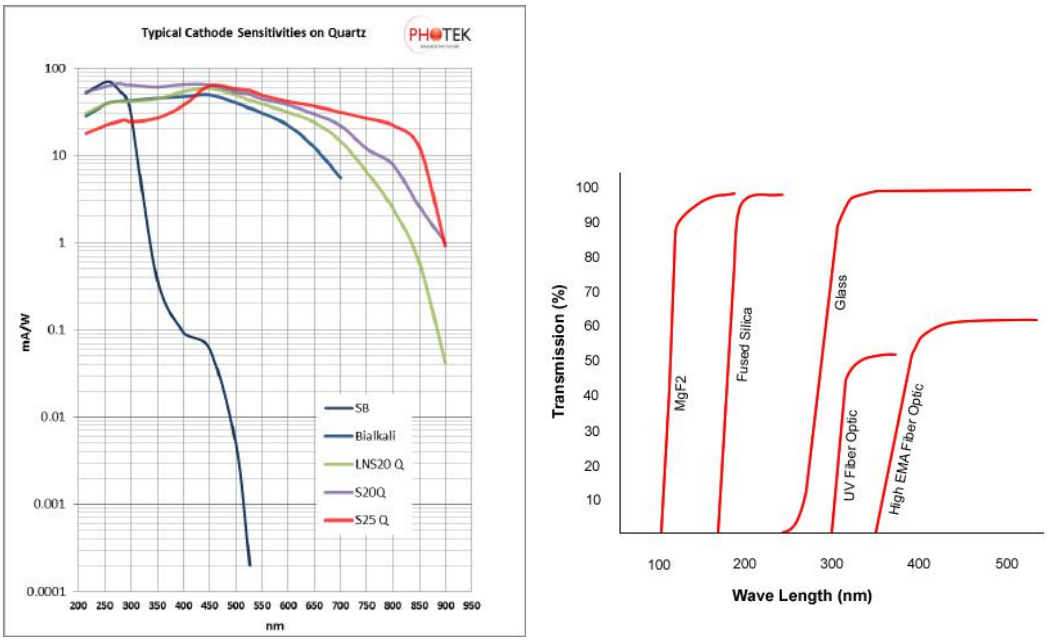

Figure 1.4: *Left*: Commonly used photocathodes in the NUV and their spectral coverage. *Right*: Input optics used in MCPs with their transmission. *Image credits: www.photek.com*

The heart of the detector is the microchannel plate (MCP). It consists of an array of glass tubes in a circular or rectangular configuration. The entire system acts as a photomultiplier tube, where the input window and the photocathode are kept at a negative voltage of a few hundred volts to repel the emitted electrons towards the MCP. They fall on the MCP pores where they emit secondary electrons from the walls which are further accelerated forward with the help of an increasing positive potential given along the MCP pores. We can also stack two or three MCPs as a Chevron or Z-stack configuration, to achieve higher gains. At the output surface of the MCP, typically kept at a few kilovolts, each incoming photon may be multiplied into 10^4 to 10^7 electrons. A high voltage power supply is used to bias the cathode, MCP, and anode terminals of the device.

The charge cloud at the MCP output surface can be read out either optically or electronically. For optical readouts, a phosphor screen is used as

an anode, to convert the incoming charge cloud to a bunch of photons. The phosphor material determines the wavelength of the emitted photons and the response time of the anode. Thus, for a single incoming photon that is detected by the photocathode, we get a bright spot consisting of 10^4 to 10^7 photons at the phosphor. This light is coupled to a charge coupled device with a fiber optic taper or a lens system. These types of devices are called intensified CCD or intensified CMOS detectors. Although these are relatively simple and easy to procure off-the-shelf, they tend to be limited by the temporal and spatial resolution of the solid state readout and also by the aberrations introduced by the relay optics.

For larger and complex space missions, custom-made electronic readouts are used as the anode. Here the anode is an electronic circuit capable of reading the charge cloud from MCP output directly and determining its X-Y position and time of arrival. Earlier instruments such as STIS used a 1024×1024 array Multi-Anode Microchannel Array (MAMA) as detector (Joseph et al., 1995; Kimble et al., 1999). The FUSE mission used two Double Delay Line (DDL) detectors (Sahnow et al., 2000) and GALEX had Cross delay line anodes (Siegmund et al., 2004), which consists of two perpendicular lines in the X-Y plane. When a charge cloud falls the delay line anode, it induces a differential voltage on these lines. The time taken by the charge to propagate to the end of the delay lines can indicate the X-Y position of the charge cloud. The most recent missions use a cross strip anode, which has a cross strip pattern made of metal and ceramic layers that sense the charge cloud. The centroid is calculated after the charge cloud gets amplified and converted to voltage with the help of on-ship preamplifiers and Analog to Digital Converters (ADCs). These are the current state of the art detectors, with count rates of ∼100 MHz and spatial resolution of $\sim 10\mu$m (Tremsin et al., 2003).

Pulse Height Distribution

Pulse height distribution (PHD) is a fundamental characteristic of the photon-counting detectors. It is a histogram showing the number of spots at the

output as a function of pulse height. This is significant for MCPs operated at high gains with more than one stages. For a single stage MCP, the amount of charge that can be contained in a pore is limited by space charge effects inside the walls. This saturation value can be of the order of 10^4 to 10^5 for a single pore in a single stage MCPs. As the number of stacks increases, the saturation value increases and shows a definite peak in the distribution as shown on the left panel of Fig. 1.5. This is because when the electrons pass from one stage to the next, instead of falling in one pore, they get distributed into multiple pores. Each of these pores then generates a charge that is equal to the saturation value. The number of pores in which the electron cloud falls and the number of secondary electrons emitted varies randomly and follows a Poisson distribution.

As more and more MCPs are added, the peak becomes tighter. For better photon counting, a narrower peak and a higher peak-to-valley (PV) ratio are desirable. Generally, the counts corresponding to the valley position are used as a threshold for eliminating false events. The peak will shift horizontally due to change of MCP electron gain. However, image intensifiers are capable of stable photon counting if the PV ratio is high enough. This helps in eliminating the variations due to MCP electron gain due to change in ambient temperature or input high voltage levels, giving better uniformity than the analog image.

1.4.2.2 Photoconductive devices

Another category of detectors is the photoconductive devices such as CCDs and CMOS, typically made of Silicon or other semiconductor materials. These devices are made of an array of photosensitive units called pixels, which consists of one or more silicon-based transistors. The incoming photon causes an electron to transition from the valence band into the conduction band. Each pixel produces an electric charge proportional to the number of photons falling on it. This charge gets shifted through a series of registers towards the output ports. The charge at the output is amplified and converted to voltage levels by an external circuitry for further processing. Depending upon the architecture

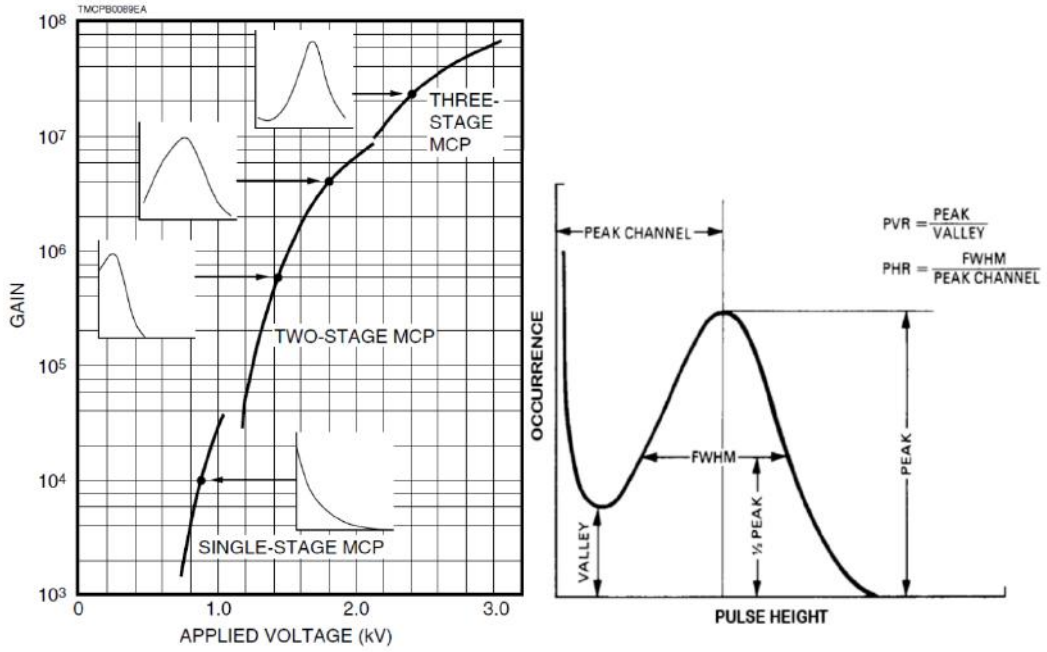

Figure 1.5: *Left:* Pulse height distribution for MCPs with varying number of stacks. *Right:* Typical PHD for a z-stack MCP, illustrating the Peak-Valley Ratio (PVR) and Pulse Height Ratio (PHR). *Image credits: Hamamatsu Photonics*

of the shift registers and the readout mechanism, CCDs are divided into full frame, frame transfer, and interline transfer. CMOS devices differ from CCDs in that each CMOS pixel element contains its amplifier and charge to voltage converter, enabling parallel readout of the pixels.

Spectral sensitivity of CMOS and CCD depend on the band gap of the semiconductor material. Typical Silicon devices have a bandgap of 1.1 eV making them inherently sensitive to visible and infrared wavelengths. Short wavelength photons such as UV and X-Rays cannot be detected by conventional front-illuminated CCDs, as their absorption depth is low and the photons get absorbed before reaching the photosensitive region. This can be solved by illuminating the substrate from the other (back) side so that the absorption and scattering in the gate and pixel structures on the front surface are avoided. These devices also employ surface passivation to avoid the electrons interacting with the traps at the Si-SiO_2 interface which can result in poor and unstable QE. One such technique is known as delta doping (Nikzad et al., 2017, 1994).

Using Molecular Beam Epitaxy (MBE), a thin layer of silicon is grown on the back side containing an extremely high concentration of p-type dopant atoms. This layer modifies the band structure of the backside substrate in such a way that the photoelectrons produced are not trapped near the interface and are instead captured in the potential well as intended. The quantum efficiency of these devices is limited by the reflection of the photons from the back surface and can be enhanced by the deposition of antireflection (AR) coatings (Hamden et al., 2011).

Another technique to improve the UV sensitivity of CCDs and CMOS detectors is to fabricate a hybrid detector with an additional photoemissive layer in front of the CCD. In Electron Bombarded CCDs (EBCCD), photons are detected by a photocathode similar to that in an image intensifier (Ulmer, 2006). The released electrons are accelerated across a gap and impact on the rear side of a back-thinned CCD. These energetic electrons generate multiple charges in the CCD resulting in a gain of the order of 10^2. Another technique to improve the short wavelength performance of CCDs is to incorporate gain stages within the CCD chip. These devices have additional multiplication registers with higher-than-typical CCD clock voltages (50 V), which can provide a gain factor of 10^2 to 10^3. The gain in EMCCDs is achieved by generating secondary electrons via impact ionization by accelerating electrons in the multiplication register by applying the high voltage clock. Such devices are known as Electron Multiplying CCDs (EMCCD) (Denvir & Conroy, 2003) and are gaining popularity for UV observations.

1.4.2.3 Superconducting Devices

Superconducting detectors or cryogenic devices were previously common in shorter wavelengths of X-rays, but are now being extended to the longer UV-optical domains also. These include two types of devices: Superconducting Tunnel Junctions (STJ) and Transition Edge Sensors (TES). The main attraction of these devices is that they can sense the energy of the photons as well, in addition to the x-y position and arrival time. In the UV regions

($\lambda \sim 100$ nm), they are reported to show a spectral resolution of R=100 and a temporal resolution of 100 ns.

STJs consist of a pair of superconducting plates made of materials such as Aluminum which is kept at very low temperatures of less than 1 K and separated by a thin insulating layer such as Silicon (Peacock et al., 1996). They work similar to silicon detectors in that when the photon falls on the junction, it produces an excitation current. This passes through the insulating layer through quantum tunneling, which is proportional to the number of photons. It is sensitive to a few milli eV of radiation, making the device highly sensitive. TESs are micro calorimeters that work similar to superconducting thermistors (Cabrera et al., 1998). They sense the change in temperature due to the incoming photons, to determine their energy. A transition-edge sensor is a thermometer made from a superconducting film made of Molybdenum/Gold bi-layers operated near their transition temperature. While in its transition from superconductor to normal metal, a minimal change in temperature causes a significant change in resistance. Transition widths are typically in the order of a milli-Kelvin.

One of the biggest drawbacks of these devices is the temperature constraint. The devices need extensive cooling systems to maintain their temperatures near the transition temperatures. Multiplexing technology has to be advanced yet to develop these into larger formats of above 256×256. Another issue is their poorer temporal resolution and jitter when compared to the traditional detectors. These are not inherently solar blind and so, to make them suitable for UV applications, we have to put filters to block the visible and IR light. Conventional filters, such as the Woods filter, are not very efficient, which may reduce the throughput of these devices further. The research in anti-reflecting coatings is expected to improve their efficiency.

1.4.3 Performance metrics of UV detectors

This section briefly mentions the key characteristics of commonly used detectors that make them desirable or undesirable for UV applications

Spectral Response: An ideal UV detector shows high sensitivity in the UV (900 – 350 Å) region and very low response to longer wavelengths. Quantum efficiency of the detector denotes the ratio of the number of photoelectrons generated and the number of incoming photons, and depends on the incident light wavelength. For MCP-based detectors, it is determined by the photocathode material, with the short wavelength cut off determined by the input window material. The collection efficiency (CE) is another important parameter that shows the percentage of generated photoelectrons that eventually get collected at the anode. This number is 60-90%, which is determined by the shape of the photocathode and the structure and voltage distribution of the MCP. Another requirement for UV detectors is that they should be not sensitive to the optical regions. Most astronomical sources emit 10^4 times photons in the optical compared to UV, which makes it important that the detector be inherently insensitive to these photons, for better noise performance.

As shown in the images in Fig. 1.4, photocathodes commonly used in photoemissive detectors have a QE of 10-20 % in the UV region. Alkali halides (CsI, KBr) typically used in the Far UV (900 –1800 Å) show 10 % and solar blind ones (CsTe, RbTe) used in the near UV (1800 – 3000 Å) show a similar 10-15 % quantum efficiency. To extend their sensitivity to optical region, multi-alkali photocathodes such as S20 are used, which show 20-40% QE. Recent years have seen advances in GaN and AlGaN photocathodes that show higher QE of 70% in the entire UV region and are inherently solar blind (Siegmund et al., 2008).

CCDs can show higher QE of 50% in the ultraviolet with back illumination and delta doping. However, as the peak spectral response of Silicon falls in the near IR region, they are not solar blind. This necessitates the use of one or more UV bandpass filters in front of them. Due to the filter transmission limitations, the sensitivity of CCDs also effectively drops to 20 %.

Background and dark Current: The primary source of noise in MCPs is the dark current which is the thermally generated photoelectrons. They get

multiplied inside the MCP and generate false counts at the output, which cannot be distinguished from actual photon events. The dark current increases by a factor of 3-10 for each 10 ° increase in temperature. Photocathode materials determine the value and temperature dependency of the dark counts. Multi alkali materials such as S20, that are sensitive to the visible region, are known to show a high dark current and require extensive cooling. Other causes of background events are cosmic ray interactions and ion feedback. Due to their long wavelength sensitivity, CCD and CMOS devices are also susceptible to temperature dependent dark currents. Most of the scientific CCDs are cooled with liquid Nitrogen to a low temperature of around 170 K to minimize its effects. These devices also suffer from readout noise, which is associated with the electronic readout circuitry. This is noise is absent in photon counting MCP detectors as each pulse is counted digitally.

The main parameter that makes MCP based photon counting detectors attractive is the noise performance. Most of the solar blind photocathodes show negligible dark noise of the order of 5 counts/sec/cm^2 and zero read noise, which means the only source of noise is the photon noise which varies with the incoming number of photons as a Poisson distribution. This allows us to have large integration times, enabling the observation of very faint sources.

Spatial and temporal resolution: Resolution is a key characteristic that decides the application of the detector on imaging and spectroscopic instruments. The spatial resolution of MCPs largely depends on diameter and center to center spacing of its individual pores. The accelerating voltage and the number of MCP stacks also determine the resolution, as the charge gets spread when it passes from one stack to another. Other major factors are the spacing between the cathode and the MCP front surface and the anode and the MCP back surface, which may cause the electron cloud to spread. These spacings are kept at the order of a few hundred microns to minimize this effect. Another consideration should be the grain size of the photocathode and phosphor material, and the performance of the relay optics in the case of a

phosphor screen anode. Typical commercially available MCPs give 10-20 μm resolution, although photon counting techniques employ centroiding to give subpixel resolution. For CCD and CMOS detectors, the spatial resolution is determined by the pixel size. As larger pixels give better sensitivity at lower spatial resolution, the trade off depends on their particular application.

Temporal resolution depends on the time taken by the electronics for processing the arriving photons and convert them to voltage levels. MCPs with electronic readouts such as cross strip anodes show minimal dead times of the order of nanoseconds. For CCD/CMOS and phosphor screen based readouts, the temporal resolution is determined by the readout circuitry. CMOS devices capable of having a full frame readout in millisecond timescales are standard, with an option of reading out smaller regions of interests at higher speeds.

Gain: The Gain is a distinctive characteristic of MCP and EMCCD detectors. It shows the number of multiplied electrons generated for each photoelectron. The gain in EMCCDs depend on the applied high voltage and the architecture of the multiplication register and is of the range of 100-1000. For MCP-based detectors, the overall gain in the detector is the product of MCP gain, and the optical gain produced by the energetic electrons striking the phosphor. The gain of the MCP depends on the material of the channel and the applied electric field. A single stack MCP typically gives a 10^4 gain for an applied voltage of 1000 V. For higher gains of the order of 10^7, two or three MCPS can be stacked. It is an important parameter because the gain at which MCP operates determines its lifetime.

Dynamic range: Dynamic range implies the range of flux levels that can be detected, from the brightest to the faintest. Since for most astronomical observations, the incoming photons will be concentrated on small local areas, we specify the Local Dynamic Range (LDR) rather than the Global Dynamic Range (GDR) for the entire detector. Due to the multiple amplification stages, the dynamic range of photon counting MCP detectors is generally small, whereas CCDs and CMOS show a better dynamic range of the order of

60-100 db, with CCDs having slightly better performance.

Area and format: Large format MCP based detectors with up to 100 mm diameters have been commonly used for space applications. Advances in semiconductors have made it easier now to manufacture large format CCD and CMOS detectors, with up to 16k x 16k detectors made possible by mosaic CCDs.

Space qualification: The technology for manufacturing MCP based detectors has matured over the past decades. Solid state devices have traditionally been expensive and difficult to manufacture to space, but recent advances have helped make the process easier and drive the cost down. There is a large attraction towards getting space qualified CMOS and CCDs for near UV CubeSats, as MCPs with their bulky high voltage power supplies are difficult to accommodate in a small CubeSat volume.

1.5 Motivation and Thesis outline

At the high-altitude balloon group at IIA, we develop compact payloads with off-the-shelf components that can be tested on a stratospheric balloon and later, made into fully space qualified payloads for small satellites. The program started off with imaging payloads for photometry, but we are now focusing on spectroscopic instruments to observe both point and extended objects with moderate spectral and spatial resolution. Detectors are often one of the most critical and expensive components of any space-based instrument. It is important to have a highly sensitive, low noise detector in the UV region where the incoming photons are very few.

The primary aim of the thesis is to design, fabricate and characterize detectors for UV space and balloon missions. The previous sections clearly show that there is no clear detector technology of choice for UV applications, and the choice largely depends on the mission constraints. Although UV CCDs are getting popular, we would like to have photon counting capability to look at

faint sources, and so we have decided to develop an MCP-based detector. Since custom electronic readouts are expensive, we have decided to use a phosphor screen anode and CMOS readout. To allow for real-time, on-chip processing, an FPGA based processor is used to implement the centroiding algorithms.

The following chapters describe the development of detectors and their application on payloads aboard various balloon and small satellite platform. We will also briefly describe the science goals and instrument parameters of these payloads.

Chapter One: Introduction

This chapter describes the motivation, importance, and present status of thesis work. We discuss the types of detectors that are typically used in near space platforms with a brief introduction to their operating principle, flight legacy, and advantages and disadvantages.

Chapter Two: Development of an Intensified CMOS Detector

Here we discuss the design and development of a prototype photon counting detector. we are using an S20 Photocathode that gives a QE in both NUV and visible (2000 - 9000 Å). We use an off-the-shelf CMOS sensor from OmniVision (OV9725) for the readout. A Spartan 6 FPGA does the image acquisition and processing. The implementation of the hardware and software, as well as the calibration steps, are included in this chapter.

Chapter Three: CubeSat and Balloon Applications

The detector is being used as the back end instrument of two of our UV payloads on a balloon platform above 40 km. One of the instruments is fiber-fed, near UV spectrograph for atmospheric observations in the 250 – 400 nm region. The detector also flies on a wide-field UV imager for observing solar system objects such as comets and asteroids and other bright UV transients. It is an all-refractive 70 mm telescope in the 250 – 350 nm wavelength range with a 10.8° field of view.

Chapter Four: PESIT-IIA Imager for Observing the Night Sky (PIONS)

This chapter deals with the design, fabrication, and calibration of the PESIT-IIA Observatory for the Night Sky (PIONS), which is an NUV imaging telescope to be flown on a small satellite. The optical, mechanical and, electrical design will be described here along with the major scientific objectives of the instrument.

Chapter Five: Development of an FUV detector

Another aspect of the thesis is the development of FUV instrumentation. The first part covers the development of detectors for the Far UV (FUV; 900 - 1800 Å), by assembling custom-coated, semi-transparent photo-cathodes on bare MCP. The second part briefly describes the development of an FUV imaging spectrograph to study extended objects in the 900-1800 Å region to observe the extended objects such as supernova remnants and planetary nebulae.

Chapter Six: Conclusion and Future Work

The chapter concludes the thesis with a brief discussion of the instruments developed so far and the possibilities of observations with them.

Chapter 2

Development of an Intensified CMOS Detector

S. Ambily, M. Sarpotdar, J. Mathew, A. G. Sreejith, K. Nirmal, A. Prakash, M. Safonova, and J. Murthy, Journal of Astronomical Instrumentation, Vol. 6, Issue 1, 2017.

2.1 Introduction

Access to space has become easier and cheaper with the advent of small satellites such as CubeSats (e.g. Brosch, Balabanov & Behar, 2014). We are developing compact scientific payloads using off-the-shelf components with tight constraints on weight, size, and power, for atmospheric and astronomical studies in the NUV range (200 –350 nm). We test and qualify these payloads using high-altitude balloons, with the expectation of space flights when the opportunity arises. In particular, we have designed and developed the MCP-based photon counting detector which we plan to fly soon.

Photon-counting detectors using MCPs have been the standard for UV payloads because of their low readout noise, large detector area, radiation tolerance, and long-wavelength rejection (Kimble et al., 2003). There are variations in the number of the MCP stacks, types of filters and photocathodes,

and in the anode and readout electronics (Joseph, 1995). For complex payloads with high levels of customization, all-electronic readout mechanisms, such as Cross Strip (XS) anodes, Wedge and Strip anodes, Multi-Anode Microchannel Arrays (MAMA), or Delay-Line anodes are used in (Vallerga et al., 2009). The charge clouds from the MCP electrodes in these systems are read out by a custom electronics board which converts the amplified electron charge cloud into a corresponding voltage level (Vallerga & Siegmund, 2000). These readouts are often expensive and, while their cost is justified for high impact missions such as *GALEX* (Martin et al., 2005) or *FUSE* (Moos et al., 2000), they may not be needed in less ambitious missions.

We have achieved significant savings in cost by using a phosphor-screen anode as the readout (Bonanno et al., 2001), and by focusing the image of the anode onto a CMOS sensor using a lens. We have chosen a photocathode (S20) with sensitivity in the range 200–900 nm for our initial development so that we can use it in both the NUV and the visible. The detector works as a CMOS camera in bright light, transferring each frame serially to the data processing system, and as a photon-counting detector in faint light conditions. In both photon counting and continuous frame-readout modes, the data acquisition and processing unit is the same field-programmable gate array (FPGA) board. Therefore, the modes can be changed by just switching from one code to another on the FPGA, without the necessity of making changes to the hardware.

In this paper, we describe the various aspects of the design and implementation of the detector, with a focus on the data acquisition algorithms that run on the FPGA. We also discuss the hardware implementation of these algorithms, as well as the results of few calibration and characterization tests on the whole sensor.

2.2 Detector Overview

The detector (Fig. 2.1) is an intensified CMOS camera comprising the two parts:

1. An image intensifier with an MCP and its associated high-voltage power supply (HVPS);

2. A readout and processing unit, which includes a relay lens, CMOS sensor and a digital readout card using an FPGA.

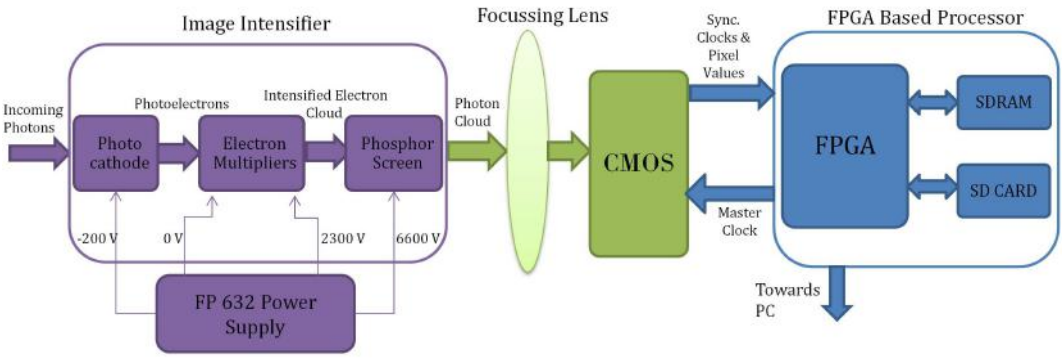

Figure 2.1: Detector Block Diagram

2.2.1 Image Intensifier

We are using an MCP340 assembly from Photek[1]. It is a 40 mm, Z-stack MCP with an S20 photocathode deposited on a quartz input window and a P46 phosphor deposited on the anode. The distance from the photocathode to the MCP front surface is 100 microns and the distance from the MCP output surface to the phosphor is 700 microns.

The MCP is powered by the FP632 micro-HVPS from Photek which weighs only 100 gm, ideal for our lightweight (< 3 kg) balloons. The HVPS provides several outputs with voltages from -200 V to $6,900$ V. The gain of the MCP is set by the voltage at the MCP output, which automatically adjusts the screen

[1] `http://www.photek.com/`

voltage, maintaining a constant MCP-out-Anode voltage difference. The resulting electron cloud from the MCP output electrode is accelerated towards the phosphor screen anode (with a peak response at 530 nm) and the resulting photons are focused on the CMOS surface by a relay lens.

2.2.2 Relay Optics

Electrons from the MCP induce fluorescence in the P46 phosphor screen (40-mm diameter) which is imaged onto the CMOS readout (3.4-mm diameter) using relay optics. Similar commercial systems often use a fiber-optic coupling but these are more difficult to physically implement with high precision. We are now using the TVF-3.6X2812IR-BCDN-MD, a board-level varifocal lens from Senko with high precision zoom and focus adjustment which was provided with the CMOS board. The lens system has an F-ratio of $F1.2$ with an adjustable focus from 3 mm to 10 mm.

This system introduces a significant amount of aberrations into the system because of the large demagnification factor from the MCP to CMOS (17:1) and we are designing a new lens system to better couple the two.

2.2.3 CMOS Sensor

We have chosen a 1 megapixel video image sensor, OV9215 from OmniVision Technologies[2], for the CMOS camera. It is a 1/4 inch sensor that provides full-frame, sub-sampled or windowed 8-bit/10-bit images. The advantages of CMOS sensors in easier readout and circuit integration, as well as their low power requirements, make them an obvious choice over CCDs for our applications. The disadvantage of CMOS sensors is that they have an uncertain photometric flat field but this is not relevant in our photon counting context (Uslenghi et al., 2003). The CMOS chip sits on an off-the-shelf headboard, originally designed for use in CCTV applications[3], which provides a bias and clock for the sensor. As shown in the picture in Fig. 2.2 The headboard reads

[2] `http://www.ovt.com/`

[3] Soliton Technologies: http://www.solitontech.com/

the digital image values and sends them to the FPGA for further processing. It also incorporates one synchronous serial port, which may be used to modify the internal camera registers when needed.

The pixel stream and the three sync signals for the pixel, line, and frame clocks are generated by the CMOS sensor and are connected directly to the FPGA inputs. The master input clock for the CMOS chip is generated by the on-chip crystal oscillator and PLL on the FPGA board. The oscillator frequency is fixed at 12 MHz, but the input clock frequency for the CMOS chip may be varied from 6 to 27 MHz using the programmable PLLs on the FPGA. The successive pixel values are read out as a 2D image matrix and stored in an array on the FPGA memory. The limiting factor in the frame rate is the CMOS frequency, and we are in the process of obtaining and testing faster chips.

2.2.4 Data Acquisition Board

FPGAs provide an attractive option to perform real time data processing, including the on-chip centroiding of photon events. They are Silicon chips with programmable logic blocks and routing resources that can be reprogrammed multiple times. The use of FPGAs allows us to rapidly prototype different algorithms without changing the hardware which is invaluable in a development environment. In addition, the logic blocks can be configured in such a way to implement multiple threads in parallel, providing much higher parallelism and speed when compared to a processor-based system. We also have an option to implement one or multiple soft-core processors-based systems on-chip, to run readily available software modules.

We have chosen the XuLA2-LX25 FPGA prototyping board from XESS Corp.[4] for the design of the main processor since the often used commercial development boards require too many resources (power, weight, complexity). This board meets our minimum requirements in a compact form factor. The

[4] `http://www.xess.com/shop/product/xula2-lx25/`

heart of the FPGA board is a Spartan-6 series XC6LX25 chip[5], which controls and reads out the CMOS sensor, processes the data, stores and transmits the output.

The FPGA modules were written using Verilog and synthesized and programmed using the Xilinx ISE (Integrated Synthesis Environment) Design Suite. Besides, we have used standard VHDL modules[6] for interfacing the SDRAM (synchronous dynamic random-access memory), PLL (Phase Locked Loop), and micro-SD (Secure Digital) card to the Spartan-6 chip on the FPGA board.

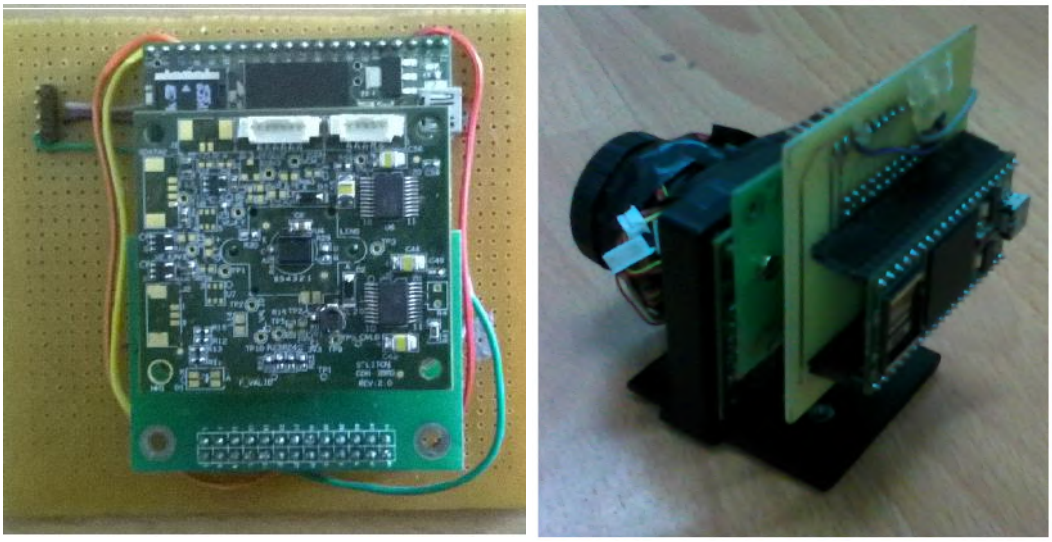

Figure 2.2: CMOS Data Acquisition Board. *Left*: The CMOS development board interfaced with the FPGA board, *Right*: Final assembly with the focussing lens and the electronics.

Technical specifications of detector components are summarized in Table. 2.1

2.3 Implementation

The detector is designed to operate in two modes:

- Continuous frame transfer mode.

[5]Xilinx, Inc: `http://www.xilinx.com/`
[6]XESS Corp.

Table 2.1: Detector specifications

MCP Diameter	40 mm
Type of MCP	Z stack
Photocathode	S20
Anode Type	P46 Phosphor screen
Pore size	10 μm (diameter) and 12 μm (pitch)
Input Window	Fused Silica
Output Windows	Glass
Cathode Output Voltage (Max)	-220 V
MCP Output Voltage (Max)	2800 V
Anode Output Voltage (Max)	6000 V
CMOS Active Array Size	1280×800 (H×V)
Frame Rate	30 fps @1280×800
CMOS Master Clock	6-27 MHz
Data Format	10 bit parallel
Pixel Size	3 μm $\times$3 μm
Dynamic Range	upto 90 dB
CMOS Operating Temperature	-50°C to +85°C
Type of FPGA	Spartan 6Q (XQ6SLX150T)
Number of Logic Cells	147000
On-board SDRAM	512 MB
FPGA Temperature Range	-40 to 100°C

- Photon counting mode.

We have designed the readout and associated electronics of the detector so that we can switch between both modes with no changes in the hardware. In photon counting mode, as and when each pixel value is read out the algorithm searches for possible events and if any, stores their centroids on the SDRAM as shown in Fig. 2.3, *Left*. These values are transferred to the SD card or the telemetry module depending on the mode of operation. This is done in parallel ie when one frame is read, the previous frame's centroids are transferred to the SD card to speed up the operation. In frame transfer mode, the pixel values are directly moved to the SDRAM and after each frame is read the SDRAM is flushed by moving the values to the SD card or the telemetry unit as shown in

Fig. 2.3, *Right*. This adds a small delay in the readout process. We have used the standard SDRAM interface developed by Xess Corp with the architecture shown in Fig.2.4.

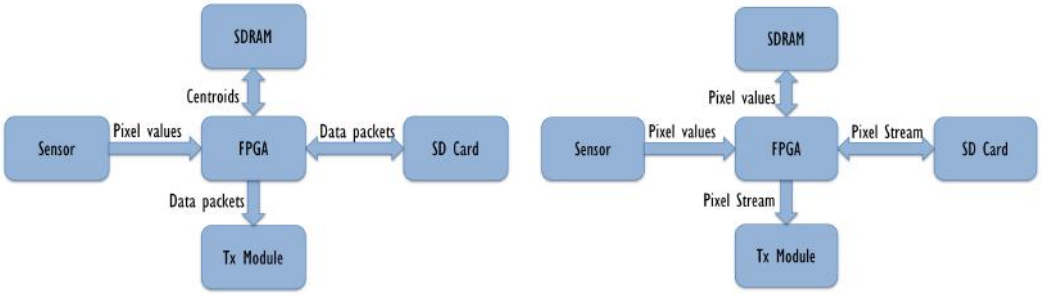

Figure 2.3: Data flow in the two operating modes of the detector *Left*: Photon counting mode *Right*: Integration mode

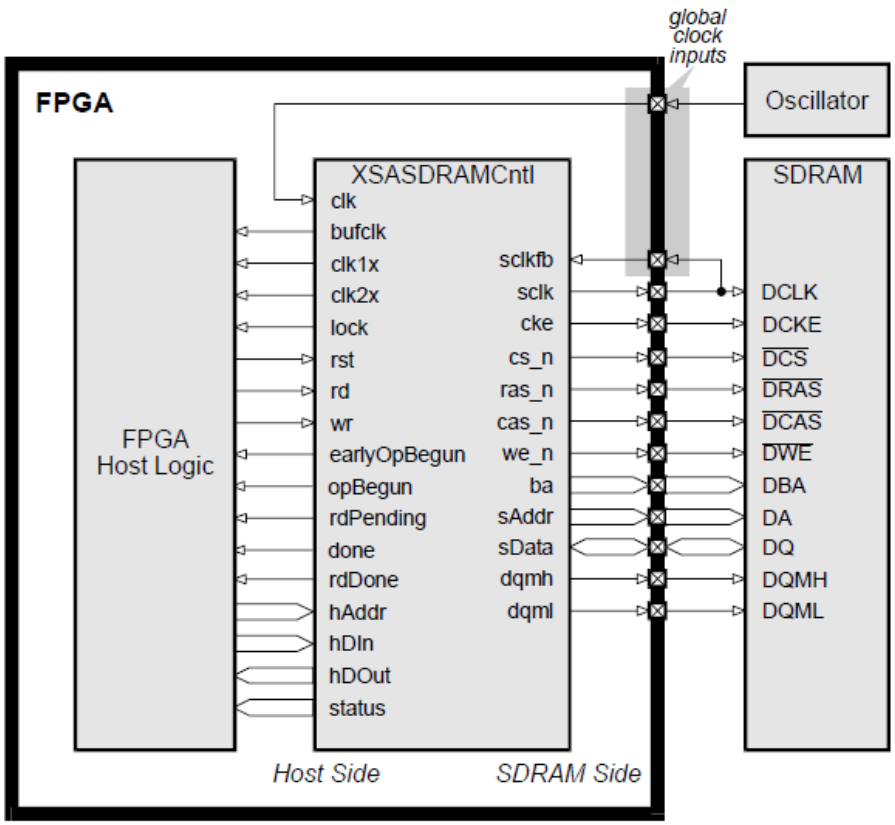

Figure 2.4: SDRAM Controller block diagram. *Image credits: Xess Corp*

Incoming photons eject electrons from the S20 photocathode which are multiplied by the MCP into a charge pulse that falls on a green phosphor screen.

The emitted photons are read by the CMOS sensor with further processing done by the FPGA (Bellis et al., 1991; Fidouh et al., 1993).

The overall implementation of the detector has been broken down to (a) development of the front end photonics system, and (b) interfacing of the digital backend electronics. The first task involves coupling the light from the MCP to the CMOS sensor through a relay lens system with minimum distortion and light loss. The second step involves the clocking and synchronization of the CMOS chip, as well as the programming and interfacing of the FPGA with the host PC. This part is further divided into four steps, which are described in detail in the following subsections.

2.3.1 Centroid calculation

Any photon event on the photocathode creates a charge cloud that is Gaussian in shape. This cloud is spread over multiple pixels on the sensor which we centroid with sub-pixel accuracy using the FPGA. The centroiding algorithm was implemented using a 3×3 pixel sliding window during our tests which we later expanded to a 5×5 pixel window (Hutchings et al., 2007). This yielded better accuracy within our computational limits.

If we operate in the continuous frame transfer mode, all the pixel values will be stored on the SDRAM module which will rapidly exceed our onboard storage. Centroiding on the chip is space-efficient but can be computationally expensive. We implemented a scheme in which we stored only the most recent five rows of the current frame on the FPGA chip (5×1280 pixels). This is illustrated in (Fig. 2.5, *Left*) where we have simulated the sample image array in MATLAB[7]. The image consists of 25×25 pixels and the pixels were read out serially to a 5×25 array. The initial values of the array were assigned to be zero. As each pixel row from the sample image was read, the last row of the array on the simulated FPGA was updated, while the older rows were overwritten with the latest values. This sequence is illustrated in Fig. 2.6. The flow chart for the centroid calculation steps is given in Fig. 2.7.

[7]MathWorks, Inc.: `http:in.mathworks.com/products/matlab/`

Figure 2.5: *Left*: Simulated image array. The values retained after a threshold level are highlighted and the rest of the values are considered to be zero. *Right*: Reconstructed image.

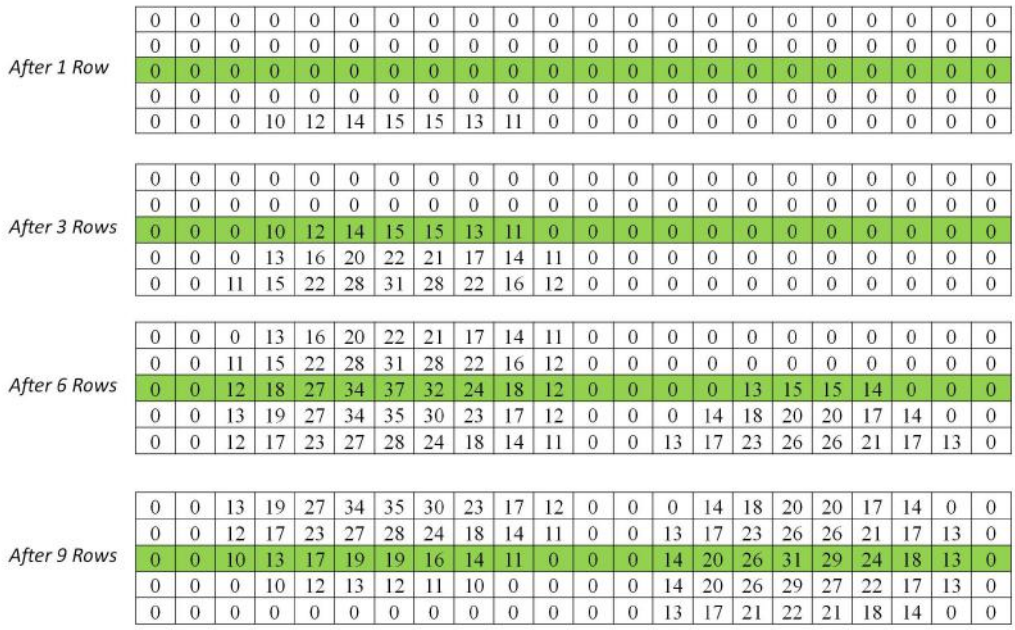

Figure 2.6: The implemented readout: the latest rows are shifted to the FPGA array in a pixel to pixel manner.

2.3.1.1 Thresholding and detecting the local intensity maxima

The first part of our centroiding procedure is to eliminate the dark noise arising from the S20 photocathode, which was measured in the lab (see Sec. 2.5) to be 1000 cps at 23°C. We dynamically estimate the local background level for each photon event and use this value as the event threshold. This is done by

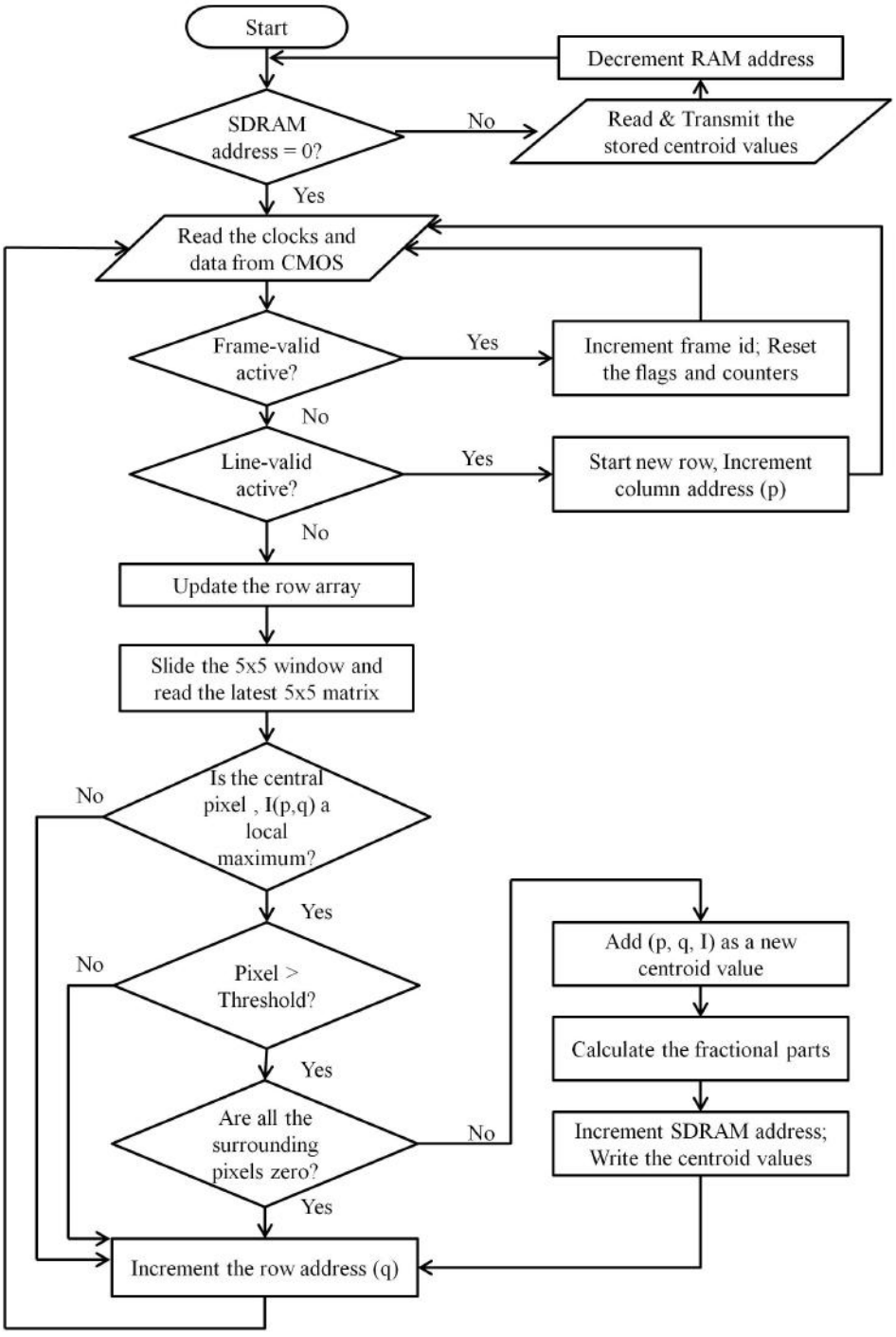

Figure 2.7: Centroiding Flowchart

taking the lowest corner pixel value in the centroiding window (Hutchings et al., 2007).

As and when each pixel is read out, the array containing the last five rows is updated while the older row values are overwritten. The 24 pixels surrounding

the last read-out pixel are read into a separate 5×5 window array, and the window is checked for the presence of any local maxima. We flag the hot pixels and multiple events before calculating the centroids. Hot pixels are removed by eliminating any event where only the central pixel is higher than the threshold. Multiple events are marked by adding the maximum-minimum corner values to the output centroid packets (Hutchings et al., 2007).

2.3.1.2 Calculating the centroid around the maximum points

Once we have identified the hot pixels and multiple events, we calculate the centroids for the actual photon events in the current row. We saved the coordinates of the central pixel as the integer parts of the centroid. We computed the sub-pixel values in parallel by calculating the difference in intensities between the neighboring top and bottom pixels and the left and right pixels of the event (Fig. 2.8). Once calculated, each centroid value consists of the x and y coordinates with their integer and fractional parts and a sign bit to indicate the direction of actual centroid coordinate (top/bottom and left/right) from the central pixel coordinate.

	1	2	3	4	5	6	7	8	9	10	11	12	13	14	15	16	17	18	19	20	21	22
23	0	0	0	13	**16**	**20**	**22**	**21**	**17**	14	11	0	0	0	0	0	0	0	0	0	0	0
24	0	0	11	15	**22**	**28**	**31**	**28**	**22**	16	12	0	0	0	0	0	0	0	0	0	0	0
25	0	0	12	18	**27**	**34**	**37**	**32**	**24**	18	12	0	0	0	0	13	15	15	14	0	0	0
26	0	0	13	19	**27**	**34**	**35**	**30**	**23**	17	12	0	0	0	14	18	20	20	17	14	0	0
27	0	0	12	17	**23**	**27**	**28**	**24**	**18**	14	11	0	0	13	17	23	26	26	21	17	13	0

In this case, for a 3 x 3 window,

xc(integer) = 7 and yc(integer) = 25 and ΣI = 289

xc(fractional) = (28 + 31 + 28 – 34 - 35 – 30) / 289 = -12/289

yc(fractional) = (28 + 34 + 34 – 28 – 32 – 30) / 289 = 6/289

Figure 2.8: Centroid computation from each of the windows. The values obtained here are directly stored as a packet and fractional pixel levels of up to 8-bit accuracy are calculated at a later stage.

2.3.2 Data Storage and Transmission

2.3.2.1 Photon Counting Mode

In the centroiding mode, the output data for telemetry is in the form of packets. Each packet contains a frame ID, event ID, integer and fractional values of centroid coordinates, and the intensity value of the central pixel (Fig. 2.9). These packets are saved on the FPGA by creating a block of registers on the chip. This results in a faster operation: the packets from one frame can be sent over the serial port while the next frame is read. However, the number of photon events that can be saved per frame is limited by the number of logic cells available on-chip. In order to solve this, we save each packet to the SDRAM as and when it is generated.

Frame ID	*Event ID*	*Xc(Int)*	*Xc(Nr)*	*Xc Flag*	*Yc(Int)*	*Yc(Nr)*	*Yc Flag*	*Intensity*	*ΣIntensity*
5	1	7	12	1	25	6	0	37	289

Frame ID	*Event ID*	*Xc(Int)*	*Xc(Nr)*	*Xc Flag*	*Yc(Int)*	*Yc(Nr)*	*Yc Flag*	*Intensity*
5	1	7	0.04	1	25	0.02	0	37

Figure 2.9: Data packet for each photon event. The final output packet is optimized to contain 7 or 8 bytes depending upon the sub-pixel accuracy required.

Hardware description languages do not support division operation as it is impossible to realize a divider module in FPGA hardware and division operations are accomplished using repeated subtractions which add cost to the time and resources. Therefore, when transmitting the packet from the centroiding to the telemetry module, the sub-pixel values are not computed but are simply sent as the numerator and the denominator values. Before transmission, the sub-pixel values can be calculated with an accuracy of 4 bits each by a separate divider module. Because the RS232 transmission runs at a much slower speed than the FPGA clock, the telemetry unit runs the divisions in parallel and transmits the 4-bit fractional values for each packet. It is possible to improve the accuracy to 6 or 8 bits but at the expense of additional clock cycles and hardware resources.

We have implemented an SD card interface for in-flight experiments, where instead of sending the data packets to the PC using a serial port, we use a much faster Serial Peripheral Interface (SPI) protocol to store the data packets on the micro-SD card on the FPGA board. The values from the SD card can be read out as a text file or through the FPGA serial port communication at a later stage.

2.3.2.2 Continuous Frame Transfer Mode

In this mode, the pixel values are directly transferred from the SDRAM to the SD card on-board after each frame is read. Since the SDRAM data width is 16 bits and our images are of 8 bits or 10 bits, the remaining bits are used to store the frame and row number which help in basic sanity checks of the data (such as, check for missing frames, incomplete rows, etc.).

2.3.3 Image Reconstruction

Image reconstruction is intended to derive a meaningful image from the data packets and is done on the host PC (a single board computer in the case of a balloon flight) which receives the serial data from the FPGA board. In continuous imaging mode, the pixel values that are read from the SD card are stored into an image array after basic sanity checks. In the case of photon counting mode, the data stream itself contains a time stamp/frame ID, as well as the x, y coordinates and intensity information, which makes the image reconstruction easier. For example, in Fig. 2.5 (*Right*) we display the image reconstructed from the centroids, calculated from the simulated image (Fig. 2.5, *Left*, in Section 3.2). The image reconstruction flow chart is given in Fig. 2.10.

2.4 Simulations

We have tested the algorithm in MATLAB using a sample image array of 256×256, with simulated Gaussian photon events of random dimensions, positions, and intensity. Poisson noise was added to the image, where the output pixel

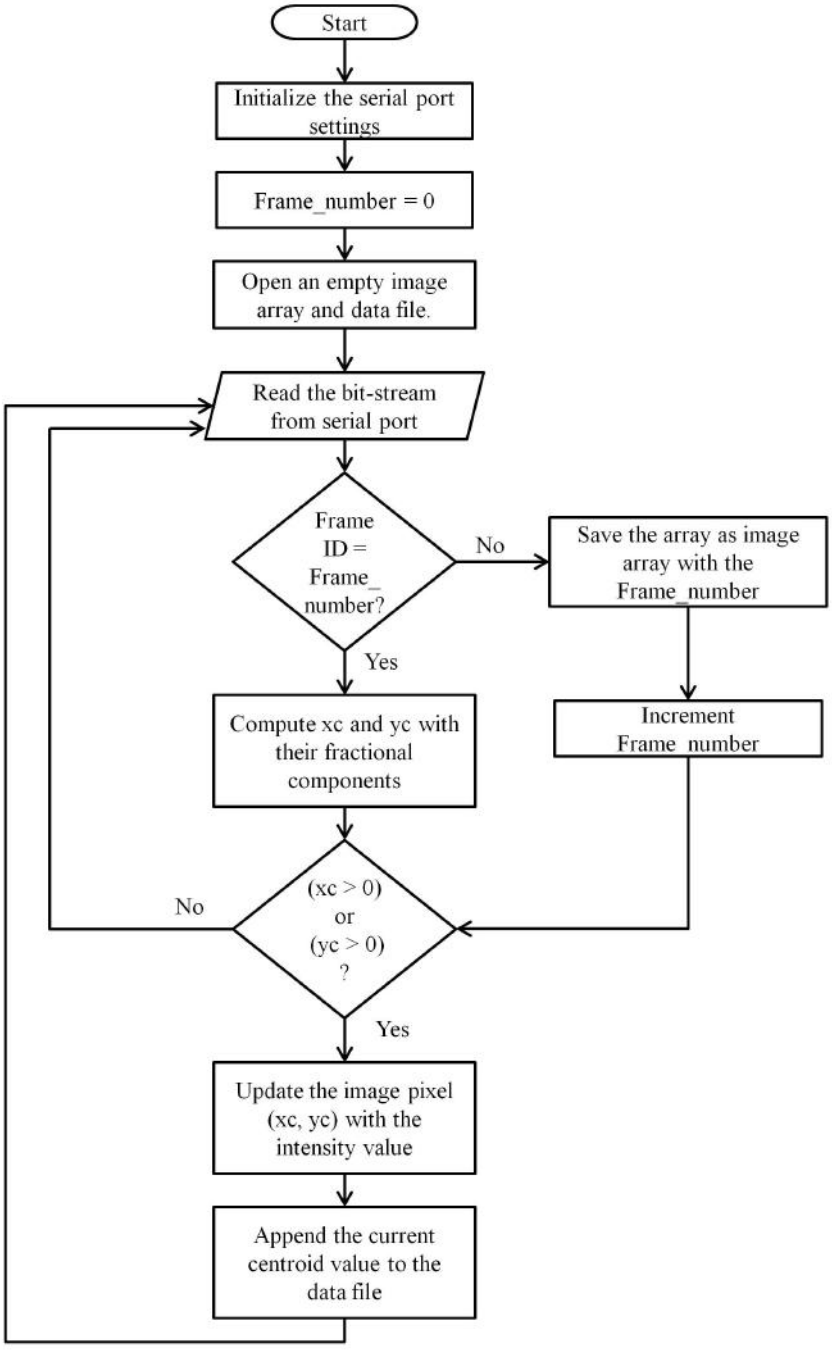

Figure 2.10: Image reconstruction flowchart

intensity was generated from a Poisson distribution with mean equal to the input pixel value. In addition, salt and pepper noise was added to this image with a density of 2%. The image values were normalized to a range between 0 and 1 to simplify the programming. Pixel values from the image array were

read serially in the same way as the CMOS chip readout.

We have run a number of simulations and found that the mean number of photon events in the simulated array was 47.3 with an SNR of 14.6. The centroiding algorithm with a 5×5 window and different levels of thresholding was applied to the sample image to see how the threshold value affects the detection efficiency and noise rejection in the output image. We have illustrated this for one case which had 49 photon events in Fig. 2.11 (*Left*), with the actual photon events circled in red and the isolated hot pixels in green. The blue circles show the points that are actual events but were undetected in the reconstructed image due to their proximity to the edges of the image (numbered 1 and 2). The reconstructed image with the threshold value equal to the mean noise level of the image (0.0025 in this case) is shown in Fig. 2.11 (*Right*). In Table. 2.2, we show the differences in the number of detected events as the threshold values are changed. We see that the optimum threshold value has to be at, or slightly higher than, the mean noise level of the original image for detecting the maximum number of photon events with a higher signal-to-noise ratio (SNR).

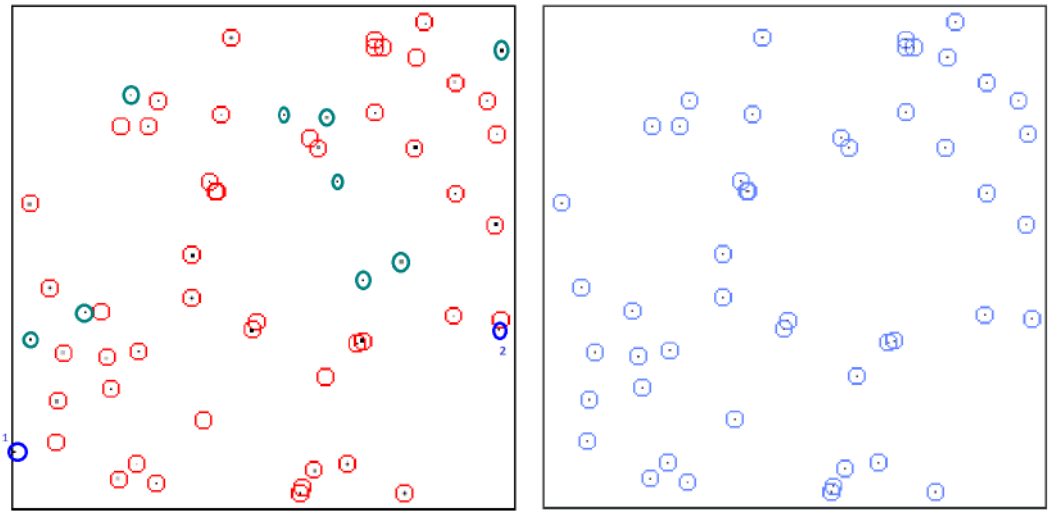

Figure 2.11: *Left*: Original image with the detected centroids highlighted. *Right*: Image after centroiding and reconstruction with a threshold value of 0.0025. The photon events are shown by circles, detected centroids are circled in red. Green circles represent the isolated hot pixels, and the blue circles are the events that were undetected (numbered 1 and 2).

The second step was to implement and test the algorithm in the FPGA

Table 2.2: Comparison of simulated images after reconstruction. First column displays the threshold value applied on the original image. Second column shows the number of detected photon events after reconstruction. The last column displays the SNR after reconstruction.

Threshold value	Number of detected events	SNR
0.0	66	14.9868
0.001	58	15.3433
0.002	54	15.5892
0.0025 (mean signal value)	51	15.6330
0.004	51	15.6330

hardware. The intensity values of the same sample image (Fig. 2.11, *Left*) were approximated to 8-bit values $(0 - 255)$ due to the space constraints in the FPGA memory. The values were serially read by the centroiding module with the frame and line valid signals from the CMOS chip with the mean noise level as the threshold. The centroid coordinates were transferred to a PC through a serial-to-USB converter. The reconstructed image (in the same case as discussed above) has an SNR of 15.72 and 47 detected photon events, of which 45 are actual events and 2 are hot pixels. The fewer number of detected events (47 vs. 49) was because of the 8-bit approximation applied to the original image. The reconstructed image from the FPGA is shown in Fig. 2.12, with detected events highlighted in red circles and hot pixels in black squares.

2.5 Hardware Implementation and Characterization

We are operating the MCP with the gain of 10^6 for the typical voltage values of -200, 2200, and 6000 V at the cathode, MCPOut, and Anode terminals, respectively. The whole detector is powered by an in-house made power supply board which houses the FP632 power supply for the MCP, 5 V LiPo battery, and a voltage regulator. The distance between the phosphor screen and the front of the relay optics is currently kept at 3.5 cm, with the option of fine

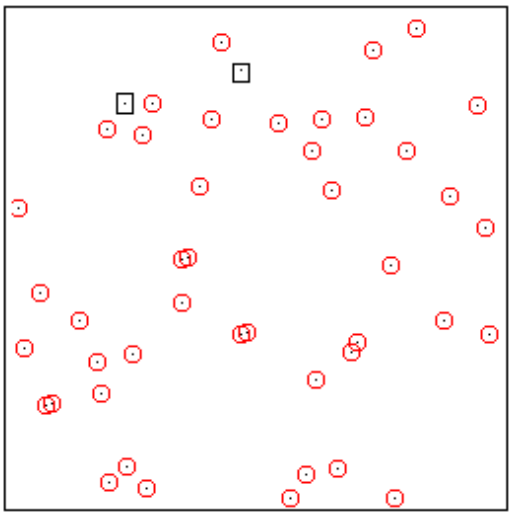

Figure 2.12: Results from the FPGA implementation. Image after centroiding and reconstruction. Real photon events are circled in red, and black squares are the hot pixels.

adjustments by using shims of about 100 μm. This distance was arrived at after a few trials, to provide the best focus for imaging the entire 40 mm diameter of the MCP on the CMOS surface. The CMOS is fixed at the focal plane of the relay lens at 10 mm distance.

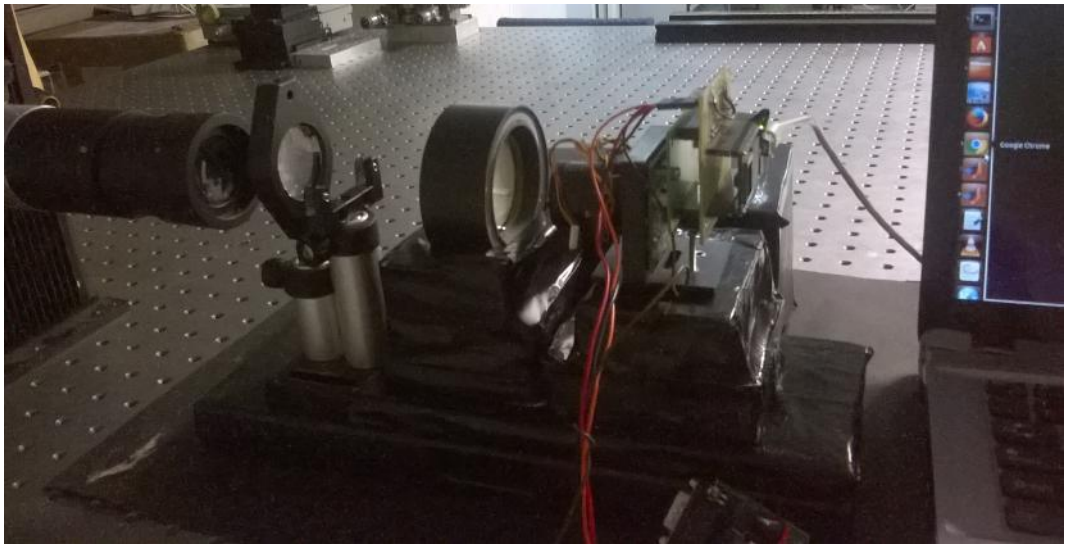

Figure 2.13: Detector test setup on the optical table. From left to right: UV light source, collimating lens, and the detector assembly with the MCP and the readout board.

To perform the characterization of the whole detector, we assembled detector with the MCP, power supply board, relay optics, and the CMOS readout board on the optical table in a dark room (Fig. 2.13, *Right*), with an ambient

temperature of 23°C. A faint uncollimated light source was provided in the form of a green LED with variable intensity, kept at a distance of about 10 cm from the MCP.

2.5.1 Measurement of dark current

We have done the basic tests in both photon counting and frame transfer mode, with the gain in the frame transfer mode lower than in photon-counting mode. The dark count test was performed by covering the detector window and reading the image of the MCP surface on the CMOS in photon counting mode. At room temperature, we saw a dark count of 1000 cps which is expected of an S20 photocathode. The dark count frame is shown in Fig. 2.14, where the events above the threshold are highlighted.

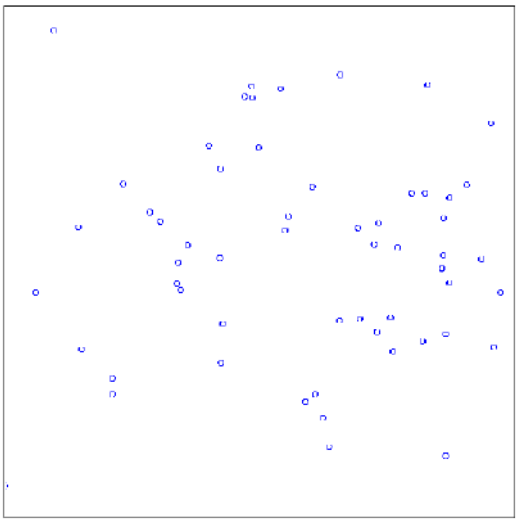

Figure 2.14: Dark count frame at 23°C (34 ms exposure). Highlighted are the detected dark counts.

2.5.2 Estimation of event gain

To estimate the throughput in photon counting mode, we used a faint light from the LED lamp. Though the lamp is not flux calibrated, its intensity can be varied. The CMOS operates at the maximum frame rate of 30 fps, while storage and transmission units run at 40 MHz. This means ideally we

can have up to 22000 cps global event rate, without any significant dead time due to the electronics. However, for our current lab tests, we are using an RS232 connection for transferring the data to the PC, which supports count rates of only up to 6000 cps. Under gain saturation, we have a total number of $\sim four \times 10^6$ photons reaching the CMOS sensor for each event, which translates to 900 ADUs for the CMOS sensor under the Gaussian profile of the event (these values come from the instruments data sheets). Due to the demagnification from the lens, a single pore is confined to 1/4th of a pixel, but each event can be spread across multiple pores depending upon the front end optics.

To better understand the gain characteristics of the detector, we have done the tests for gain variations by measuring the total CMOS ADUs under each event for a number of events due to a faint LED source. We measured the event gain by taking a histogram of the events for three different voltage settings. We can see from Fig. 2.15 that the actual event gain is less than the manufacturer's value, and that it varies considerably. For the cathode voltage of 2.2 kV (gain of 10^6), we see a typical event gain of 550 ADUs instead of 900 ADUs, which may be due to the variations in the efficiency of the phosphor screen or the relay optics or both.

2.5.3 Rejection of multiple events

Even with a very faint LED source, we see some double events in the detector. Such events are detected by an additional threshold value, which is the difference of maximum and minimum corner pixel values. For a 5×5-window centroiding algorithm, we found out the number of double events that are remaining after applying a particular rejection threshold (Fig. 2.16). In this figure, by different colors, we mark the different levels of intensity of the LED lamp, with blue for the highest and red the lowest setting. Though we do not have calibrated flux, we can that at a higher rate of incoming photons we do see a large number of events marked as multiple events, which are detected by using an appropriate value of for the corner threshold. With fainter incoming

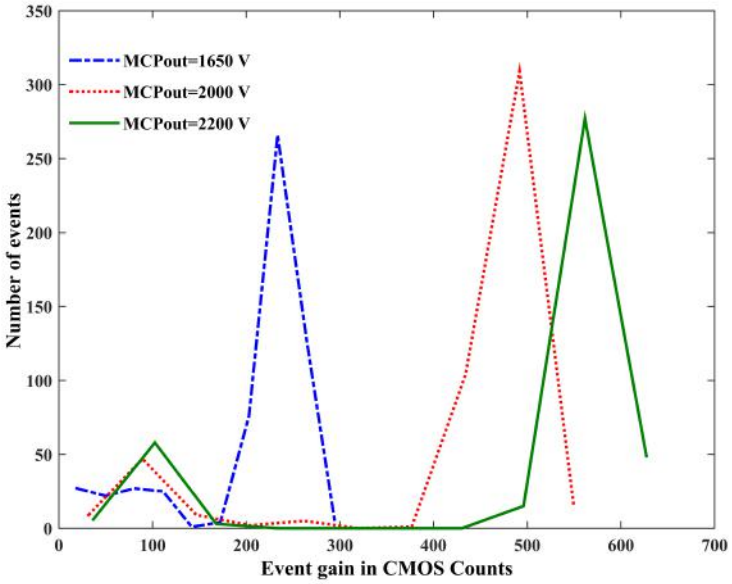

Figure 2.15: *Left*: Histogram of event gains.

flux, this number reduces fast, as expected.

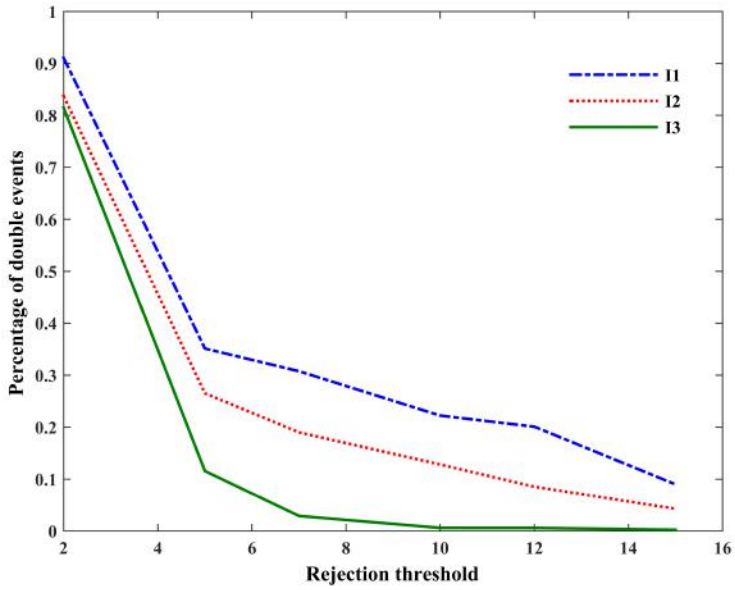

Figure 2.16: Double events vs rejection thresholds (in ADUs) for 3 different intensity levels of the LED lamp. Blue indicates the highest and red the lowest intensity.

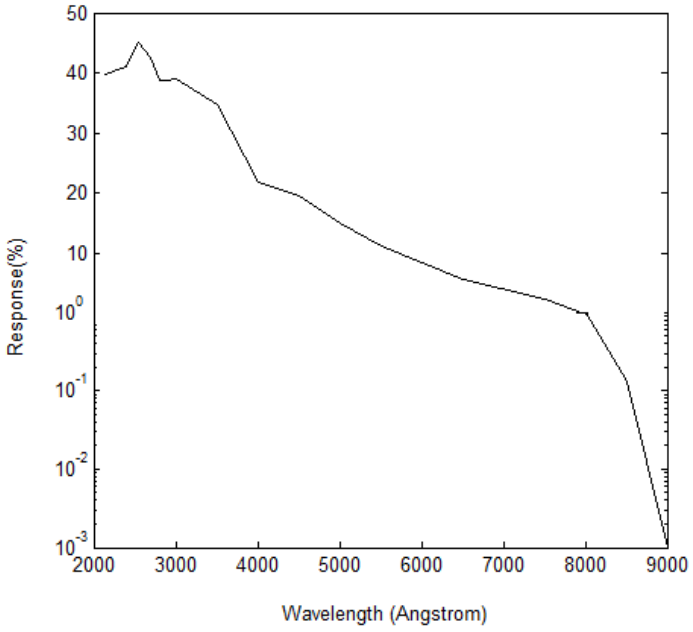

Figure 2.17: Quantum efficiency of the S20 photocathode with a logarithmic scale downwards from 8000 Åto show the drop in QE

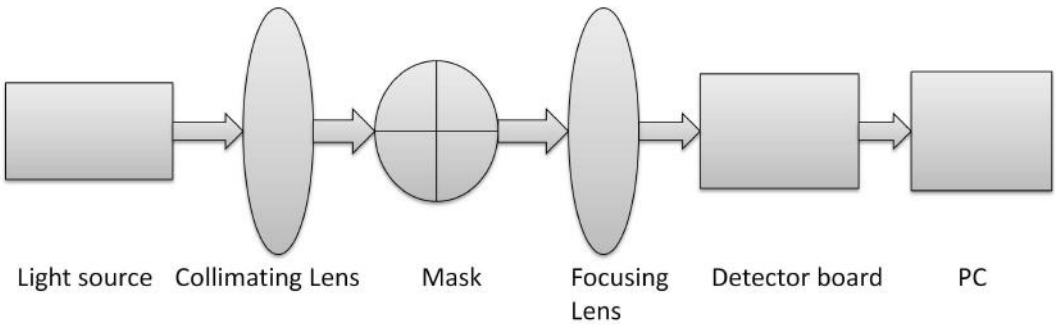

Figure 2.18: Test setup for imaging tests

2.5.4 Imaging tests

To test the overall performance of the detector, we took the images of a USAF target in both centroiding and frame transfer mode as shown in Fig. 2.18. For frame transfer mode, we set lower voltage values for the HVPS, and read the image of the MCP at the CMOS surface. The data rate was kept at 30 MBPS for a 24 MHz input clock rate in full frame, although we have transmitted only one frame per second to the host PC to account for the large transmission delays. The image shown in Fig. 2.19 (*Left*) is reconstructed by the pixel

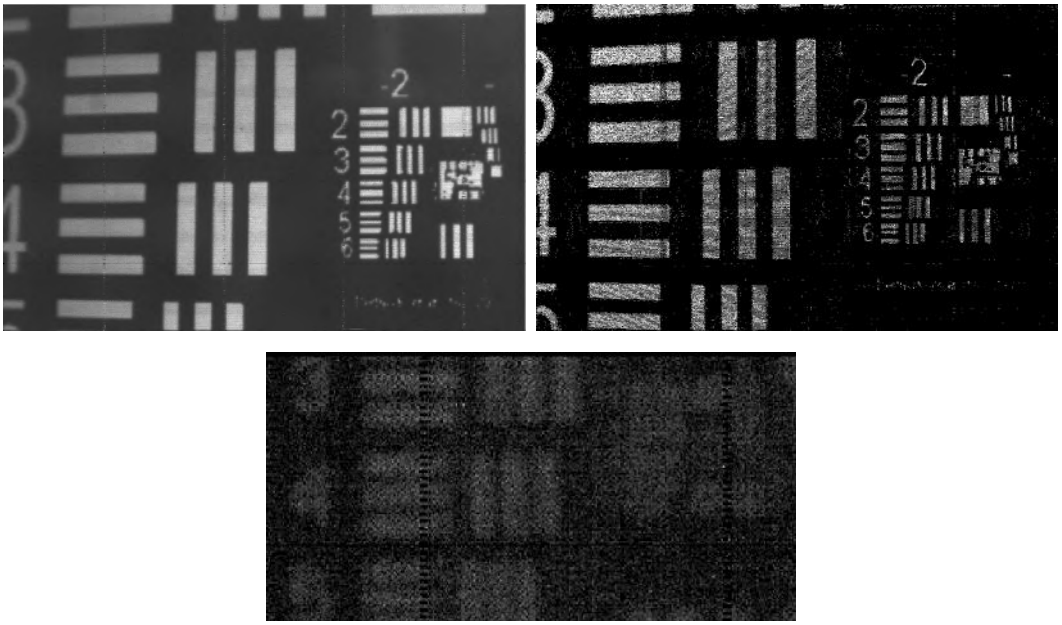

Figure 2.19: *Top Left*: Image of the USAF target in frame transfer mode. *Top Right*: Image reconstructed from the centroids. *Bottom*: Zoomed in version of the image reconstructed from the centroids (including the fractional parts)

values read out serially from the sensor by a MATLAB program. The image in Fig. 2.19 (*Right*) is reconstructed from the centroids with a dynamically estimated threshold value. The data packets, shown in Fig. 2.9, were read through the serial port by another MATLAB program. The centroids for the same frame ID were added together to form the image. The centroid values are accurate up to 1/16th of a pixel, though we have used only the integer parts for the reconstruction. In the current test set-up the resulting spatial resolution was rather low, 1.78 lp/mm, therefore we are not able to resolve within the single MCP pore. One of the reasons we are getting low spatial resolution is the performance of the relay lens (Sec 2.2). We are in the process of optimizing this. In addition, the incoming light was not perfectly collimated which could have introduced the loss of resolution.

We are still in the process of optimizing the interface between the MCP and the CMOS in order to improve the image quality, by using the new custom-made optics. To improve the current temporal resolution (30 cps) to handle faster event rates, we would need to re-program the internal registers of the CMOS through the I2C interface, which is time-consuming and difficult to

implement in real time on the flight. Therefore, in the final version of the detector, we will replace the existing CMOS sensor with a high-speed CMOS sensor NOIL2SM1300A from OnSemiconductors[8], that supports up to 500 fps at full frame and enables on-the-fly addressing of sub-regions.

2.6 Conclusions and Future Work

In the present work, we have described an intensified CMOS detector with an FPGA-based readout developed in-house which can work as a camera in bright light, transferring each frame serially to the data processing system, and as a photon-counting detector with on-board centroiding in faint light conditions. The performance of the electronics is predominantly limited by the performance of the FPGA chip and the speed of CMOS data transfer.

A basic electronic readout system for the CMOS chip is developed using FPGAs along with the capabilities for centroiding, transmitting, and reconstructing the image. The performance of the electronics is predominantly limited by the performance of the FPGA chip and the speed of CMOS data transfer. We have improved the system by procuring components that have higher performance and evaluating the same algorithms on them. The overall performance of the system now depends on the design and implementation of the optics. In the present hardware implementation, we are facing severe distortion introduced due to the high demagnification (20:1) from the MCP output to the CMOS surface. We are planning to reduce the demagnification ratio by using a new CMOS chip of a higher dimension and pixel size. We are also upgrading to a better optical system for focussing the light to the CMOS so that the effects of distortion are minimized.

Another important work ahead is to make the whole detector system flight-ready, where much more rigorous calibration needs to be done with the front-end optics system. The distortion effects need to be modeled so that corrections can be applied to the output images. When operating the MCP in the high-

[8] http://www.onsemi.com/

altitude balloon flights, the operating temperature needs to be maintained, requiring proper insulation of the detector. The S20 photocathode of the MCP is prone to high dark noise which can be reduced by a new photocathode coating, such as a low-noise S20 or a Solar Blind. In addition, other high-altitude issues, such as arcing within the tube, condensation on the input window, etc., need to be addressed.

We are now readying the detector assembly for use in an astronomical payload on small satellites, such as PISAT[9]. We also have a high-altitude balloon program for testing flight hardware (Sreejith et al., 2016). The detector described in this work will be flown as the backend instrument for the near-UV spectrograph as described in Sreejith et al. (2015) and a wide field imager (Mathew et al., 2018a) on high-altitude balloon experiments.

[9]PISAT is a 3-axis stabilized imaging satellite developed by PES University, Bangalore, India. http://pes.edu/pisat

Chapter 3

CubeSat and Balloon Applications

S. Ambily, J. Mathew, M. Sarpotdar, A. G. Sreejith, K. Nirmal, A. Prakash, M. Safonova, and J. Murthy, Proc. SPIE 9905, 2016 &
J. Mathew, S. Ambily, A. Prakash, M. Sarpotdar, K. Nirmal, A.G. Sreejith, M. Safonova, J. Murthy, and N. Brosch, Experimental Astronomy, Volume 45, Issue 2, 2018.

3.1 Introduction

This chapter discusses the applications of the detector on high altitude balloons and small satellites. UV observations are ideally done from space platforms, but they are difficult to access and have long development times. Space experiments have traditionally been technologically challenging and expensive as well, with the detector being one of the most critical components. We have envisioned our balloon program as a platform for testing and verifying the operation of our payloads and as a scientific observatory for atmospheric studies. After prototyping our astronomical payloads on high altitude balloon flights, we work on space qualifying them to fly on small satellites, as going into space has the obvious advantages of longer mission life and the ability to go further into the far ultraviolet.

We have identified a number of scientific motives for our balloon and

space program. The first of these is spectroscopic observations of absorption and emission lines in the Earth's atmosphere from balloon-borne instruments. These allow simultaneous measurement of multiple gas species, including greenhouse gases, aiding in the understanding of our atmospheric chemistry. Balloon experiments are complementary to space-based instruments in that they measure gas profiles instantaneously with different observational geometries while instruments on a low earth orbit (LEO) can monitor long-term changes in the atmosphere. This requires observations from above 20 km in the case of the near UV ($>$ 200 nm) and 200 km in the case of the far UV (90 – 200 nm).

The second goal is to observe astronomical sources such as solar system objects, high energy transients, and other targets of opportunity. Balloon experiments allow us to plan and launch a scientific payload in as short as two weeks, giving us the quick response time required to obtain UV observations of transients. A prime candidate for such an observation would have been comets, such as Comet ISON in 2013, which flash through the sky over a period of a few months. We propose to follow the evolution of pristine comets and other transients such as supernovae, Gamma Ray Bursts, and flare stars, over periods of weeks to months in the UV.

3.2 Overview of high altitude balloon program at IIA

We have begun a high altitude balloon program at the Indian Institute of Astrophysics to enable astronomical and atmospheric observations from a near space platform. The program was started in 2012, and we conduct 5-6 launches a year. Our launch window is from October to May, to avoid the Monsoon season in India. The balloons usually reach an altitude of 25-35 km, which opens the near UV (280 – 400 nm) window for observations (Safonova et al., 2016). We are restricted by regulations by Directorate General of Civil Aviation (DGCA) and the Indian Ministry of Defense that limit the weight of the

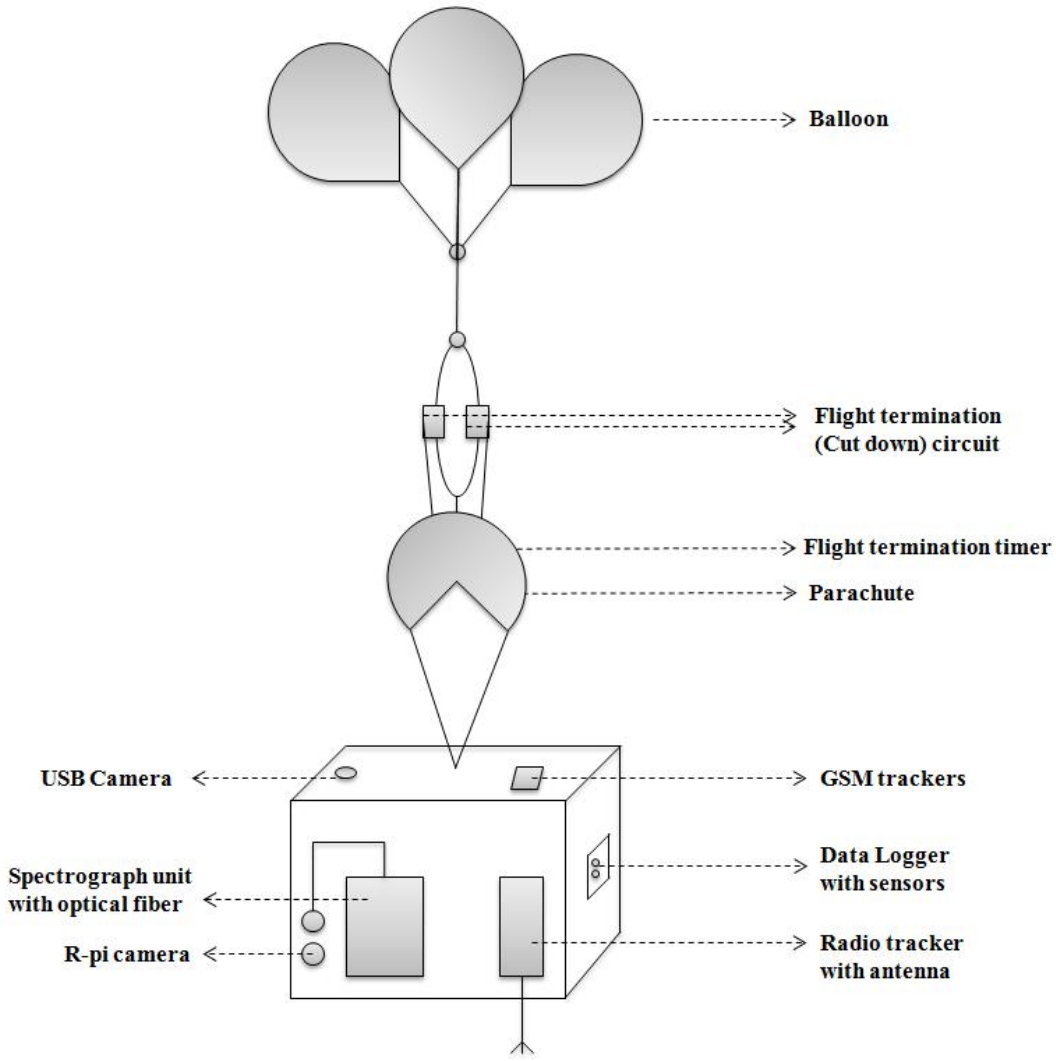

Figure 3.1: Balloon flight train where the spectrograph is used for atmospheric observations with the fiber fixed on the side

payload to 6 kg, and the launch window to 2-4 a.m. on Sundays.

We obtain the Notice to Airmen (NOTAM) from Airports Authorities and the Ministry of defense at least two weeks prior to the balloon launch. An online tool, Cambridge University Spaceflight Landing Predictor (CUSF), is used to obtain the balloon trajectory. Once the payload and balloon mass is fixed, the calculator also helps us estimate the amount of gas to fill into the balloon to achieve the desired burst altitude or ascent rate. We use a payload box made of Styrofoam for thermal insulation, with a polythene covering to

protect the payload from moisture. The payload is also covered with reflecting tapes and have blinkers for better visibility at night.

We have developed most of the necessary flight equipment and support systems in-house which will be described in the following sections. The cartoon in Fig. 3.1 shows the major components used in the balloon experiment.

Balloons

The material and size of the balloon determine the altitude and payload weight of the experiment. Currently, we use latex balloons of various sizes such as 1.2 kg, 2 kg, and 3 kg. The weight denotes the maximum weight of the payload that can be lifted by the balloon. Often, we combine 2-3 balloons in order to support our scientific payloads. We fill the balloon with Hydrogen or Helium. For a 2 kg balloon, the diameter of the balloon is around 2 meters, and as the balloon goes up, the balloon expands and reaches a diameter of around 10 meters. Depending upon the actual amount of gas that is filled, the balloon bursts at an altitude of around 35 km.

Flight Termination Unit

One of the main attractions of balloon and rocket experiments is that the instruments can be recovered. To ensure the successful recovery of the payload, we have designed and developed a flight termination unit on the balloon train as shown in Fig.3.1. FTUs can be electrical or mechanical systems. When the required flight time or altitude is achieved, a cut off system gets activated and separates the balloons from the rest of the flight train. This is a fail-safe mechanism to ensure that even if we do not achieve the necessary altitude and the balloons do not burst, the payloads can be successfully brought back to the ground. We use a simple microcontroller based timer unit that is kept for a duration of 2-3 hours. Once the time is elapsed, a transistor switch gets activated and turns a relay on, which is connected to a Nichrome wire that is wound around the rope. The relay is powered on for about 60 s with a current

output of 1 A, which heats the Nichrome wire and severs the rope, separating the balloons from the parachute and rest of the payload assembly. We also keep an additional geo-fencing cutdown, to ensure that the payload falls within a given radius from our launch site. This is especially crucial, considering the geographic location of Bangalore from the coast. The geo-fencing unit is based on a GPS and is triggered when the payload coordinates cross a predefined distance from the launch site.

Parachute

We use a nylon parachute that can support a weight of up to 7 kg. Once the balloons get burst or separated, the payloads start falling freely and the parachute opens and slows down the descent at a velocity of 5 m/s.

Attitude sensor and Pointing system

At the initial stages, the program was used exclusively for atmospheric observations and trace gas analysis. Astronomical observations require a stable pointing system to make sure that the telescope is pointed at the target. We have developed a two-axis pointing system (Nirmal et al., 2016) with an in-house developed attitude sensor (Sreejith et al., 2014). The attitude sensor and the pointing system are made of inexpensive off-the-shelf components. The system employs an HMC 5883L magnetometer for azimuth measurements. The accelerometer and gyroscope values from an MPU-9150 Inertial Measurement Unit (IMU) are used to calculate the altitude. It also employs an iWave GPS receiver unit to obtain the time, latitude, and longitude information. The measured attitude is compared with the desired pointing direction by an onboard computer based on an Arduino Mega. The feedback system employs a PID controller and powers a set of two servo motors for two axis correction. The attitude sensor can achieve a pointing accuracy of $\pm 0.25^\circ$, and the pointing system can reach a pointing accuracy of up to $\pm 0.28^\circ$.

We have also developed a star sensor for fine sensing and correction of the

attitude, again using off-the-shelf components (Sarpotdar et al., 2017). It is a star camera with a wide field of view of 10° with a space-qualified Star1000 CMOS sensor and a mil-grade Spartan-6 FPGA based image processing unit. The FPGA has a catalog preloaded in its memory, along with the algorithms for determining the star patterns in its current FoV. The star sensor implements a centroiding algorithm to find centroids of the stars in the image, a Geometric Voting algorithm for star pattern identification, and a QUEST algorithm for the attitude quaternion calculation. The camera is sensitive to a magnitude of up to 6 and has an accuracy of 30″.

We are currently integrating the star sensor to improve the accuracy of pointing. This combines the values of the attitude sensor to coarsely point the telescope initially and then takes in the values from the star sensor for fine adjustments. As our current balloon program has a weight limit of 6 kg, we plan to test the system at the National Balloon Facility (NBF) of the Tata Institute of Fundamental Research at Hyderabad.

Data Logger

We log all the environmental parameters inside and outside the payload box at regular intervals to assess the health of the instruments and for further analysis and interpretation of the science data. We have developed a data logger with a 32-bit microcontroller. The microcontroller reads the sensors for the inside and outside temperature, pressure, and humidity at regular intervals and stores these values on an SD card. The entire system is designed and fabricated as a rugged and stand-alone box, with a 7V rechargeable Lithium Polymer battery and an LCD display for debugging.

Tracking systems

We employ a two-tier system for tracking the balloon payload. We use a Radio transmitter from Byonics[1] in the payload box. It employs a high altitude

[1]Byonics LLC: `https://www.byonics.com/`

GPS unit and a dipole antenna and sends the live coordinates of the payload at regular intervals. The transmission is through Amateur (HAM) radio frequencies in the form of standard Automatic Packet Reporting System (APRS) packets. In addition to the radio tracker, we use GSM trackers with multiple SIM cards to ensure that there is coverage even in remote locations. We also use a smartphone to use both GSM and GPS tracking after the payload has landed. This is especially important when the payload is in lower altitudes, where a line of sight communication with radio may be difficult.

Ground Support Systems

We use a two-fold system for tracking the balloon and recovering the payload, with a set of antenna and receiving equipment at the CREST campus. The APRS packets are received by the Hoskote ground station and are fed as audio inputs to a computer. The computer decodes the packets, displays the balloon coordinates and altitude on the screen, and plots them on a map to see the live location.

We also use a mobile receiver with a smaller antenna and a portable decoder. This is carried by the tracking vehicle and is vital once the payload comes down and loses line of sight communication with the CREST ground station. The packets are decoded and displayed on an LCD screen.

Flight Computer

We use a Raspberry Pi-3[2] single board computer as the main control and processing system on our experiments. It consists of Broadcom BCM2837B0, 1.4GHz 64-bit quad-core processor, dual-band wireless LAN, Bluetooth 4.2/BLE, and Power-over-Ethernet support. It has four USB2.0 ports and an HDMI port along with a Micro SD port for storing the operating system and data. We use the Wireless LAN and HDMI port to program and debug the RPi.

The RPi interfaces both of our flight cameras: one pointing upwards for

[2]The Raspberry Pi Foundation.: `https://www.raspberrypi.org/`

monitoring the balloons and one pointing along the telescope direction. It also powers and controls the spectrograph for atmospheric observations, with a Python code.

MayaPro 2000 Spectrograph

We use the Maya Pro 2000, an off-the-shelf near UV spectrograph (200 – 400 nm) from Ocean Optics[3] for atmospheric observations. It is a fiber-fed spectrograph with a lens at the end of the fiber for collecting and focussing the light into the fiber. For atmospheric observations, we mount the fiber on the side of the payload box, and for astronomical observations of bright targets, we mount the fiber at the prime focus of a 75 mm parabolic mirror which is mounted on the pointing system. The spectrograph is interfaced with the RPi On-Board Computer (OBC), which does the data acquisition, control, and storage through a Python interface. We have launched the spectrograph on two balloon flights for atmospheric observations, and the results are summarized in the paper Sreejith et al. (2016). We have used Differential Optical Absorption technique (Platt et al., 1979) for estimating the column densities of Ozone in the atmosphere using scattered solar UV radiation.

3.3 Near UV Spectrograph for Balloon Flights

At the initial stages of the balloon program, we used the off-the-shelf spectrograph for our observations. However, it was soon clear that the instrument has some disadvantages when it comes to astronomical observations. One of the major problems is in the readout mechanism, as it consists of a non-photon counting CCD. Astronomical observations of faint sources in the near UV can hugely benefit from having a photon counting detector, due to their low noise. Another problem with the spectrograph was the higher value of dark current, which was also extremely sensitive to outside temperature due to poor insulation. To resolve these issues, we decided to build a custom UV spectrograph

[3]Ocean Optics Inc.: `https://oceanoptics.com/product-category/maya-series/`

with a photon counting detector as the backend. It is a fiber-fed spectrograph in the wavelength range of 250—400 nm (Sreejith et al., 2015). It is a compact instrument with dimensions of 350 × 130 × 45 mm, intended to be flown on our balloon platform or a larger TIFR balloon at an altitude of 40 km. We have chosen a Czerny-Turner (Czerny & Turner, 1930) design which is realized entirely of off-the-shelf components (Fig. 3.2).

3.3.1 Science objectives

Observations in the near and far ultraviolet require platforms at altitudes above the Oxygen and Ozone layers. Our main scientific objective is spectroscopy of the Earth's atmosphere. This is a relatively tractable problem from a platform on high-altitude balloons, as it does not require a high pointing accuracy although pointing knowledge is needed. Since we observe from above 25 km, it puts the payload above most of the atmospheric absorption (primarily O_3 and O_2) allowing us to observe to a short wavelength cutoff of 270 nm. The first scientific objective is the observation of atmospheric emission and absorption features. Trace gas analysis is carried out from scattered/direct solar light observations from the balloon platform. Other objectives include the observation of solar system objects such as comets, where we would be able to observe molecular lines from water, CO, and other species.

3.3.2 Instrument Details

Our spectrograph is a fiber-fed, two-mirror Czerny-Turner design with two spherical mirrors and backend detector is an MCP-based detector as detailed in Chapter 2. The light from the fiber falls on to a collimating mirror of 60 mm. The wavefront then falls on the plane grating of 600 lines per mm, which then falls on the imaging mirror. As we use an off-axis spherical mirror as our entrance aperture, the system is prone to aberrations such as Coma, astigmatism, and distortion. The design is optimized for minimizing these aberrations, especially astigmatism.

One way of correcting astigmatism in an off-axis spectrograph is by using a toroidal grating. As the grating will have different focii for the tangential and sagittal planes, astigmatism can be reduced. However, we found it difficult to get inexpensive, off-the-shelf gratings for the near UV range and custom manufacturing of gratings was outside our budget. So we employed another method of correcting the aberrations, which is by divergent illumination of the grating as explained in Austin et al. (2009). In this method, the distance from the tip of the fiber and the collimating mirror is adjusted in such a way that the wavefront falling on the grating is slightly diverging. This introduces astigmatism in the tangential plane which can be adjusted to cancel out the astigmatism introduced by the mirror.

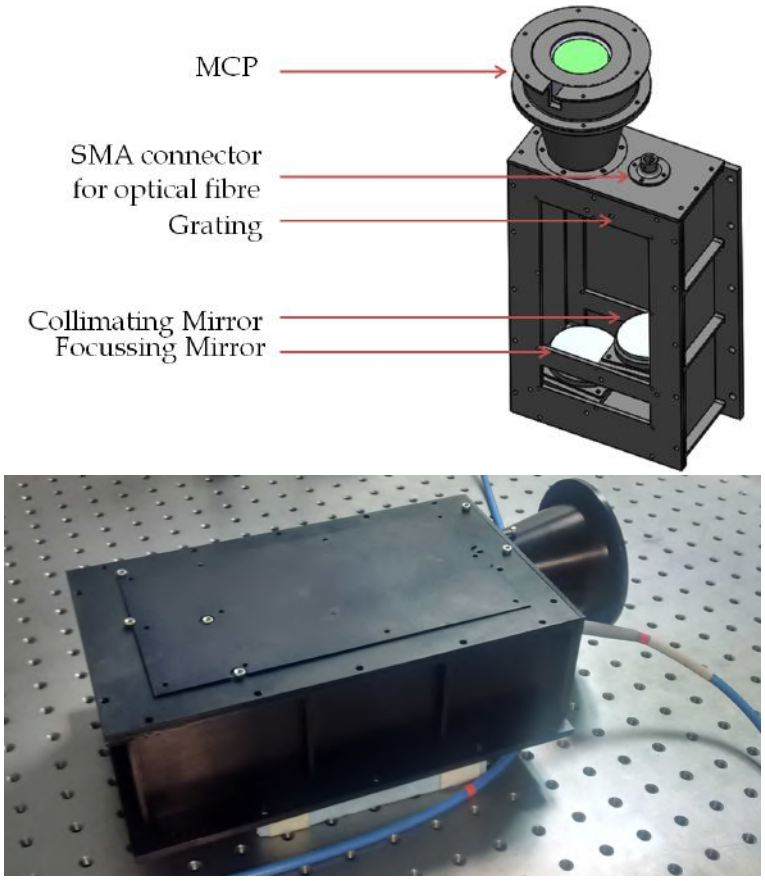

Figure 3.2: *Top:* Near UV spectrograph *Bottom:* Assembled spectrograph in lab.

The mechanical design of the system was done in SolidWorks[4], and the FE

[4]Dassault Systèmes SolidWorks Corporation: `http:solidworks.com`

analysis was carried out in Ansys[5]. The mechanical elements were manufactured in Aluminum because of its lightweight and good structural properties and black anodized to minimize the scattering. The alignment and calibration were carried out as detailed in Sreejith (2017).

3.3.3 System Performance

We use the AB magnitude system (Oke & Gunn, 1983) for defining the photometric parameters of the instrument. The system uses flux measurements that are calibrated in absolute units of spectral flux densities and does not have a reference object such as Vega. In this system, an object with constant flux per unit frequency interval has zero color. The AB magnitude is defined as

$$m_{\mathrm{AB}} = -2.5 \log \langle F_\nu \rangle - 48.6 \,, \tag{3.1}$$

where $\langle F_\nu \rangle$ is averaged across the bandpass monochromatic flux (ergs cm^{-2} Hz^{-1} sec^{-1}) at the mean wavelength λ_0.

The amount of photons detected by the instrument is expressed as the effective area, which is determined by the mirror size, the reflectivity of the mirror and grating surfaces, the coupling and transmission efficiency of the grating, the grating efficiency, and the quantum efficiency of the detector. As most of these values vary with the wavelength, we express it as a function of the wavelength as shown in Fig. 3.3.

$$A_{\mathrm{eff}}(\lambda) = A_{\mathrm{Geo}} \times C_{\mathrm{Eff}} \times T_{\mathrm{Fib}}(\lambda) \times \mathrm{R}(\lambda)^4 \times G_{\mathrm{Eff}}(\lambda) \times \mathrm{QE}(\lambda) \,, \tag{3.2}$$

where A_{Geo} is the effective geometrical collecting area, $\mathrm{C_{Eff}}$ is the coupling efficiency of the fiber, $\mathrm{T_{Fib}}$ is the fiber transmission, R is the mirror reflectivity, $\mathrm{G_{Eff}}$ is the grating efficiency, and QE is the quantum efficiency of the detector. The effective area plot for the instrument is shown in Fig. 3.3.

From Fig. 3.3 *Left*, we can see that the instrument has a peak effective area

[5]ANSYS Inc.: `https://www.ansys.com/`

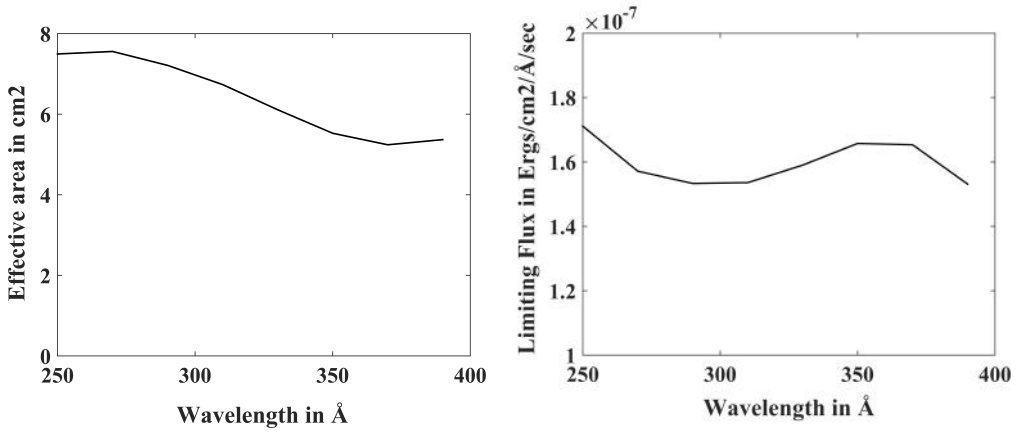

Figure 3.3: *Left:* Effective area of the spectrograph. *Right:* Limiting Magnitude as a function of wavelength

of 7.5 cm^2 at 250 nm and a minimum effective area of 5 cm^2 in the 250 – 400 nm bandpass. We have also estimated the limiting flux that can be detected by the instrument, as a function of the wavelength as shown in Fig. 3.3, *Right*.

3.4 WiFI: Wide Field Imager on CubeSats

CubeSats and high altitude balloons provide a good opportunity to make significant observations at the relatively under-explored regions of the UV spectrum. We have designed and fabricated a wide field imager for the near UV region. The instrument has an all-refractive optics system made of CaF_2 and Fused Silica lenses, to ensure a good transmission of 85-90 % above 250 nm. Since the photocathode of the MCP has good a spectral response from 200 to 900 nm, we can use it in both NUV and visible regions with suitable filters. The detector works in photon counting mode for observing faint UV sources from the upper atmosphere.

We have planned two versions of the instrument: the one we have currently assembled is for the balloon platform with an S20 photocathode that will allow us to observe in the 280 – 400 nm region as explained in Chapter 2. As the upper layers of the atmosphere above 25 km is transparent to these wavelengths, we plan to use this version of the instrument for observing solar system objects and bright transients. We have also planned to replace the

detector with a solar blind CsTe photocathode and modify the mechanical design slightly to fit the instrument in a small satellite. This would open a much lower wavelength of 200 – 300 nm for observations. With a good attitude sensing and tracking, we will be able to observe faster transients from a satellite platform.

In the following sections, we will discuss the various aspects of the design and implementation of the system from the design of optics, choice of components, and an overview of its scientific capabilities.

3.4.1 Science Drivers

Our main scientific interest is the observation of variable sources in the UV sky. We have the wide field of view of 10.8° and moderate spatial resolution of 20″ that would enable us to monitor the sky at a high cadence. UV missions of the past such as *GALEX* have conducted all-sky surveys in the past (Gezari et al., 2013). But one of their main disadvantages has been detector limitations, which forced them to avoid the galactic plane, as it is too bright. Being a small telescope, out brightness limits are much higher than what was allowed for missions such as *GALEX* and *UVIT*, enabling observations into much of the galactic plane. Also, these surveys have been focused on the static sky, and variable sources have been largely under-observed. We plan to do time domain astronomy in the UV with our instrument, by observing Supernovae, Tidal Disruption Events, and M Dwarf flares. We hope to follow up the detections in X-ray and γ-rays and work in collaboration with ground-based observatories for the follow-up.

3.4.2 Instrument details

We are planning to put the instrument on a CubeSat platform after the initial testing, and so, the design of the optical and electronics assembly was done keeping in mind that the payload should fit in a $300mm \times 200mm \times 100mm$ box.

3.4.2.1 Optics

The imager is intended to work at the wavelength range of 250 – 400 nm. We have designed a modified double-Gauss lens system with CaF_2 and Fused Silica lenses for focussing the light onto the MCP. The system consists of 5 lenses, two of which are double lenses. The spot size is adjusted such that the PSF is spread over four pores on the MCP. The lens design parameters are summarized in Table. 3.1. As shown in the table, currently the length of the track exceeds our limit of 200 mm. We are solving this by placing two fold mirrors before the image plane so that the track is folded back to fit in the allotted space.

Table 3.1: WiFI optical system specifications

Number of Elements	7
System Aperture	70
Total Track	250.39
Working F Number	2.98
Paraxial Image Height	19.76
Maximum Radial Field	5.4
Materials	CaF_2 and Fused Silica

3.4.2.2 Mechanical design

The mechanical design and analysis were carried out keeping in mind the launch conditions and vibrations on both balloon and space platform. We have assumed an operating temperature of 10 ±10 °C on the satellite platform and carried out the optical and mechanical tolerances analysis. We plan to maintain the operating temperature with Multi Layer Insulation (MLI) materials. Further temperature control will be provided with temperature sensors and heaters placed on the assembly.

The mechanical components are manufactured in Aluminum 6061-T6, to minimize the weight while maintaining the structural properties. To eliminate the scattering, mechanical components are black anodized, and an additional

baffle tube will be provided. The mechanical structure consists of two parts: the lens holder and the detector assembly. Both are joined together along with a C-shaped payload interface at the center of gravity of the instrument as shown in Fig. 3.4. The lens holder contains the optical elements and the spacers in between. The detector assembly has holders for the MCP and the backend electronics, with the backend PCBs attached to the base plate. The coupling lens is fixed to the PCB holder, and the distance between the lens and the MCP phosphor screen is adjustable with the help of screws.

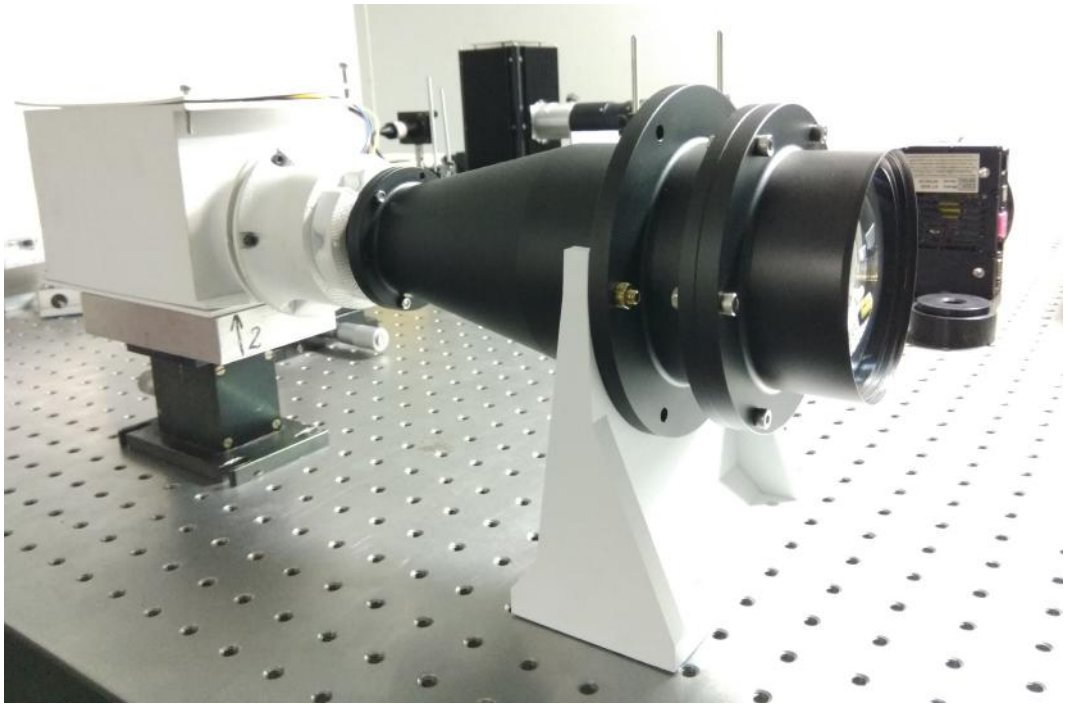

Figure 3.4: Wide Field Imager (WiFI)

3.4.2.3 Detector

The hardware and software architecture of the detector for balloon payload are detailed in Chapter 2. As the S20 photocathode has high QE well into the visible, a filter from Hoya (U-235C) is used to provide a bandpass between 240-390 nm. The filter has a peak transmission of 88% at 320 nm and excellent cut off for wavelength over 400 nm. The filter is kept at a distance of 15 mm from the MCP window.

For the CubeSat application, we are making a few modifications to the detector. CsTe photocathode is employed to make the detector solar blind. It has a QE of around 12% with much lesser dark count as compared to S20.

3.4.3 System Performance

The effective area of the instruments represents the amount of signal collected and transmitted to the detector and is expressed as a product of the geographical collecting area of the primary aperture, the optics transmission efficiency, filter response and the QE of the detector.

$$A_{\text{eff}}(\lambda) = A_{\text{Geo}} \times T_{\text{L}}(\lambda)^7 \times T_{\text{F}}(\lambda) \times \text{QE}(\lambda)\,, \tag{3.3}$$

where A_{Geo} is the effective geometrical collecting area, T_L is the transmission of Fused Silica and CaF_2, T_F is the filter response, and QE is the quantum efficiency of the detector. The effective area plot for the instrument is shown in Fig. 3.5 *Left* for the balloon payload with S20 photocathode and filter and Fig. 3.5 *Right* for the CubeSat payload with a CsTe photocathode. We have estimated a limiting magnitude of 20 for the satellite payload, which translates to a flux level of 2 x 10^{-16} ergs cm^{-2} $Å^{-1}$ sec^{-1} at 250 nm for an SNR of 3 in a 1000 s integration time, which is achievable for a small satellite platform.

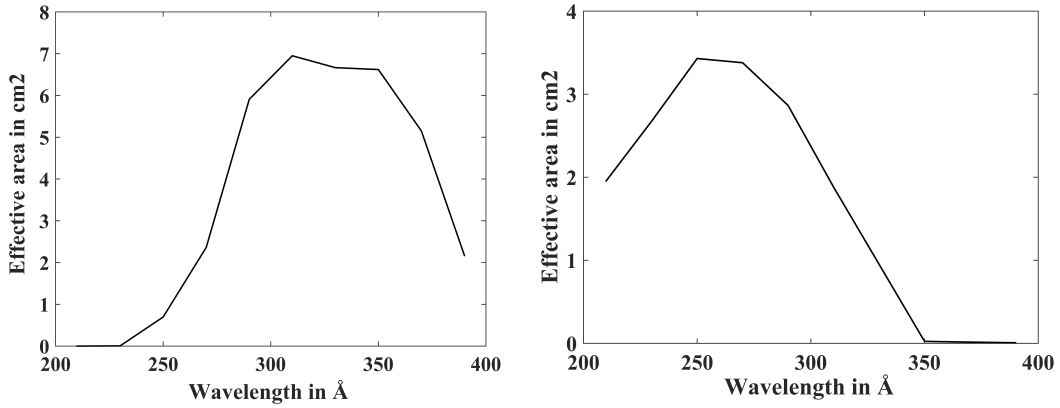

Figure 3.5: WiFI Effective area *Left:* Balloon payload with S20 photocathode and filter *Right:* CubeSat payload with solar blind photocathode

3.5 Future prospects: A long-slit imaging spectrograph

The UV window from 130 – 300 nm covers the spectral domain where a number of atoms have their resonance lines and contains lines from the photodissociation and photoionization of many molecules and atoms. There have been many missions, including the spectrographs on the Hubble Space Telescope, that have made observations in this spectral region. However, most of them were optimized to look at point sources. Moreover, these large missions have a variety of science cases, and it is difficult to get sufficient time to do targeted science with their instruments.

Extended objects such as nebulae and supernova remnants are complex and filamentary, and their physical conditions vary across the objects. We plan to build a Near UV Imaging Spectrograph (NUVIS) for studying extended objects in the sky. Our instrument will be designed to fit in a 6U CubeSat structure, and as we are above the MgF_2 cut off, the technical challenges are minimal. Unlike the Lyman ultraviolet region of 900 – 1216 Åwhere we need windowless detectors and special mirror coatings, we can use traditional solar blind detectors with an MgF_2 window and optics with an Al–MgF_2 or LiF coatings, both of which gives good reflectivity in this region. As the wavelength region does not include the Lyman-α at 1216 Å, the effect of geocoronal scattering from the line is minimized.

The scientific objective is to map the sky using an ultraviolet (130 – 300 nm) long-slit spectrograph with the primary targets being diffuse regions such as supernova remnants and planetary nebulae. We are currently exploring launch opportunities for the instrument, although we are confident that with a standard CubeSat form factor, we will be able to piggyback on other large missions from ISRO or outside.

3.5.1 Science Objectives

We have designed the instrument primarily to look at extended sources, although we have a moderate spatial resolution of 13″ to look at point objects as well. As the background in UV is darker by ∼5 mag (O'Connell, 1987), we can observe very faint objects. Our science program includes the spectroscopic studies of supernova remnants and planetary nebulae in our own Galaxy, star formation in nearby galaxies along with the emission from their extended halos. Some of these phenomena are well-studied by imaging telescopes on GALEX and HST and the spectrographs on FUSE and HST. Recent missions such as UVIT/AstroSat telescopes have given us a new view of the UV sky with unprecedented detail on objects such as planetary nebulae (Kameswara Rao et al., 2018a) and supernova remnants. However, imaging instruments cannot reveal any underlying physics of these objects such as the physical conditions, temperatures, densities, and radiation fields. In addition, these shared resources such as HST and future large missions, cannot be dedicated as much observation time for observations of extended objects. Unlike the existing higher resolution spectrographs on HST and many other UV missions which are optimized for point objects, we would use a long-slit ($4^\circ \times 1'$) to probe the extended regions in a single shot, albeit at modest spectral resolution.

3.5.1.1 Extended Objects

We will be able to map nebulae and other extended objects at moderate spatial and spectral resolution of 13″ and 1200 respectively. We are focused on particular objects and directions, rather than mapping the entire sky. The spectral resolution was chosen to provide a clear separation between the many atomic and molecular lines in this spectral region, particularly the CIV doublet (1548/1551 Å). The spatial resolution is chosen to be able to resolve fine structure in the selected nebulae with a sufficiently high signal-to-noise ratio. Our targets will include supernova remnants, circumgalactic matter, and planetary nebulae which may span over 1 degree in size to probe their spatial structure.

Although previous instruments have observed specific areas in these nebulae at small spatial scales but were not able to trace the large-scale changes over the entire region.

The instrument would enable us to study the various phases of the interstellar medium (ISM), from hot gas in supernova remnants (SNR) to warm gas in planetary nebulae to cold gas in molecular clouds. Supernova remnants are also known to have emissions in the FUV wavelengths, including from H_2 (Kameswara Rao et al., 2018b). Hot gas emits CIV at 1548 and 1551 Å, whereas the NIII line at 1750 Å tracks the warm gas. The cold gas in the ISM is indicated by the Lyman and Werner bands of molecular hydrogen. Such gas has been detected in specific lines through absorption line spectroscopy of quasars (Steidel et al., 2010) but would be better tracked through emission lines in the warm-hot intergalactic medium (WHIM) (Martin et al., 2014). With a long duration observation plan, we will have the freedom to obtain a spectroscopic survey of the sky.

Equally compelling is the UV studies of extended objects in the Solar System. We have to study the objects in our solar system to better understand the conditions on exoplanets. The earlier studies of the UV emission from Solar System bodies already proved useful for the understanding the planetary atmospheres and plasma phenomena. For example, spectroscopy of comets in the UV revealed the presence of new compounds and clarified the mechanisms accounting for their presence (Brosch, 1999).

3.5.1.2 Point Sources

We will also obtain spectra of any point source in the field with a resolution of about 2000. If we have control of the pointing, we may be able to have a fast response to UV transients such as supernovae, GRBs and other explosive events providing crucial diagnostics (Sagiv et al., 2014). As we are a long slit spectrograph with a wide field of view in one direction, we can hope to detect a number of high energy transients in this region. The instrument can also be used to analyze the transients detected by other imaging instruments we

have built, such as the Lunar Ultraviolet Cosmic Imager (Mathew et al., 2017), WiFI (Mathew et al., 2018a), and PIONS (Ambily et al., 2018), and reveal much more information on the detected transients.

Another exciting science goal is the characterization of M dwarf flares. M Dwarfs are known to be hosting planets, and with the launch of Kepler, K2, and TESS, there are a number of detected exoplanets in our galaxy. Photometric measurements could yield valuable information about an extrasolar terrestrial planet, However, by far the most powerful technique available for retrieving the characteristics of planetary surfaces and atmospheres is spectroscopy, which samples the radiation reflected, scattered, or emitted by the planet at different wavelengths. Although we are not sensitive enough to isolate the planet spectrum, our instrument can be used to characterize the bright host stars, especially the flaring ones such as M and K dwarfs. UV radiation from the parent star interacts with the planetary surface and atmosphere as it is scattered and reflected from the planet. These interactions produce characteristic absorption and emission bands. In some cases, the wavelengths at which spectral features are observed can be used to straightforwardly reveal the presence of different types of molecules in the atmosphere via comparison with the known spectral features for gases taken from a spectral line list. Here, the UV stellar spectrum is required to understand atmospheres of planets as it both drives and regulates atmospheric heating and chemistry and is critical to the long-term stability of terrestrial atmospheres, with the key topic in the study of exoplanetary atmospheres is the physics of atmospheric evolution, mass-loss, and retention (Cockell et al., 2016; Kaltenegger et al., 2007).

3.5.2 Instrument Design

One of the constraints on our instrument design is to fit the instrument in a 6U size. The detector occupies a 2U volume, so it is required to fit the optical design within a 4U volume. The challenge is to maximize the collecting area and efficiency of the system. We have decided to adopt a rectangular primary mirror, as it maximizes the collecting area in our given CubeSat volume (Flem-

Instrument type	Long-slit imaging spectrograph
Telescope type	Ritchey-Chretien
Field of view	$4^\circ \times 1'$
Aperture diameter	200 mm x 100 mm (rectangular)
Focal length	350 mm
Operating bandwidth	130 – 300 nm
Slit size	12.5 mm x 50 µm
Grating type	Holographically ruled toroidal
Grating line density	2200 lines/mm
Grating dimensions	35×35 mm
Detector type	MCP with Solar blind cathode
Detector diameter	40mm
MCP Pore size	$10\,\mu$m
Anode type	Phosphor screen
Detector resolution	1024×1024
Spatial resolution	$\sim 12''$
Spectral resolution	0.7 Å (point sources), 1.2 Å (extended sources)
Peak effective area	6.5 cm^2
Sensitivity	15 AB (with SNR of 5 in 1200s exposure)
Dimension (L × W× H)	$300 \times 200 \times 100$ mm

Table 3.2: Summary of instrument parameters for the near UV imaging spectrograph

ing et al., 2018). For a given 200×100 mm space, a spherical mirror of 100 mm diameter can give an area of 78 cm^2 whereas a rectangular mirror gives a collecting area of 200 cm^2.

We have designed a Ritchey–Chrétien telescope with a hyperbolic rectangular primary of 200×100 mm and a hyperbolic secondary mirror (Fig. 3.6). The central obstruction is around 15%. A long rectangular slit of $4^\circ \times 1'$ (100 μm × 20 μm) is placed at the focal plane of this telescope. A rectangular mirror collimates the light from the entrance slit onto a holographically-ruled diffraction grating. The grating is 30mm ×30mm size with rulings of $\sim$ 2200 lines per mm. The light is diffracted and focused onto the imaging plane by the grating. The spectra are recorded on the photon-counting MCP detector,

and the data processing is performed onboard.

Table. 3.2 summarizes the important parameters of the instrument.

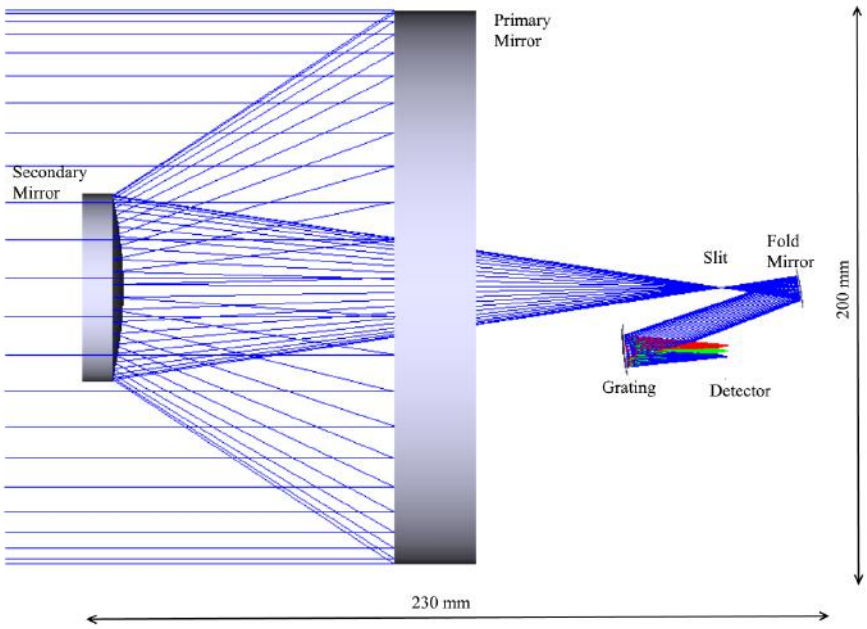

Figure 3.6: Preliminary optical diagram of the instrument

We have done the preliminary optical design in Zemax[6] to estimate the spatial and spectral resolution. Being a wide field instrument, the spatial resolution is poorer at the edges, which prefers a special dumbbell shaped slit as used in the ALICE spectrograph (Stern et al., 2008). However, we have designed the system with a uniform rectangular slit, although it can be later modified.

3.5.3 Performance estimates

The effective area of the instrument is expressed as a product of the mirror size, the reflectivity of the mirror and grating surfaces, the grating efficiency, and the quantum efficiency of the detector. As most of these values vary with the wavelength, we express it as a function of the wavelength as shown.

$$A_{\text{eff}}(\lambda) = A_{\text{Geo}} \times \text{R}(\lambda)^4 \times G_{\text{Eff}}(\lambda) \times \text{QE}(\lambda)\,, \tag{3.4}$$

[6]Zemax LLC: `https://www.zemax.com/`

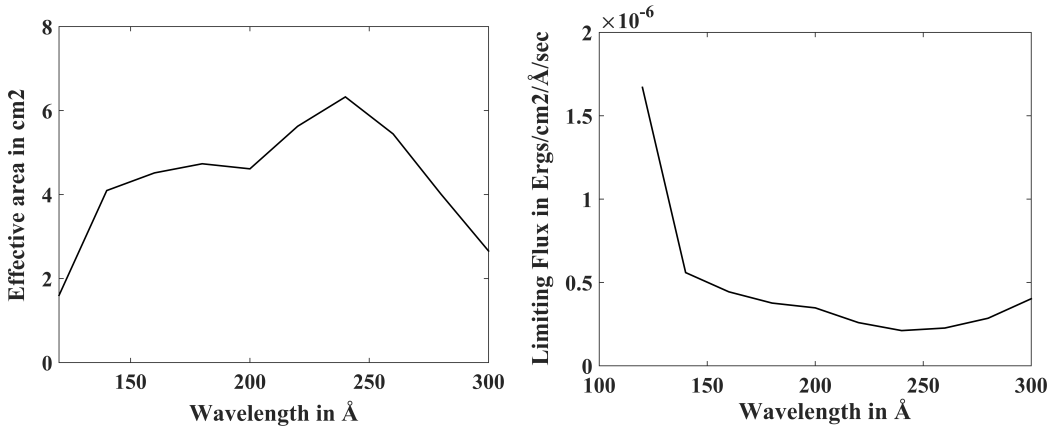

Figure 3.7: *Left:* Effective area of the NUVISS. *Right:* Limiting Magnitude as a function of NUVISS

where A_{Geo} is the effective geometrical collecting area, R is the reflectivity of the mirror and grating coating, G_{Eff} is the grating response, and QE is the quantum efficiency of the detector. The effective area plot for the instrument is shown in Fig. 3.7, *Left*. From the figure we can see that the instrument has a peak effective area of 7 cm^2 at 250 nm and a minimum effective area of 2 cm^2 in the 130 – 300 nm bandpass. We have also estimated the limiting flux that can be detected by the instrument, as a function of the wavelength as shown in Fig. 3.7, *Right*.

3.5.4 Summary and future work

This chapter describes the payloads that use the MCP-based detector as a background instrument. We have finished the assembly and calibration of the balloon payloads, and are readying them for a TIFR balloon launch.

The 6U imaging spectrograph is currently in the design stages, with the preliminary optomechanical design being completed. We have ordered the components for fabricating the detector. The optomechanical design also will be completed in the next couple of months, to finalize the vendors and start procurement.

Chapter 4

PESIT-IIA Imager for Observing the Night Sky (PIONS)

S. Ambily, J. Mathew, M. Sarpotdar, J. Murthy, V. K. Aggarval, S. Nagabhushanam, S. Jeeragal, D. A. Rao, K. Nirmal, Sreejith A. G., M.Safonova, and B.G. Nair, Proc. SPIE 10699, 2018.

4.1 Introduction

Small satellites are changing the way we explore space, by enabling missions that target specific scientific and technical interests. The low cost and faster development schedules of CubeSats enable them to carry out a targeted science and test upcoming technologies for future missions. While large missions aim to make groundbreaking advances in varied areas of astronomy and instrumentation, small telescopes onboard satellites, balloons, or rockets can also make significant contributions at a fraction of the cost (Brosch, Balabanov & Behar, 2014). We, the ultraviolet astronomy group at the Indian Institute of Astrophysics (IIA), are currently focused on building and testing imaging payloads for at astronomical and atmospheric observations in the NUV. We use our high altitude balloon platform for testing the sub-system prototypes and later develop them into full-fledged space payloads.

The ultraviolet region is helpful in studying the chemical composition, densities, and temperatures of the interstellar medium, and the temperature and composition of hot young stars. UV emission is a good indication of high frequency activity and transients such as supernovae, Active Galactic Nuclei (AGN), and Gamma Ray Bursts (GRB). Another exciting science case is the monitoring of bright comets and Near Earth Objects such as asteroids. They have always invoked astronomers' interest both because they are bright enough to be detected easily and due to the possibility of collision with earth.

Compared to the scientific potential, time domain astronomy in the UV is not yet studied extensively. Traditionally transient observations were done in the high energy domains of X-rays and γ rays, and the longer wavelengths of radio and infrared. With the installation of large aperture telescopes and dedicated survey programs such as the Palomar Transient Factory (PTF) on the ground, the rate of detection of transients has increased in the optical wavelengths. The new and upcoming facilities such as the Zwicky Transient Facility and the Large Synoptic Survey Telescope (LSST) are also capable of covering large swaths of the sky to look for variable sources. It is important to complement these observations through space-based observations, as in most cases the UV transient can be observed much ahead in time and can alert the observations from the ground. It is also important to complement the existing and future observatories in high energy and radio (LOFAR, SKA) with corresponding UV observations.

The Pesit/IIA Observatory for the Night Sky (PIONS) is a near UV imaging telescope to be flown on a small satellite developed by the PES Institute of Technology, Bengaluru. The instrument is a 150 mm RC telescope that covers a wavelength range of 180-280 nm. We are using an intensified CMOS detector with a Cesium Telluride photocathode, to be operated in photon counting mode. The telescope has a wide field of view of 3° and an angular resolution of 13″. We plan to point the telescope to scan the sky continuously along the sun pointing axis to look for variable UV sources such as flare stars, AGNs, and other transient events. We have an effective area of 12 cm^2 and can detect

objects as faint as 21st magnitude to perform their photometric analysis. Since the aperture and the effective area of the telescope are small when compared to missions such as GALEX, it can be pointed to relatively brighter parts of the UV sky which were not accessible to larger missions.

4.2 Science Drivers

Space missions such as GALEX, FUSE, and the suite of instruments on HST has demonstrated the fascinating science that can be done with UV observations. Although these missions have surveyed the sky in both Far and Near UV through both photometric and spectroscopic studies, there are many areas in the UV sky that are not well studied. For example, the GALEX mission has imaged around 80% of the sky, with a limiting magnitude of 28. However, due to detector limitations, it has not been able to observe the brightest regions of the sky such as the Milky Way plane. A small dedicated telescope can survey these areas that are typically left out by large missions, with wider science motivations.

Monitoring the UV sky for time variable sources provides exciting science opportunities for future missions (Sagiv et al., 2014). The UV sky is relatively fainter, making a majority of variable sources in the night sky detectable in UV with a space-based observatory. A small imaging payload onboard a CubeSat or nanosatellite can observe bright transient sources such as Supernovae, Active Galactic Nuclei (AGN), and Gravitational wave counterparts (Ridden-Harper et al., 2017). As it is impossible to predict when a star will flare, only continuous monitoring can yield these results. Although UV space telescopes of the past and present, such as GALEX and SWIFT, have resulted in the discovery of many interesting transients, a dedicated program is not feasible with such shared resources but ideal for a SmallSat platform. Recent developments in technologies resulting in larger telescopes and improved detector performances have increased the rate of detection of transients. A wide-field UV instrument, exclusively for transient surveys, can increase the discovery

rate of transients by several orders of magnitude (Gezari et al., 2013).

Late-type stars such as the K and M dwarfs are some of the most active stars in the UV and flare quite frequently with a 10^2 to 10^3 times increase in intensity. There are a large number of these stars in the vicinity (1 kPc) of the Sun with about 75% of the stars being M Dwarfs. There are two reasons why it is crucial to detect and characterize these stars and their flares. As there are a large number of M dwarf flares happening around the solar system, it is essential to identify their sources to detect any extragalactic transients. These stars are also known to have planets surrounding them, and the flares can influence the planet atmosphere. These stars also have a high amount of activity in their corona and strong magnetic fields associated with them. Due to the strong magnetic field and intense UV flares, it was thought that the exoplanets orbiting them are sterile. However, it is also proposed that the intense UV radiation can trigger the formation of biochemical compounds and Ozone. The atmosphere of these planets depend on the irradiation from their host stars and so, to characterize the planets, it is critical to understand the stellar spectrum and the frequency and intensity of the flares. With a large field of view of 3° and low noise photon counting detectors, PIONS will be able to detect such flares with a temporal resolution of upto 2 ms. We are also sensitive to AB magnitudes of 21, enabling us to detect the faint M Dwarfs. Being a dedicated small satellite, we can also do multiple pointings at the same star to obtain its light curves with high photometric accuracy.

A wide field imager can also impact the studies of hydrodynamic escape from short period exoplanets. Hot Jupiters around bright stars are prime targets for atmospheric characterization through transit spectroscopy. These planets show higher transit depths for specific lines in the NUV and/or FUV than what is shown for the continuum, making it possible to characterize their atmospheric profile and detect any mass loss. The NUV region is attractive, as the flux levels are relatively higher. As of now only a small number of bright planets have been observed either through photometry or spectroscopy. For better characterization and modeling it is essential to detect more such

candidates and obtain their light curves in the NUV, which will be possible with our low-noise photon counting detector.

Another important science case that can be explored with modest NUV instrument is the early detection and observation of supernovae (Ganot et al., 2016). Surveying the UV sky for massive star explosions, along with follow up observations using ground based optical and radio telescopes and spectroscopic investigations are critical steps in the detection and identification of these events. Observations of supernovae play a vital role in studying the star formation rates and chemical evolution of the universe. Determining the physical properties of massive stars prior to the explosion is key to understanding and constraining the current models of stellar evolution. The early detection of SNe and the measurement of their light curves are useful to understand the physics of the explosion and the progenitor properties. The first light escaping from an exploding star emerges as a shock-breakout flare, with a hot spectrum peaking in the UV or X-ray bands.

Surveying the UV sky along with optical follow up observations can also play a vital role in understanding the physics and energy of Gamma Ray Bursts (Cenko et al., 2012). They typically are associated with an optical/UV counterpart that lasts between minutes to a few days. Observing the GRB afterglow for events detected by current (Fermi, Swift) and future γ ray missions and possible detection of orphan GRBs without any high energy counterparts can provide valuable constraints to the GRB jet models.

A wide field imager with a high cadence of the order of minutes can be instrumental in understanding the amplitude and temporal scale of the variability of Active Galactic Nuclei (AGNs) as well, which is mainly contributed by the accretion disk (Mushotzky et al., 2011). A high cadence, wide field UV survey can also probe may other exciting science cases such as detection of gravitational wave counterparts (Ridden-Harper et al., 2017), analysis of the variability of quasars and RR Lyrae, and detection of tidal disruption events (Gezari et al., 2012).

We have used the UV sky simulator as described in Safonova et al. (2013)

to model the UV sky as seen by the instrument. The contribution from components such as the diffuse UV background, zodiacal light, airglow, UV bright stars, and the instrumental background is estimated for the PIONS instrument response. This data are combined to generate an output FITS file which gives the total count rate in a given field. The all-sky map as seen by PIONS is given in Fig. 4.1

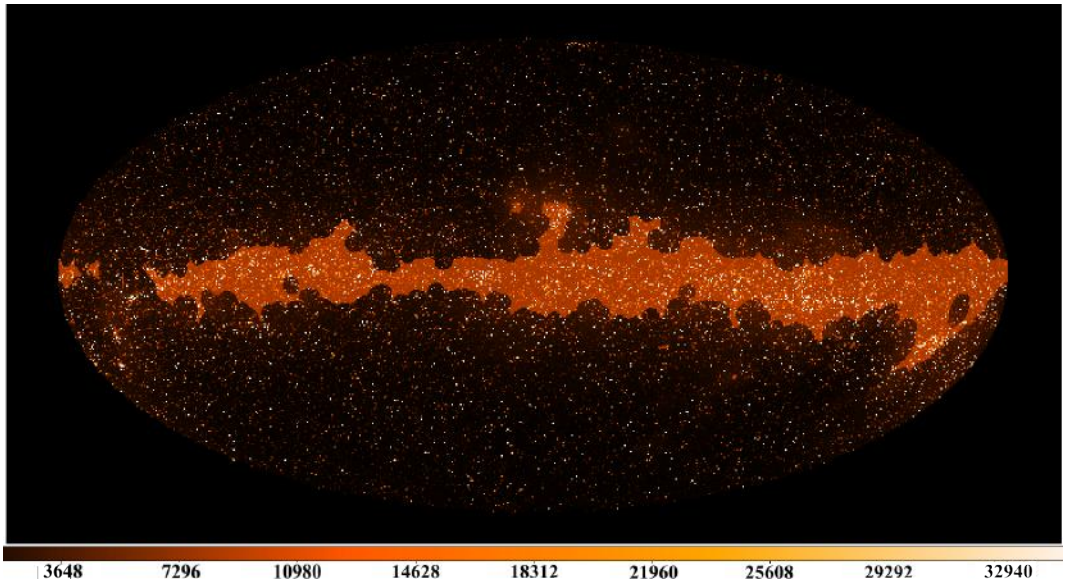

Figure 4.1: Sky as seen by PIONS. The numbers at the bottom indicate the estimated counts in a 1200 s exposure with the effective area estimated in Fig. 4.9.

4.3 Instrument Overview

PIONS is a wide field imager to scan the sky in the near UV mainly to look for variable sources. The instrument is a Ritchey-Chrétien telescope with an MCP based photon counting detector. It covers a wide field of view of 3° making it suitable for surveying large swaths of the sky. The camera has a good spectral response in the 200 – 300 nm region, with the short wavelength cutoff due to the optics and the long wavelength cut off from the solar blind detector. The important instrumental parameters are summarized in Table. 4.1.

Being a small satellite payload, our design is constrained by the weight, volume, and power limitations of the satellite which is roughly of 12U size in

total. One of the main constraints is to limit the length to 300 mm, which places a limit on the focal length of the optical system. The aperture is limited to 150 mm due to the weight and the volume constraints, to fit the instrument within 5 kg and to less than 200 mm height.

Instrument	UV wide-field imager
Telescope type	Ritchey-Chrétien
Field of view	3° (circular)
Aperture diameter	150 mm
Focal length	475 mm
Operating bandwidth	200 – 300 nm
Detector	MCP with Solar Blind coating
Pore size	10 μm
Spatial resolution	$\sim 13''$
Time resolution	2 msec full frame, 10 μs windowed
Sensitivity	21 AB (with SNR of 5 in 1200s exposure)
Weight	$\sim$ 4 kg
Dimension (L $\times$ W$\times$ H)	300 $\times$ 200 $\times$ 200 mm
Power	5.5 W

Table 4.1: Instrument Details of PIONS Imager

4.3.1 Optomechanical design

The optical design consists of a 150 mm primary mirror and a 64 mm secondary mirror with two corrector lenses. Both of the mirrors are hyperbolic to eliminate the off-axis aberrations across the wide field of view, resulting in an RC design. The telescope has a relatively large field of view of 3° for survey purposes. This introduces off-axis image aberrations such as field curvature and astigmatism, which are corrected by the corrector lenses. The optical design data is summarized in Table. 4.2. The optical layout and the spot diagram are shown in Fig. 4.2 and Fig. 4.3 respectively.

The mirrors are made of Zerodur substrate with a reflective Aluminum coating and a protective MgF_2 layer, giving a broad bandpass of 120 – 900 nm.

The set of two lenses, used to correct the aberrations, are made from fused silica, which has more than 90% transmission down to 195 nm. In addition, both sides of the lens are coated with the anti-reflection MgF_2 coating to suppress the reflection and thus maximize the transmission (up to 95%) in the NUV band.

Surface	Radius (mm)	Thickness (mm)	Semi diameter (mm)	Conic constant	Optical material
Primary mirror	-335.28	-102.19	73	-1.24	Zerodur
Secondary mirror	-201.23	-159.45	32	-6.57	Zerodur
Corrector lens 1	54.96	4	15		Fused silica
	89.08	11			
Corrector lens 2	-60.28	3	15		Fused silica
	636.57	10			

Table 4.2: Optical desgin parameters

We have tried to limit the optical aberrations such that 80% of the encircled energy falls within three pores of the MCP as shown in Fig. 4.4. The final PSF will be further affected by the manufacturing and alignment tolerances and temperature fluctuations. We have taken them into account while optimizing the system to ensure the performance for even the widest field of view. Table. 4.3 details the tolerance values used.

The mechanical design was done keeping in view of the satellite and launch requirements such as light weight, small volume, and structural stability to be able to withstand all launch-load vibrations. The natural frequency must be above 100 Hz, and the instrument should be able to withstand shock loads of up to 5 g. Aluminum 6061-T6 is used for the tubular structure of the telescope, due to its high strength-to-density ratio, low outgassing properties, easy machinability, and low cost. The mounts for mirrors and lenses are made

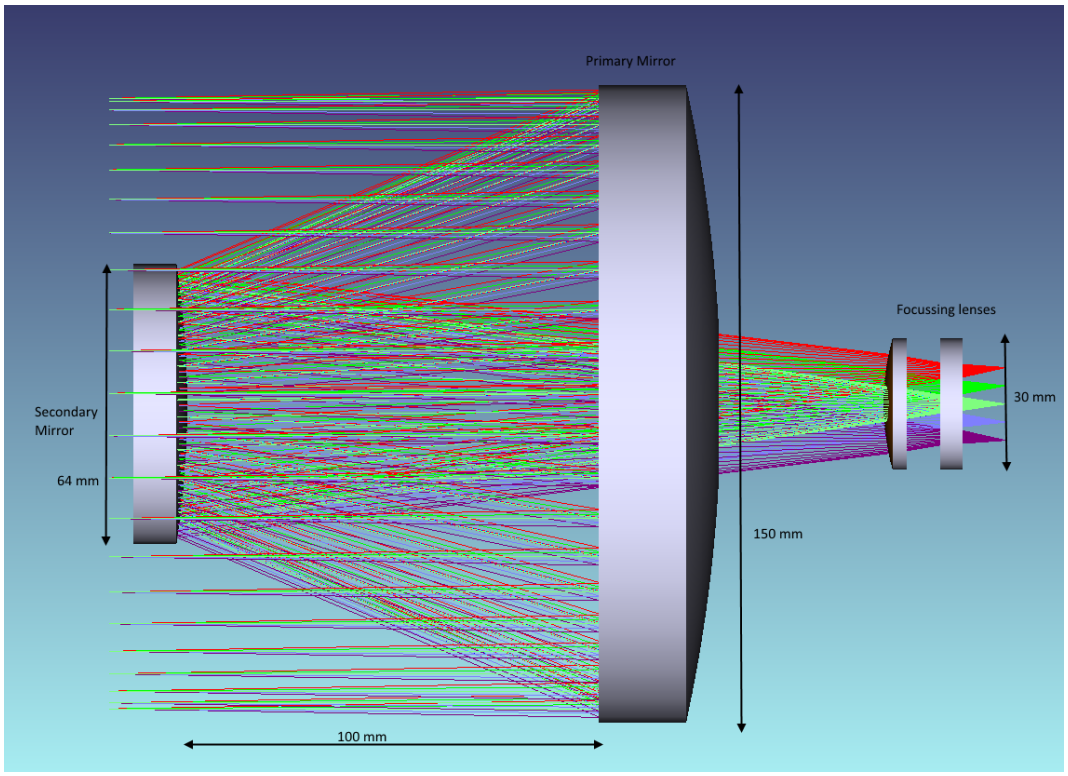

Figure 4.2: Optical Layout

of Invar36 due to its very low thermal expansion properties that match with the Zerodur mirrors. We have used the mechanical design software SolidWorks[1] for the mechanical design and modeling of the instrument. The structural finite element analysis was carried out at PESIT and obtained the natural frequency at 198 Hz. The walls of the telescope tube are painted with Aeroglaze Z306 which absorbs 90 % reflected light, to minimize the scattering.

The CAD model of the instrument is shown in Fig. 4.5 and the exploded view is shown in Fig. 4.6.

4.3.2 Detector

We are using an MCP-based photon counting detector as explained in Chapter 2 as the detector of choice(Ambily et al., 2017). The detector works as a CMOS camera in bright light, transferring each frame serially to the data processing system, and as a photon-counting detector in faint light conditions.

[1]Dassault Systèmes SolidWorks Corporation: `http://www.solidworks.com`

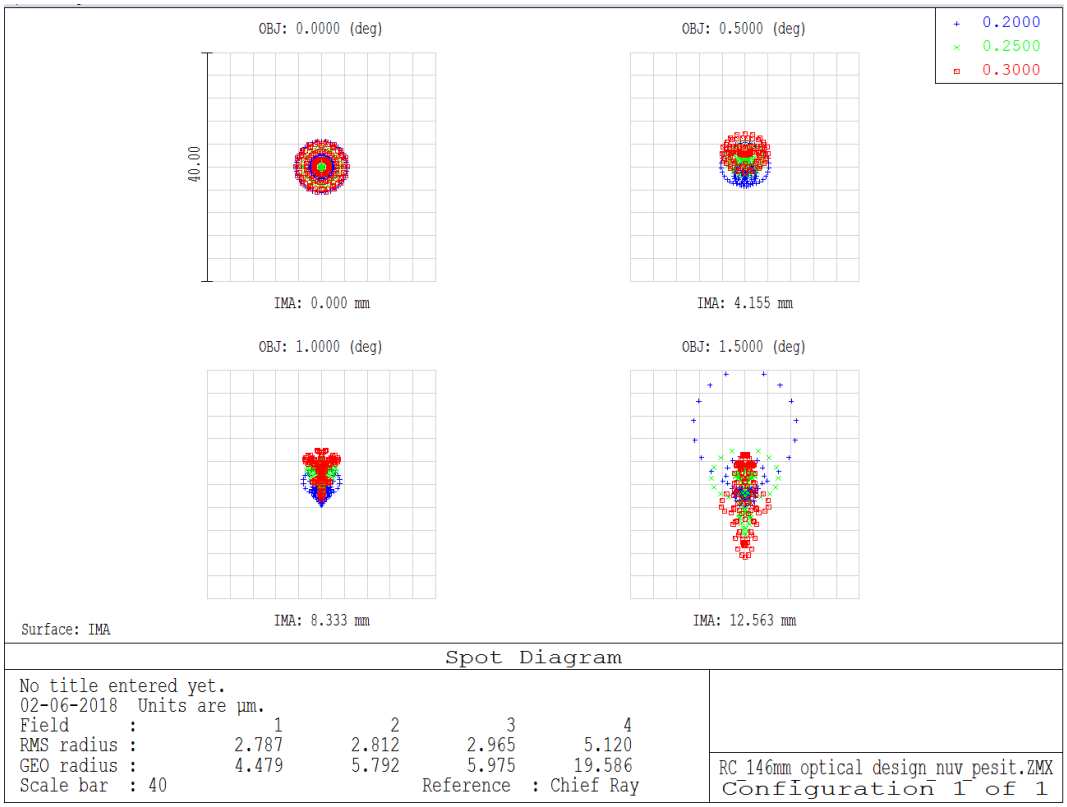

Figure 4.3: Spot Diagram for on-axis and off-axis fields. Colors indicate the wavelength.

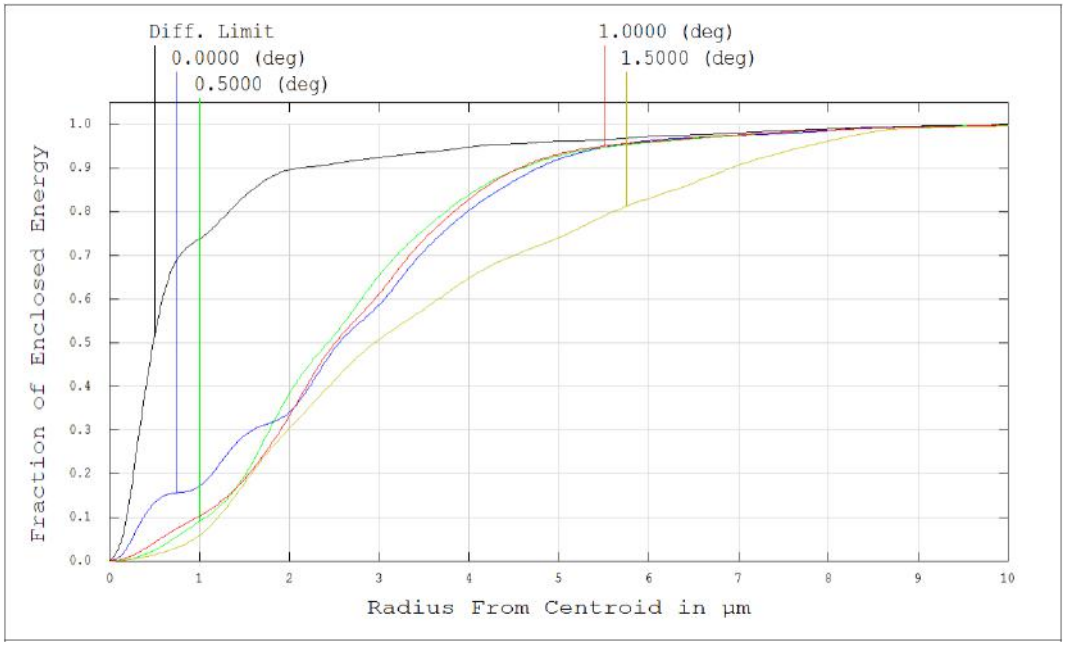

Figure 4.4: Encircled energy. Colours indicate different fields, with offset from the optical axis shown in the plot.

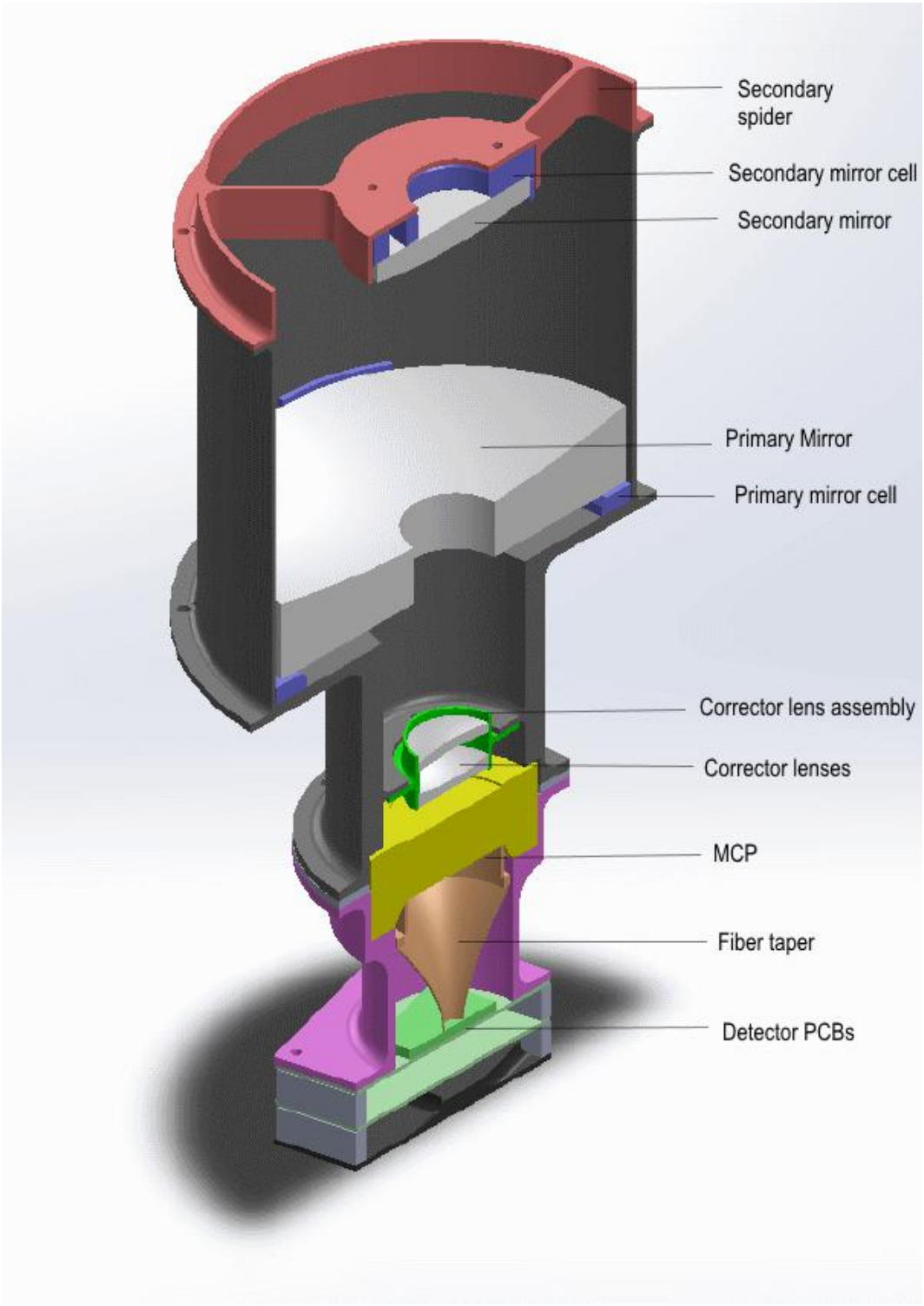

Figure 4.5: CAD model of the PIONS mechanical structure

The laboratory model of the detector had an S20 photocathode with a wide spectral coverage, to suit balloon applications. We have made a number of modifications to the detector to improve its performance and make it suitable

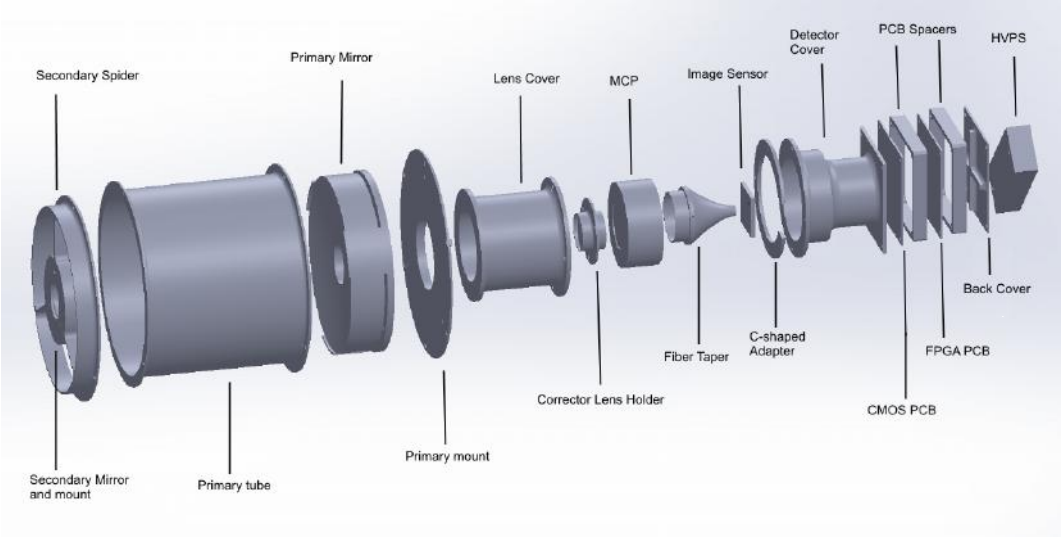

Figure 4.6: Exploded view of the PIONS mechanical structure

Tolerance term	Sub tolerance term	Tolerance value
Manufacture	Radius of Curvature (Mirror)	1 %
	Radius of Curvature (Lens)	0.1 %
	Thickness	50 μm
	X-Y decenter	50 μm
	X-Y tilt	60″
	Surface roughness	$\lambda/6$
Alignment	X-Y decenter	50 μm
	X-Y tilt	60″

Table 4.3: Manufacture and alignment tolerances for PIONS

for the satellite platform.

The new version of the detector employs a solar blind photocathode made of Cesium Telluride to address the red leak and dark current issues seen in the S20 photocathode. We have also replaced the lens-based relay optics with a fiber optic taper as shown in Fig.4.7. This is to minimize the distortions that we see with the lens based system. Besides, a taper is more space efficient, as we can reduce the distance between the MCP output window and the CMOS by a factor of 3.

The following sections briefly mention the main parts of the detector, high-

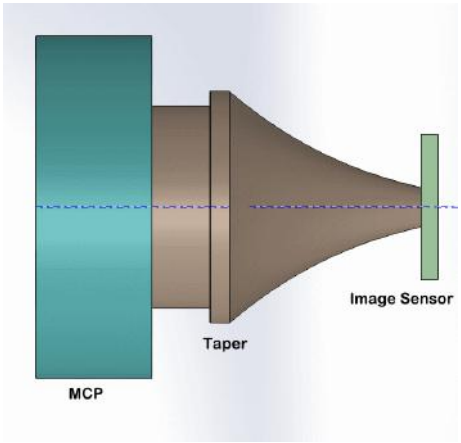

Figure 4.7: Cross section of the modified detector with fiber taper

lighting the modifications.

4.3.2.1 MCP

We are using an MCP340 assembly from Photek. It is a 40 mm, Z-stack MCP with a solar blind, Cesium Telluride photocathode deposited on a quartz input window and a P46 phosphor deposited on the anode. The distance from the photocathode to the MCP front surface is 100 microns, and the distance from the MCP output surface to the phosphor is 700 microns.

The MCP is powered by the FP632 micro-HVPS from Photek which weighs only 100 gm, ideal for the lightweight (< 3 kg) small satellite and balloon platform. The HVPS provides four outputs for the cathode, MCP, and anode terminals with voltages of upto -200 V, 0 V, -2300 V, and 7000 V respectively. The gain of the MCP is set by the voltage at the MCP output, which automatically adjusts the screen voltage, maintaining a constant MCP-out-Anode voltage difference. The resulting electron cloud from the MCP output electrode is accelerated towards the phosphor screen anode (with a peak response at 530 nm), and the resulting photons are focused on the CMOS surface by a fiber taper interface.

The output window of the MCP is coupled to a fiber taper from Photek. The taper has a length of 56 mm with an input diameter matching the MCP size. Compared to the lens system the taper provides a number of advan-

tages and disadvantages. It provides a more efficient coupling with lesser light loss than the lens, resulting in high overall throughput. Being compact and lightweight, it makes an attractive option for the small satellite payload. However, compared to a well-designed lens system, the taper introduces distortions such as honeycomb structures, which needs to be modeled and corrected.

4.3.3 Image sensor

Another significant modification we have incorporated in the detector is with the CMOS sensor. Since we are interested in time-domain astronomy, it is important to have a CMOS image sensor and readout electronics that can support high frame rates. The LUPA1300-2 (NOIL2SM1300A) is a 1.6 MP sensor from OnSemiconductors[2] that meet our requirements of faster readout and larger sensor size. It has 14 μm pixels with $18mm \times 14mm$ size, which gives rise to fewer aberrations when interfaced with the 40 mm MCP. It also operates high-speed clocks of up to 315 MHz rendering a maximum frame transfer rate of up to 500 fps. The sensor further supports windowed and subsampled readouts, which means we can achieve a temporal resolution of 2 ms for the full resolution of 1.3 MP and 10 μs for the smallest window. The high readout rate of the sensor is made possible by clocking the sensor at 315 MHz, with 12 channels of Low Voltage Differential Signalling (LVDS) serial outputs. We have designed a custom readout board to give the necessary bias and clock lines for the sensor. It also interfaces the synchronization clocks and pixel values and to the FPGA board as shown in Fig. 4.8.

4.3.4 Digital readout board

We have already designed a generic FPGA based board for CMOS and CCD sensors (Sarpotdar et al., 2016), which can be used as the digital readout for the detector with minor modifications in the PCB. The board contains the necessary peripherals for storage (SDRAM, Flash, and SD Card) and interfac-

[2] `http://www.onsemi.com/`

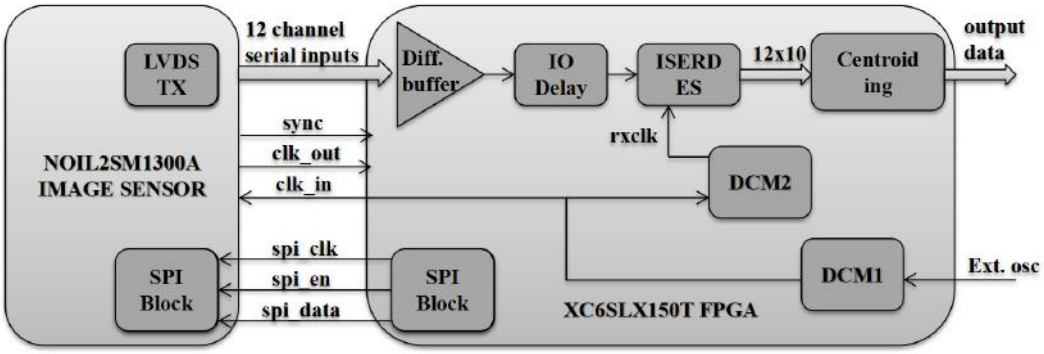

Figure 4.8: Block diagram of the interface between image sensor and the FPGA boards

ing (UART, I^2C, and JTAG). To replace the commercial FPGA used in the XuLA board, we have selected a MIL-grade Spartan-6Q FPGA from Xilinx because of its wide operating temperature range. Since the FPGAs are of the same family, we can port the current image processing algorithms with minor modifications.

4.4 Assembly and Calibration

Alignment and calibration of the instrument will be performed at the M.G.K. Menon Laboratory for space science at the CREST campus of the Indian Institute of Astrophysics. This facility was used for the alignment and calibration of UVIT payload(Kumar et al., 2012) on ASTROSAT and include all the necessary equipment such as Zygo[3] interferometer, theodolites, National Institute of Science and Technology (NIST) photodiodes, SBIG[4] cameras, monochromator, light sources, translation stages, and a UV collimator. The telescope assembly and alignment will be performed in class 1000 clean rooms with laminar flow tables providing a class 100 or better local environment. Procedures will be adapted from the UVIT and the LUCI instrument and, where possible, equipment from these missions will be used.

We use the AB magnitude system for defining the photometric parameters

[3]Zygo Corporation: `https://www.zygo.com/`
[4]Diffraction Limited: `http://www.diffractionlimited.com`

of the instrument. We express the total system response characterizing the instrument's efficiency in transmitting light in terms of effective area in cm^2,

$$A_{\text{eff}} = A_{\text{coll}} \times R_{\text{PM}} \times R_{\text{SM}} \times T_{\text{l}} \times \text{QE}(\lambda)\,, \tag{4.1}$$

where A_{coll} is the effective geometrical collecting area, R_{PM} and R_{SM} are the reflectivity of the primary and the secondary mirrors respectively, T_{l} is the lens transmission and $\text{QE}(\lambda)$ is the quantum efficiency of the detector. The effective area plot for the instrument is shown in Fig. 4.9.

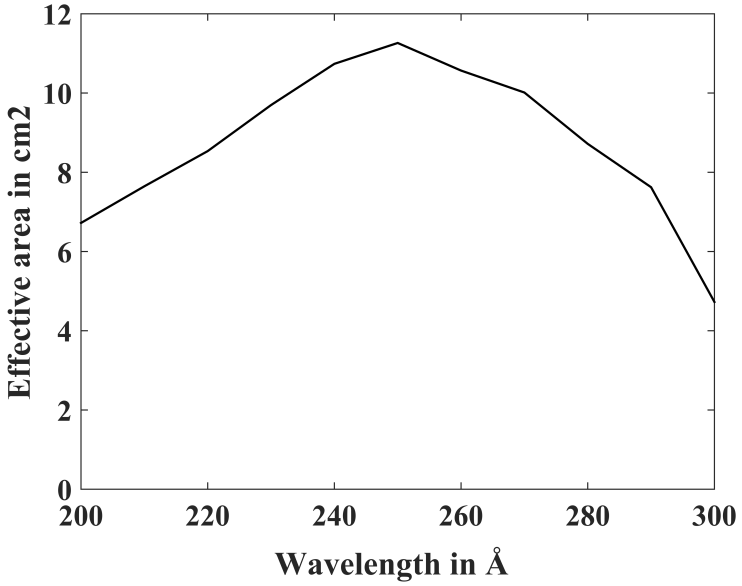

Figure 4.9: Effective area of the instrument after considering the optics efficiencies and detector QE

4.5 Summary and Conclusions

We have described the instrument details for a wide field imager in this chapter. The design and fabrication of all the components are complete and we are carrying out the assembly and calibration currently. The instrument is to be mounted on PISAT-3, a low-cost nanosatellite, designed and developed at the Crucible of Research and Innovation Laboratory (CORI) of the PES Institute of Technology (PESIT), Bangalore, India. The telescope points along the lon-

gitudinal axis away from the sun and provides the opportunity to scan the sky about sun pointing axis either continuously or for long duration observation. In terms of design capability, the control system will be capable of pointing in any inertial direction, with the duration dictated by the permissible power and thermal constraints.

The specifications of the satellite interface are given in Table. 4.4.

Pointing Knowledge	$30'$
Pointing Stability	$1'$/sec
Maximum continuous pointing time	20 minutes
Sun Avoidance Angle	100°
Data rate	10 kbps
Temperature Range	$10\pm10^\circ$ C
Weight	$\sim$ 4 kg
Dimension (L $\times$ W$\times$ H)	$300 \times 200 \times 200$ mm
Power	5.5 W

Table 4.4: Satellite interface details for PIONS

Chapter 5
Development of Far UV Detectors and Instrumentation

5.1 Introduction

This chapter describes the development of detectors and other instrumentation for far ultraviolet observations from space. The FUV spectral window from 912 to 1800 Å is one of the most exciting bandpasses with a greater density of absorption and emission lines, including many important diagnostics of the physics of the interstellar and intergalactic media (ISM and IGM), star-forming regions, and planetary atmospheres. There is an increased interest in the FUV, especially from 912 to 1216 Å, in recent years, as we are looking for the next large decadal mission to replace the Hubble Space Telescope (Kouveliotou et al., 2014). One of the proposed missions is the Large UV/Optical/IR Surveyor (LUVOIR), which is a multi-wavelength space observatory operating from 0.1 μm to 5 μm. For the flight qualification of technologies in support of future missions, many smaller instruments need to be developed and tested on CubeSats and sounding rocket platforms.

We plan to venture into the more challenging FUV region by designing and building detectors and spectroscopic instruments at IIA. The technological

challenges of moving from NUV regions to the shorter wavelengths are onerous, although the time and cost associated with developing a CubeSat payload make it an attractive platform for acquiring the technological know-how. One of our key science motivations is the observation of extended objects in the galaxy to learn about their evolution, and the characterization of stellar atmospheres with the aim of assessing the habitability of their planet atmosphere. This also closes a gap in recent observations, as there have not been any astronomical payloads targeted at these wavelengths since the FUSE and SPEAR (Edelstein et al., 2006) missions. The payloads on planetary missions such as ALICE (on New Horizons and Rosetta Lander) and UVES (on Juno) have carried out observations in these wavelengths.

Another topic that is dealt with in this chapter is the fabrication of an FUV detector in-house, with custom coated photocathodes. To cover the entire region of 912 – 1800 Å, we need a windowless detector with a wide response. In that case, the photocathodes are to be directly deposited on the MCP. As a first step, we deposit CsI photocathodes on an MgF_2 window and characterize the performance of films of varying thickness. Although this limits the sensitivity in the shorter wavelengths below 1200 Å, it helps us refine the deposition process and achieve an optimum thickness value for the photocathode. As windowless detectors are difficult to handle and needs to be maintained in vacuum, this exercise also gives us the technical know-how on handling the vacuum.

5.2 Development of FUV detectors

Detectors are one of the most critical and expensive components of any space-based instrument. As mentioned in Chapter 2, MCP-based photon counting detectors generally consist of a photocathode, electron multipliers (MCP), anode, and readout electronics. The photocathode is a negatively charged electrode that is coated with a photosensitive compound. When photons of sufficient energy strike this, the absorbed energy causes electron emission due

to the photoelectric effect. Properties of the photocathode can determine the sensitivity and resolution of the instrument.

An MCP photocathode consists of a photosensitive material coated either on the front surface of the MCP or on a protective window that is kept before the front surface with close spacing, in order to minimize the divergence of the generated electrons. A thin wire grid is kept at a negative potential to repel electrons inside the detector. The type of the coated material determines the sensitivity and the quantum efficiency of the final detector. The grain size of the deposition determines the resolution of the detector. For photon counting detectors, the main source of noise from the detector is the dark current, which is also dependent on the type of photocathode. The coatings are made of alkali halides or multi alkali materials, with Cesium Iodide or Potassium Bromide photocathodes being the most commonly used for far ultraviolet observations. Solar blind materials such as Cesium Telluride and Rubidium Telluride are widely used for near UV experiments as their response reduces towards the longer wavelengths above 300 nm. For responsivity in the longer wavelengths, multi-alkali photocathodes such as S20 are used. There are two modes of integrating a photocathode on the window the opaque and semi-transparent mode as shown in Fig. 5.1. In the semitransparent or transmission mode as shown in *Right*, the electrons are transmitted through the window to a thin layer cathode material which emits the electrons. In the opaque mode or reflective mode, the electrons are emitted towards the same side of incoming photons with a charged mesh grid to direct the electrons to the electron multiplier. The opaque mode may give higher sensitivity and quantum efficiency, as it allows for thicker coatings. However, due to the unusual trajectory of the photoelectrons, it is less commonly used in imaging applications.

As part of our program to develop compact, low-cost instruments for UV observations, we are working on fabricating a far UV detector in-house. As the first step, we have studies the properties of various thin film photocathodes on a MgF_2 window in semi-transparent mode. The sensitivity of commonly used CsI and KBr photocathodes in opaque (solid lines) and semitransparent

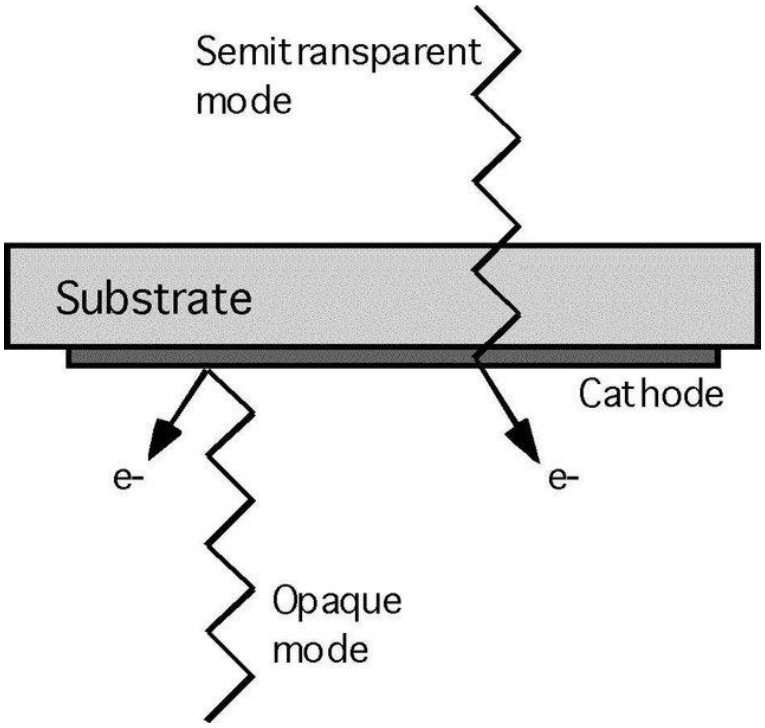

Figure 5.1: Photocathodes in semitransparent and opaque mode. *Image credits: Siegmund et al. (2008)*

(dotted lines) modes are shown in Fig. 5.2

5.2.1 Coating Procedure

We used the deposition facilities at the High Energy Physics laboratory at the Indian Institute of Technology (BHU) Varanasi for the thermal evaporation and deposition of Cesium Iodide and Potassium Bromide photocathodes on a 25 mm MgF_2 window (Jammal et al., 2018). All the necessary equipment for deposition and testing are available in the facility. The deposition is done in a stainless steel chamber of 45 cm diameter as shown in Fig. 5.3. The high purity (5N) CsI and KBr crystals are procured from Alfa Aesar (Triloki et al., 2015)(Rai et al., 2017). The deposition chamber is maintained at high vacuum with the help of a Turbo Molecular Pump (TMP) from Pfeiffer, capable of achieving a high vacuum of 10^{-7} Torr, which is powered on about 8 hours before the process.

Once the necessary pressure is achieved, the CsI/KBr crystals are kept on

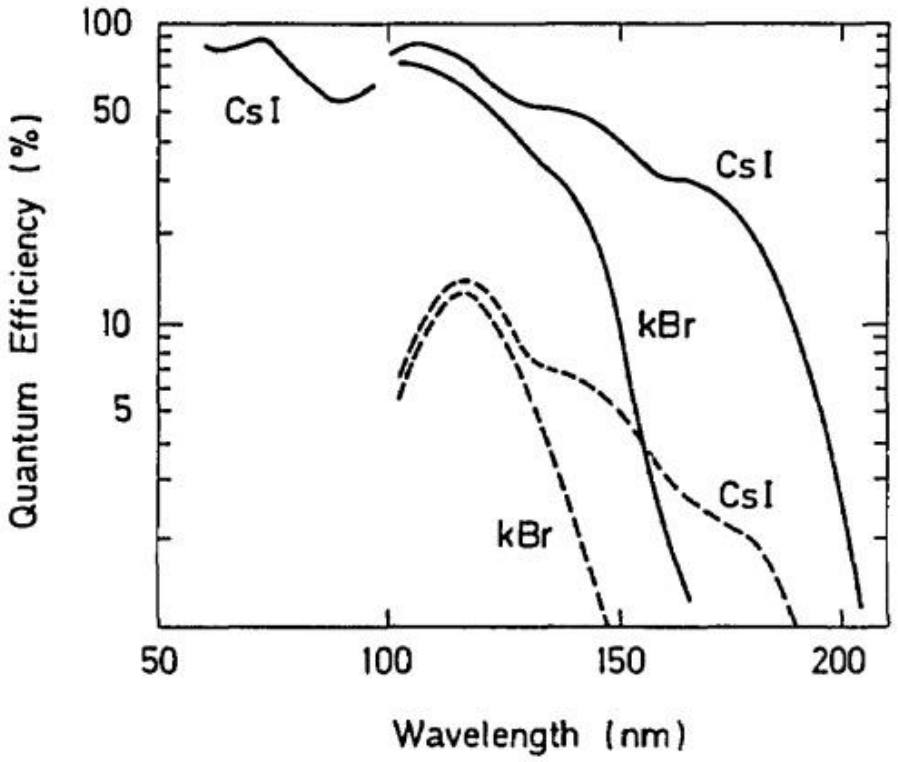

Figure 5.2: Sensitivity of commonly used FUV photocathodes in opaque (solid lines) and semitransparent (dotted lines) modes. *Image credits: Coleman et al. (1981)*

a platform made of Tantalum and heated for outgassing. A mass spectrometer from Stanford research Systems RGA200 was used as residual gas analyzer inside of the deposition chamber and to ensure that the chamber is dominated by Nitrogen. The MgF_2 substrate is cleaned with acetone and mounted at a distance of 20 cm from the crystals. The coating is done by resistive vapor deposition with a high current of 80 A passing through the tantalum to evaporate the CsI/KBr crystals. The thickness of the coating is monitored in real time with the help of a thickness monitor from Sycon Instruments (STM-100). It is a crystal oscillator which is placed beside the MgF_2 substrate. The coatings get deposited on the crystal with the same thickness as the substrate, whose frequency varies as the thickness of the material deposited increases. The rate of deposition is controlled by varying the current, and we maintain a rate of 2 nm/s.

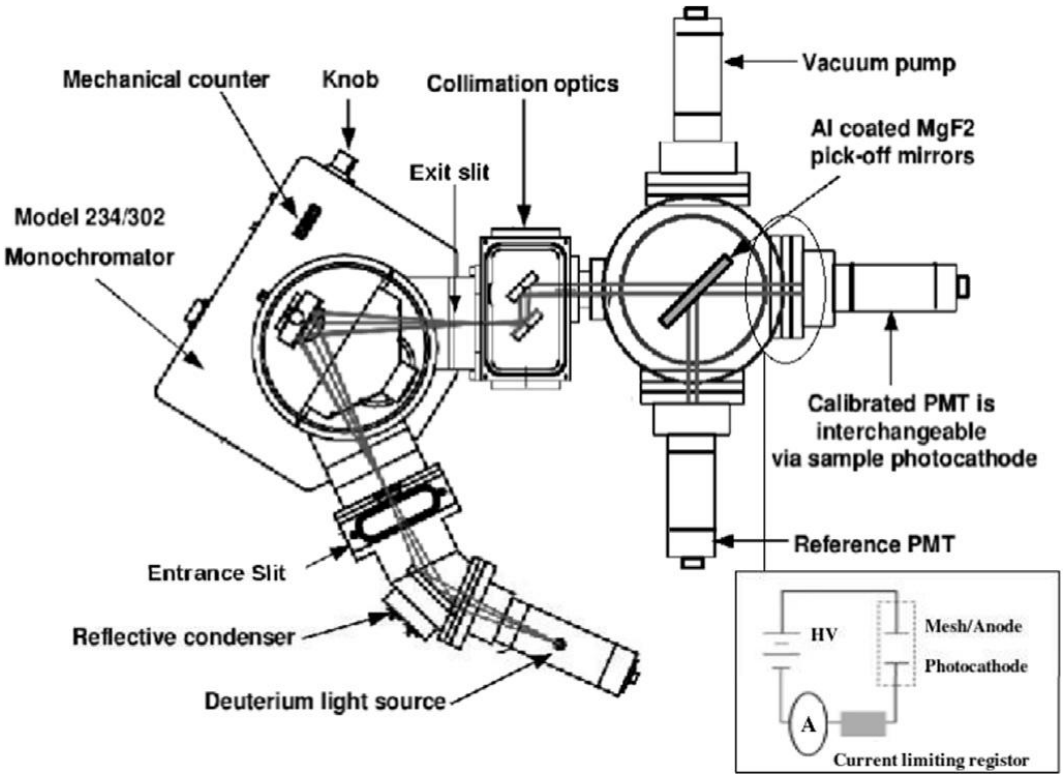

Figure 5.3: Deposition procedure at BHU. *Image credits: Triloki et al. (2015)*

5.2.2 Experimental setup

After the necessary thickness is achieved, we transfer the coated substrate to a desiccator filled with dry N_2, with a small pump. Afterward, the sample is moved to the measurement and characterization chambers. It is important to monitor the ambient humidity while depositing and measuring, as it is desired to shield the samples from moisture.

5.2.3 Measurement of photocurrent and quantum efficiency

We use the setup shown in Fig. 5.3 for the measurement of photocurrent and quantum efficiency (QE) of the cathode (Triloki et al., 2015). The measurement chamber is kept at a pressure of the order of 10^{-4} Torr. A deuterium lamp, emitting 30 W energy in the 120 – 380 nm wavelength range, is used for the input light. A Vacuum UV monochromator from McPherson is used

to select the required bandpass with 1 Å resolution. The sample is mounted on a Copper ring to establish electrical connection with an anode of +200 V kept at a 2 mm distance. A Keithley picoammeter measures the resulting photocurrent from the cathode at an interval of 1 nm. We use two sets of Photomultiplier Tubes (PMT) from Hamamatsu for the QE measurement. An Aluminum pick-off mirror is kept in the beam path to redirect the light to the two arms, with the PMT in the reference arm illuminated continuously to monitor the stability of the Deuterium lamp. The measurement arm can be interchanged with a calibrated PMT and the sample, and this PMT is calibrated against a NIST vacuum photodiode for measuring the absolute QE.

5.2.4 Measurement of optical properties

For semi-transparent photocathodes, it is important to measure the optical properties of the photocathode, especially the transmission and absorption properties. The measurement uses a similar setup to that of the QE measurement except that instead of the PMTs and the ammeter, we use spectrophotometer from Perkin Elmer to measure the output light from the cathode. The input from the lamp is compared against the spectrophotometer readings for the same wavelength regions, to estimate the percentage of transmission.

5.2.5 Results and Analysis

Since we did not have a calibrated Photo Multiplier Tube, we have measured the photocurrent measured for the 12 nm film and compared it with the input photocurrent from the D2 lamp (Fig. 5.4). The value is very low because for very low thicknesses the grain size of the deposited films will be too low and hence we can see large pores on the surface(Triloki et al., 2014) (Rai et al., 2016).

We have coated the MgF_2 window with three types of the photocathodes: 12nm CsI, 50nm CsI, and 50nm KBr. The transmission properties of the coated CsI films are measured and plotted as shown in Fig. 5.5. Although,

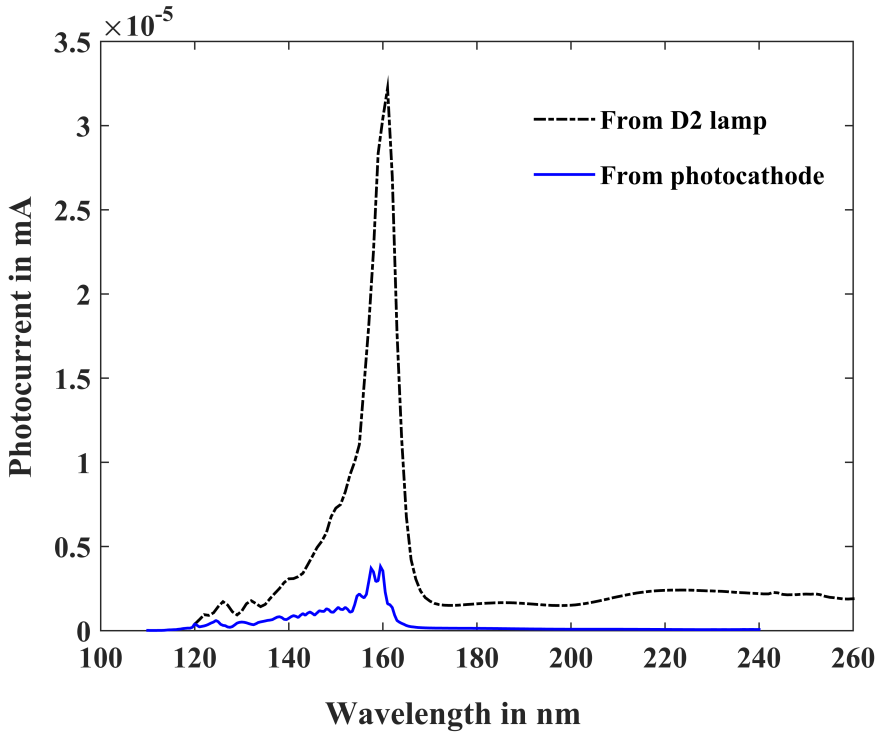

Figure 5.4: Photo current measured with the 12 nm thick CsI film (solid, blue line) overplotted with the photocurrent from the reference Deuterium lamp (dotted, black line).

ideally the 12 nm should have higher transmission it shows lesser transmission due to being exposed to higher humidity (65% vs. 55%)(Triloki et al., 2012) (Rai et al., 2015).

5.2.6 Conclusion and Future Work

We have coated semi-transparent KBr and CsI thin films on a 25 mm diameter MgF_2 optical window, with an optimum thickness for maximum QE and transmission. We realized the need to have better ways to monitor the ambient conditions, to ensure uniform properties for the films. To get a further understanding of the properties, it is important to know the morphology of the deposited films through X-ray diffraction and electron microscopy.

To achieve the final goal of assembling the detector, we have procured a bare MCP of 25 mm diameter from Photonis. The photocathode assembly needs to meet the stringent requirements that the spacing between the two elements should be kept at 100 μm and the assembly should be carried out in

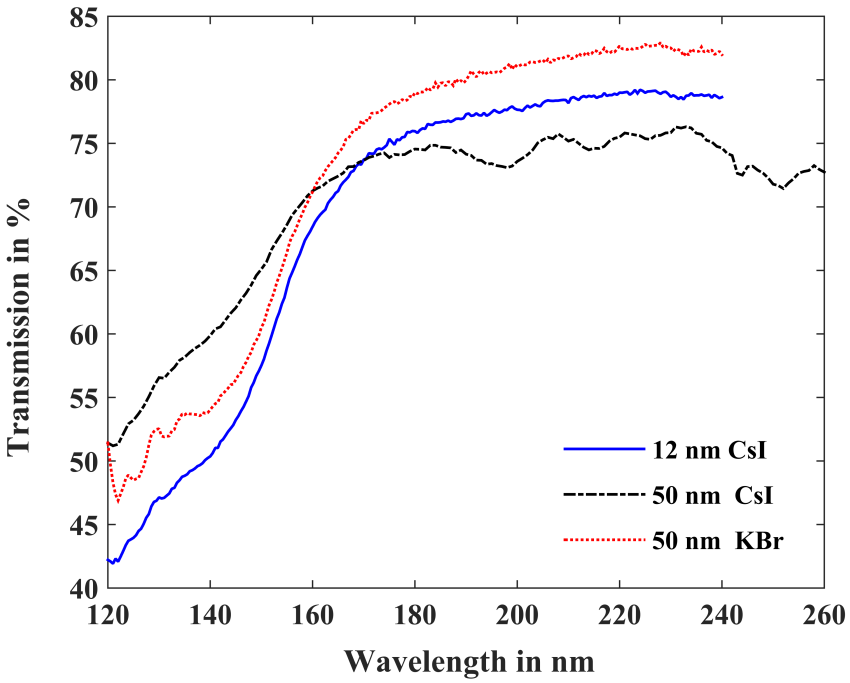

Figure 5.5: Transmission Curve for photocathodes on MgF_2. The blue solid line represents a 12 nm CsI film, the black dashed line represents a 50 nm CsI film and the red dots are for a 50 nm KBr film.

a vacuum sealed environment. The detector assembly should be hermetically sealed with proper electrical connections for biasing the electrodes (Conti et al., 2018).

5.3 SING: A Far Ultraviolet Imaging Spectrograph

Observations in the Lyman UV (LUV, 912 – 1200 Å) are important to detect many of the key physical tracers from the local Universe (redshift, $z < 0.1$). Despite this, there has never been an astrophysics mission with both sub-arcminute spectral imaging capability and high sensitivity in the LUV. Of the major UV space missions, only Copernicus and FUSE have covered the entire FUV from 912 Å with IUE and HST covering from above 1150 Å. This has hampered our efforts to study many of the astronomical and cosmological

phenomena, especially in the local universe. Further, these were intended for observations of point sources, with multiple observations spread over weeks required for extended sources, which is not possible to obtain with a large mission with multiple science priorities. While imaging surveys such as GALEX and UVIT have mapped the sky with high spatial resolution and revealed interesting morphological features of these objects in great detail, spectroscopic studies are indispensable to obtain crucial diagnostics necessary to understand the local physical conditions. Spectroscopy in the FUV, especially the in LUV region, can reveal a great detail on the conditions of the interstellar and intergalactic medium, inflows, and outflows into AGNs, and the frequency and intensity of stellar flares to assess the habitability of their planets.

Space missions in India are also looking to expand their horizons by venturing into bigger and more complex space missions in the future. The success of ASTROSAT/UVIT has raised new questions about the ultraviolet sky which may only be answered through spectroscopy. For the successor missions to ASTROSAT and the upcoming planetary missions, FUV instruments can provide a scientific advantage. On missions such as New Horizons to Pluto and Juno to Jupiter, the FUV spectrographs provided fascinating observations on their atmosphere.

We have proposed to build a long-slit, imaging spectrograph designed for operation in the spectral range between 900 and 1800 Å. The instrument fits in a 6U CubeSat volume. Since the scientific potential of this spectral region is largely unexplored, even a CubeSat or small satellite carrying a spectrograph with moderate spectral and spatial resolution can carry out significant science. As we are particularly interested in studying the physical conditions of extended objects such as planetary nebulae and supernova remnants, we have a spectral resolution of about 1 Å, sufficient to separate the OVI doublet and to resolve the molecular hydrogen bands. We have chosen a long slit with an extent of 4° and a width of $1'$, ideal for spectroscopy of extended sources. The instrument has a spatial resolution of $13''$ over the 4° field of view. The detector has a 40 mm Gallium Nitride (GaN) photocathode with a peak effi-

ciency of 70% and a resolution of 2048 x 2048. This spectral range necessitates a windowless detector which will be provided by the Institute of Astronomy and Astrophysics (IAAT) at the University of Tübingen (Conti et al., 2018).

5.3.1 Science goals of SING

SING is primed to be one of the first FUV sensitive spectroscopic surveys of extended objects in the sky, giving us key insights into the physics of galaxy evolution, interstellar and intergalactic medium, and Active Galactic Nuclei. One of our primary objectives is to understand how galaxies acquire, process, and expel gas, which can give us clues on galaxy formation and evolution (Tumlinson et al., 2013). Understanding how gas gets cycled through the circumgalactic, intergalactic, and interstellar medium during the chemical evolution of galaxies is of fundamental importance to this. The SING spectral region covers many lines that can track gas in various temperatures 10^2 to 10^7 Kelvin (Tumlinson et al., 2012), with the most important of them being the OVI doublet (1032/1038 Å). In addition, the CIV doublet provides vital diagnostics to the hot gas (1548/1550 Å), as does the CIII and NIII lines from the warm gas. The Lyman and Werner bands can track the cold gas in the ISM. There have been only very few studies of these crucial lines because of the lack of data, and we will obtain spatial and velocity information of the extragalactic hot gas in clusters of galaxies, in individual galaxies and AGNs, and in the intergalactic medium. Through these observations, we will trace the abundances, line ratios and velocities of the gas over the extended regions. In conjunction with X-ray and radio images, we will obtain a complete physical model of the gas.

Tracking the emissions from gas flows, especially from the IGM and CGM have proved difficult due to its faint and diffuse nature. Most of the observations so far have been done indirectly through absorption spectroscopy from quasars. This in itself has been proved difficult, as UV-bright quasars in nearby bright galaxies are rare. In addition without access to the LUV, the nearby universe is closed for observations, as we need higher redshifts to bring them

to the observable regions of existing HST spectrographs. The LUV capability of SING would enable us to cover the nearby universe increasing the number of observable quasars. SING would also enable us to do emission line spectroscopy in the LUV, especially in the OVI doublet to track hot gas, in and around galactic clusters. This would also help address the missing baryon problem, by explaining the abundances of chemical elements in the galactic matter with respect to the dark matter halos. Estimating the hot and cold gas in CGM may reveal a higher percentage of baryons in the galactic halos than expected, explaining why the currently estimated abundances are much lower in low redshifts. Spectroscopy in the LUV will help access the tracers for gas at various temperatures required to probe the CGM at low redshifts.

The FUV also contains tracers to understand structures in our own galaxy, from spectroscopy of the interstellar medium to the structure of supernova remnants. When the shock breakout from supernovae pass through the ISM and CSM, it changes the temperature and energy of the gas within. These give rise to optically bright filament structure that has been recently observed by UVIT for the Crab and Vela supernova remnant (SNR). However, imaging from UVIT or GALEX cannot reveal the temperature and physical conditions in those regions. These structures were previously observed for the Cygnus Loop with FUSE but constrained observations from only one region of the structure. It is essential to track the emission lines from the extended region of the objects to understand the structure and evolution of filaments, which would require multiple observations with facilities such as FUSE. With a long-slit imaging spectrograph like SING, this can be done in a single pointing. We have shown a simulation of lines from a filament in the Cygnus Loop in Fig. 5.6 with that of a 15^{th} magnitude B star.

Another science interest of SING is the emission line studies of planetary nebulae. Recent observations from UVIT found extended emission in FUV observations of the planetary nebula NGC 40 (Kameswara Rao et al., 2018a) and NGC 6302 (Kameswara Rao et al., 2018b), indicating the presence of molecular hydrogen. Spectroscopy is required to map the gas over the entire

nebula and understand the processes. The instrument also works well for observations of outflows and inflows from AGNs. A large fraction of AGNs has strong outflows of ionized gas, which pushes back the infalling gas, thus limiting gas accretion onto the AGN in a process called negative AGN feedback. There may also be positive AGN feedback, due to gas flowing back onto the AGN and forming stars (Maiolino et al., 2017), with a comprehensive survey required to understand when the two are important. Positioning our long slit across such a galaxy or cluster of galaxies would allow us to map the velocities at different radii. Another aim is to study the UV sky background. Although the ultraviolet background radiation is well-understood above 1300 Å, as summarized in Murthy (2009), significant observations have not been done in the lower wavelengths so far. Even with moderate spectral and spatial resolution, we can study the sources and nature of the diffuse background and get an overall picture of its spectral energy distribution in the UV.

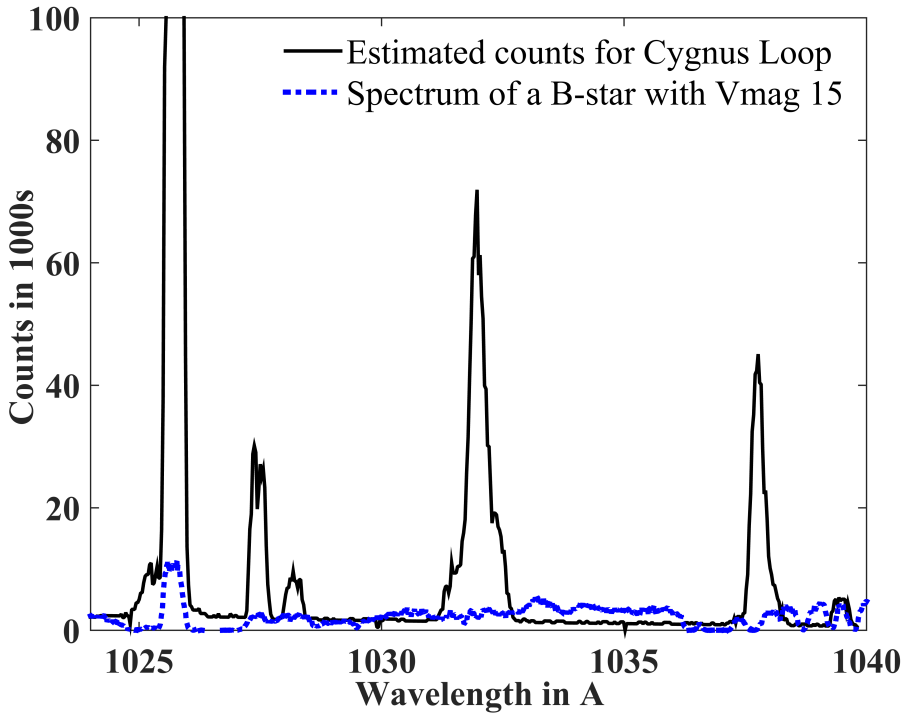

Figure 5.6: Simulation of lines from a filament in Cygnus as observed by SING (Solid, black line). Spectrum from a 15^{th} magnitude B star is also plotted (Dotted, blue line).

Observation of transients can also benefit from an FUV spectrograph.

These include supernova explosions, gamma-ray bursts, and tidal disruption events, many of which feature a characteristic UV afterglow preceding the optical flare. These targets are generally followed up through world-wide campaigns across multiple wavelengths from gamma rays to radio. Although multiwavelength photometric observations can reveal a wealth of information, spectroscopic follow up has proven to be essential in confirming the types of events and understanding the physical properties of the progenitor systems. As of now, most of the spectroscopic follow up of transients is conducted in the optical or through serendipitous observations from the HST spectrographs. A dedicated UV spectrograph with a modest aperture and spectral resolution can be a good starting point to carry out follow up observations of interesting events.

In recent years, dwarf stars of M and K spectral type have emerged as the most promising targets for detection of Earth-like exoplanets. The atmospheric chemistry of these planets is essentially dependent on the stellar EUV and FUV radiation field. The flaring of low mass stars leads to a rapid increase in the EUV and FUV irradiance on the planetary atmosphere that can be orders of magnitude more intense than the Earth-Sun irradiance. The effect of this flaring on the habitability of these exoplanets is the subject of extensive modeling, but the lack of data leaves the results of these models unconstrained. Another critical science case in the FUV is the characterization of stellar atmospheres, with the aim of assessing the habitability of the planet atmosphere. Planet atmospheres are reliable indicators of habitable conditions and signs of life on dozens of potentially habitable worlds beyond our Solar System too. The rate of high energy flares in UV affects the atmospheric chemistry of the planets and can affect the presence or absence of liquid water and other biosignature gases. As some of the biosignature species can also be produced by photochemical effects of the EUV and FUV radiation, characterization of the stellar spectrum in UV is essential to identify the actual sources of such biomarkers. Some of the brightest airglow lines of the planet atmospheres are the Lyman series lines seen up to the Lyman limit at 912 Å. Ionized Oxygen and Nitrogen

oxides lines also appear as a significant feature in airglow spectrum in FUV range. FUV observations can bring a wealth of data on the atmospheric composition and surface conditions of planets in the habitable zones of a variety of stars. In addition, FUV observations can help constrain the models of the hydrodynamic escape of nearby transiting hot Jupiters as the CUTE mission (Fleming et al., 2018) proposes to do in the NUV.

5.3.2 Instrument Design

Instrument type	Long-slit imaging spectrograph
Telescope type	Off-axis parabola
Field of view	$4^\circ \times 1'$
Aperture diameter	250 mm x 100 mm (rectangular)
Focal length	175 mm
Operating bandwidth	90 – 180 nm
Slit size	12.5 mm x 50 µm
Grating type	Holographically ruled toroidal
Grating line density	2200 lines/mm
Grating dimensions	35×35 mm
Detector type	MCP with Gallium Nitride coating
Detector dimater	40mm
MCP Pore size	$20\,\mu$m
Anode type	Cross trip
Detector resolution	2048×2048
Spatial resolution	$\sim 13''$
Spectral resolution	0.65 Å (point sources), 1.2Å (extended sources)
Peak effective area	11.5 cm^2
Sensitivity	15 AB (with SNR of 5 in 1200s exposure)
Weight	$\sim$ 10 kg
Dimension (L × W× H)	$300 \times 200 \times 100$ mm

Table 5.1: Summary of instrument parameters of SING

The spectrograph will have moderate angular and spectral resolution and will be optimized to observe extended sources. We have the necessary combi-

nation of field of view and sensitivity to resolve many of the unknown effects in these extended objects. Our most compelling science drivers require a spectral resolution of 1 Å with a spatial resolution better than 13″ over the wavelength range from 900 – 1800 Å. We have achieved this through an off-axis spectrograph with a rectangular mirror coated with Silicon Carbide (SiC) and a holographically ruled diffraction grating (Table. 5.1).

The optical design of SING is capable of providing a moderate spectral resolution (R $\sim$ 1200 for extended sources and R $\sim$ 1800 for point sources) and a high peak effective area (12^2) in the 900 to 1800 Å FUV spectral bandpass. The optical design is a two-bounce system based on previously flown Far UV instruments on missions such as FUSE and ALICE (UV spectrometer onboard ROSETTA and New-Horizons missions). One of the main challenges in achieving and maintaining a high throughput was the low reflectivity of SiC coatings used to extend the spectral coverage to 900 Å. This implied we use a minimum number of elements and reflections in the optical system. To effectively utilize the space available in a 6U CubeSat, we are employing a rectangular mirror which can give almost three times the effective area of a circular mirror that fits the same volume.

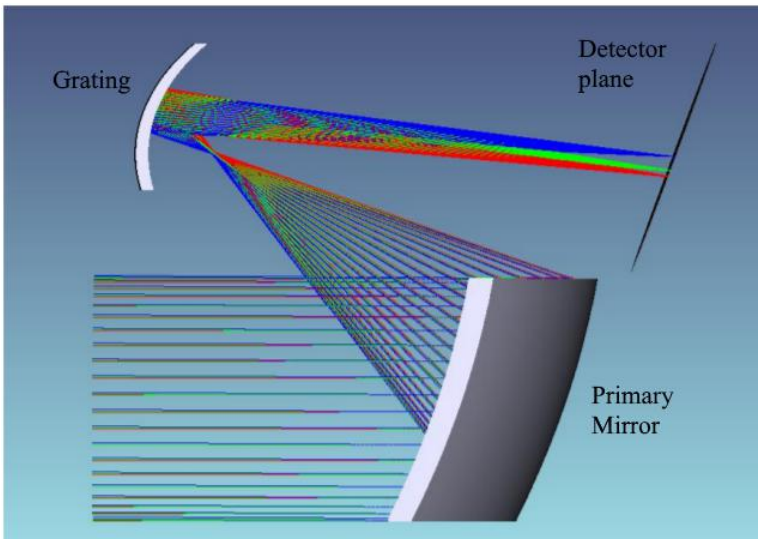

Figure 5.7: Optical layout of SING

The FUV telescope consists of a normal-incidence, off-axis parabolic pri-

mary mirror with a long slit located at its focus. The focal length of the primary mirror is 175 mm, and an off-axis angle of $\sim 5.5°$. At the focal plane, 80% of the light in the point spread function (PSF) falls within a circle of diameter $15''$. A long slit of 100 µm $\times$ 25 mm ($1' \times 4°$) at the focus of the telescope enables us to study the extended sources. This would also act as the optical entrance aperture for the spectrograph.

We have designed a Rowland circle spectrograph with an aberration corrected holographically-ruled grating. This grating helps to minimize astigmatism typically encountered in a Rowland system. The slit, grating, and the detector are arranged on this normal incidence Rowland circle. Light from the diverging telescope beam passes through the slit at the focal plane and enters the spectrograph cavity. The grating is a 30 mm square aperture with a radius of curvature of 1652 mm. The holographic recording parameters were optimized to reduce astigmatism while maintaining resolution. The characteristic groove densities would be 2200 grooves/mm to give a linear dispersion of 1.2 Å (for extended sources) and 0.65 Å (for point sources) per resolution element of two pixels. This resolution is desired to cleanly separate the OVI doublet (1032/1038 Å) and the CIV doublet (1548/1551 Å). The primary mirror is made of low thermal expansion materials such as Zerodur with an SiC coating over it, to ensure a uniform reflectivity of 40% over the entire FUV bandpass. The grating will also employ a coating of SiC.

The preliminary optical design is shown in Fig. 5.7 and the optical performance is illustrated as a spot diagram in Fig. 5.8.

Our detector is similar to the MCP based photon counting detector that was flown on the ORFEUS mission, designed at the University of Tübingen. The detector has 2048 $\times$ 2048 resolution elements with a pixel size of 20 μm. A Cs-activated photoactive layer of GaN, operated in semitransparent mode shall improve the sensitivity of the instrument by a factor of six as compared to traditional CsI or KBr photocathodes. As there are no suitable window materials in the FUV below the MgF_2 cut off at 1150 Å, we are using an open-faced detector with the photocathode deposited directly on the MCP.

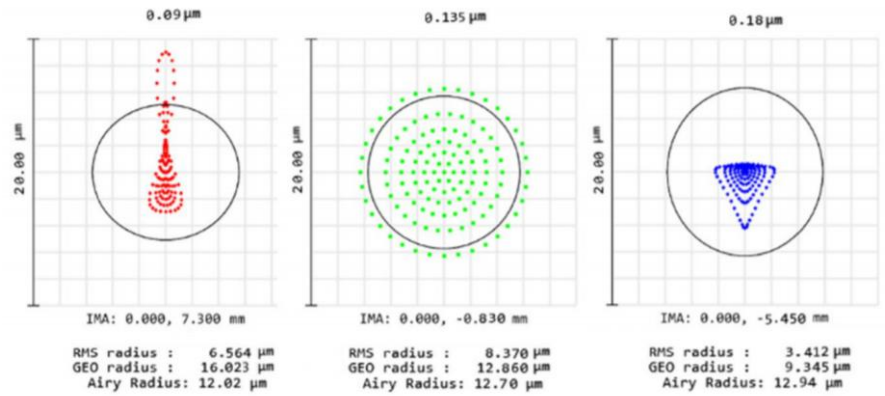

Figure 5.8: Optical performance of SING

The intensifier is a stack of two long-life MCPs capable of giving a gain of up to 10^6. The electron cloud from MCP is accelerated towards a cross strip anode (64 strips in the X direction and 64 strips in the Y direction), which is then amplified to be readable by the front-end electronics. This amplification is done by the BEETLE chip, an ASIC with 128 charge amplifiers developed for the Large Hadron Collider experiment (Löchner and Schmelling, 2006). The output of the BEETLE chip is converted into digital signals by 4 ADCs and sent to the digital processing unit, a Virtex-5 FPGA. The implemented centroiding algorithm will calculate the center of the charge cloud and store it as one event in the corresponding pixel of the image.

The SING effective area can be estimated as the product of the collecting area, grating efficiency, quantum efficiency of the detector, and the reflectivity of each optical surface. Assuming a 40% reflectivity for the SiC coated mirror and grating, a 50% grating efficiency and 60% QE for the GaN photocathode, the effective area plot is as given in Fig. 5.9.

From Fig. 5.9 we can see that the instrument has a peak effective area of 11.5 cm^2 at 1100 Å and a minimum effective area of 6 cm^2 in 900 – 1800 Å . We have also estimated the limiting flux that can be detected by the instrument, as a function of the wavelength as shown in Fig. 5.9

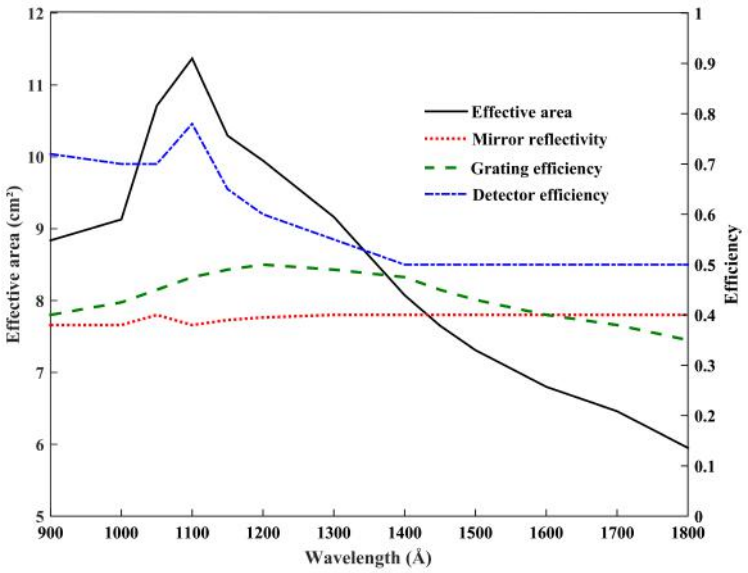

Figure 5.9: Projected effective area of SING. The left y-axis corresponds to area in cm^2 and the solid black line denotes the effective area across the bandpass. The right y-axis shows the efficiency, with the efficiency of the mirrors, grating, and detector are denoted by the red dots, green dashes and the blue dot-dashes respectively.

5.4 Future work

We have completed the preliminary optical design of the system and are in the process of finalizing the manufacturers for the optomechanical components. The lab model of the detector is fabricated and calibrated at Tübingen. We will work in collaboration with the University of Tübingen to fabricate the vacuum enclosure for the detector and the completed instrument.

Another challenge is to complete the scattering analysis and devise strategies to minimize the scattered light. This is especially crucial as the wavelength region includes the Lyman-α at 1216 Å which contributes to large geocoronal scattering. We will incorporate the methods used in FUSE and planetary missions such as ALICE, wherever possible.

The instrument will be calibrated at the MGKML at the CREST campus of IIA. This facility was used for the integration, characterization, and calibration of the UVIT instrument (Kumar et al., 2012). The facility is equipped with a class 1000 clean room which also houses a laminar flow table to provide

a class 100 environment. We will be adapting procedures from UVIT and LUCI calibrations, using equipment from the UVIT and Aditya programs. The complete instrument will be stored in a sealed container purged with ultra-clean nitrogen after final assembly.

Chapter 6

Summary and Future Work

6.1 Summary and Conclusions

The thesis deals with the development of detectors for various space and balloon missions. We are building compact UV payloads using off-the-shelf components, to further study some of the less explored science cases in the UV. We have given an overview of the scientific prospects of these observations and a summary of the current and previous missions from balloon, rocket, and satellite platforms. We briefly describe the types of existing detector technologies along with their merits and demerits for our applications.

Chapter 2 deals with the hardware and software development of our detector of choice: an MCP-based photon counting detector with a CMOS sensor as the readout. We describe the components that we have chosen and the reasoning behind them, as well as the hardware implementation. We also explain the simulations and FPGA implementation of the real-time data acquisition and centroiding algorithms that we have developed. We also report on the tests and calibrations that conducted on the laboratory detector. Based on the performance of the prototype detector, we have made a number of modifications. The first one is to replace the current relay optics to a fiber optic based system. This is done to minimize the aberrations. Another issue with

the detector is the large mismatch between the MCP and CMOS diameters, which introduces a large number of aberrations. We have solved this by using an image sensor with higher dimensions and higher pixel size. This has also helped us improve the performance, as the new CMOS incorporates high-speed SERDES channels that have ultimately improved the temporal resolution from 33 ms to 2 ms.

The first testing platform for the detector is a couple of balloon payloads. We describe them in Chapter 3, along with an overview of the high altitude balloon experiments being conducted in IIA. We describe the necessary components, launch procedures, and scientific motives of the balloon program. The first balloon payload is a near UV spectrograph to observe solar system objects and atmospheric airglow lines. The second instrument is a lens-based wide field imager for transient observations. We have briefly described the scientific objectives and optomechanical design of both the systems. The instruments have been assembled and the final calibrations are being carried out. We are talking to the National Balloon Facility (NBF), TIFR for the launch dates, as these instruments are heavier than what is permitted for our balloon program. Chapter 3 also briefly describes a 6U CubeSat spectrograph (NUVIS), for which we have completed the preliminary optomechanical design.

Chapter 4 describes a CubeSat imager, PIONS, which is a wide field, reflecting telescope that we have developed in collaboration with PES University in Bangalore. We have described the science objectives, optomechanical design, detector details, and spacecraft interface details. The payload is currently in the assembly and calibration stage. We are in contact with PES and ISRO on finalizing the launch date and will be commencing the satellite integration and environmental tests soon.

Chapter 5 describes the development of FUV instrumentation, with the first half describing the steps taken toward developing an FUV detector in-house. We have deposited and analyzed alkali halide photocathodes of varying thickness for their performance and will be assembling them with the MCP in a sealed housing. The second half of the chapter describes the development

of a UV spectrograph with bandpass up to 900 Åto look at extended objects. The instrument is in the design phase currently, with the laboratory model detector being tested at the University of Tübingen.

6.2 Future Work

6.2.1 Flight testing of payloads on TIFR balloon platform

One of the future works is the testing of our near UV payloads on the TIFR balloon platform. We are planning to use the TIFR facility for our astronomical observations, as they use zero pressure balloons that can give a float time of around 5 hours at an altitude of 40-50 km. The balloons will be floating in a relatively less turbulent region of the stratosphere, giving us the pointing stability to conduct meaningful observations. This is not possible from Bangalore, due to our proximity to the ocean.

We have fabricated a larger version of our pointing system as described by Nirmal et al. (2016), which can support the weight of the NUV spectrograph and the WiFI imager. At present, the stability of pointing is within $\pm 0.28°$, mainly because our balloons cannot achieve stable floating in the stratosphere and due to the large winds at lower altitudes. Such winds are not present in the upper regions of the stratosphere where payloads are known to be stable and floating, and we expect the pointing accuracy and tracking stability of our system to be similar to those on the ground. We are exploring several ways to further improve the system performance by using better sensors and servomotors with finer steps. We have also developed a star-sensor (Sarpotdar et al., 2017) with a resolution of $30''$ to be integrated into the pointing system for fine sensing, as shown in Fig. 6.1.

To mount the spectrograph, we will place the primary mirror on the pointing system with the fiber at the prime focus as shown in Fig.6.1. The mirror and the fiber will have two-axis pointing correction, as provided by the star

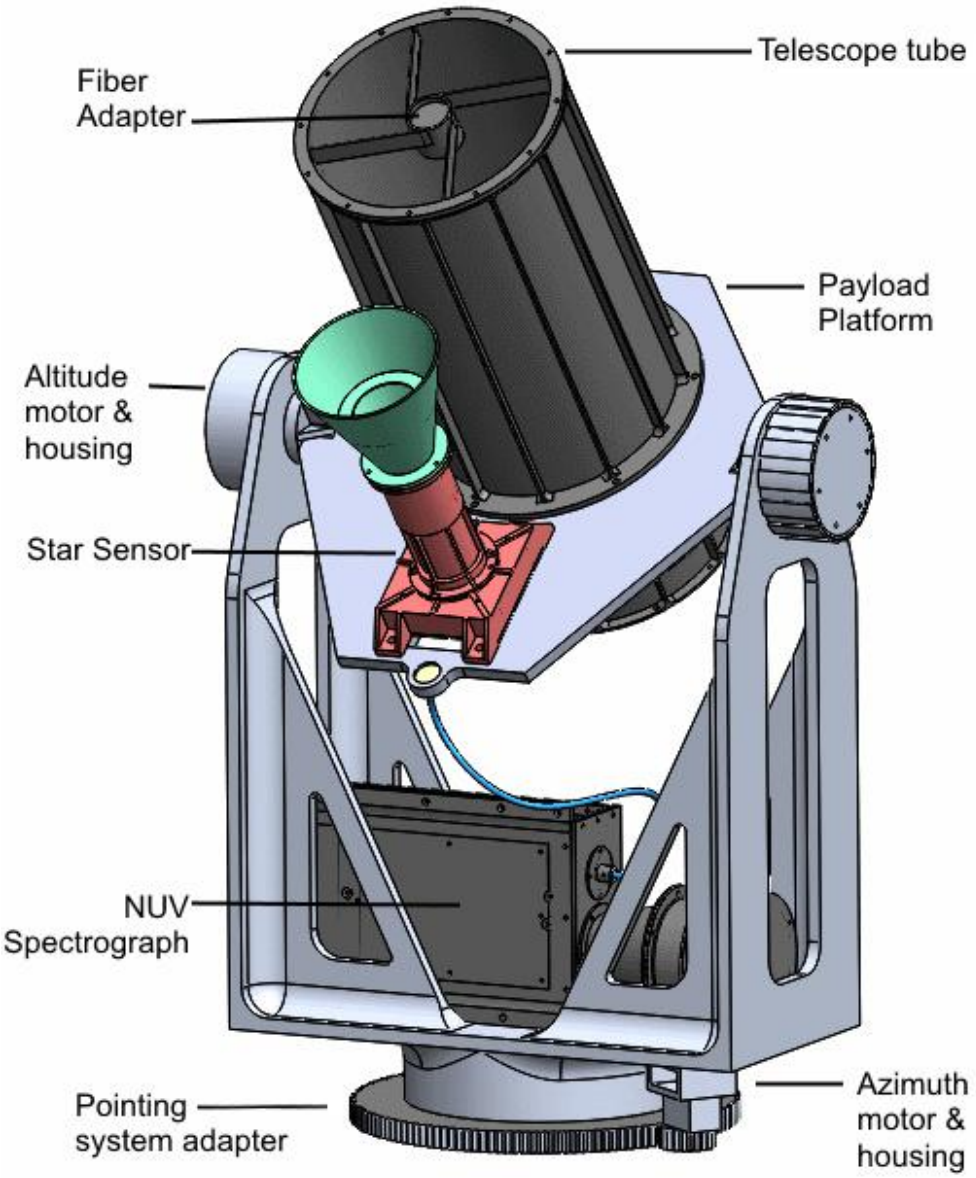

Figure 6.1: CAD drawing of the TIFR balloon payload with spectrograph. The fiber is mounted at the prime focus of the mirror, which is fixed on the altitude control platform. The rest of the system is mounted on the main platform with azimuth control.

sensor and attitude sensor. The spectrograph will be mounted at the bottom plate as shown for better mechanical stability. For imaging observations, we will be mounting the WiFI telescope on the pointing system with the help of an L-plate at its center of gravity. We have tested the pointing system with

similar mass dummies to ensure that even for larger weights the pointing can be achieved.

6.2.2 Environmental tests and development of data pipeline for PIONS

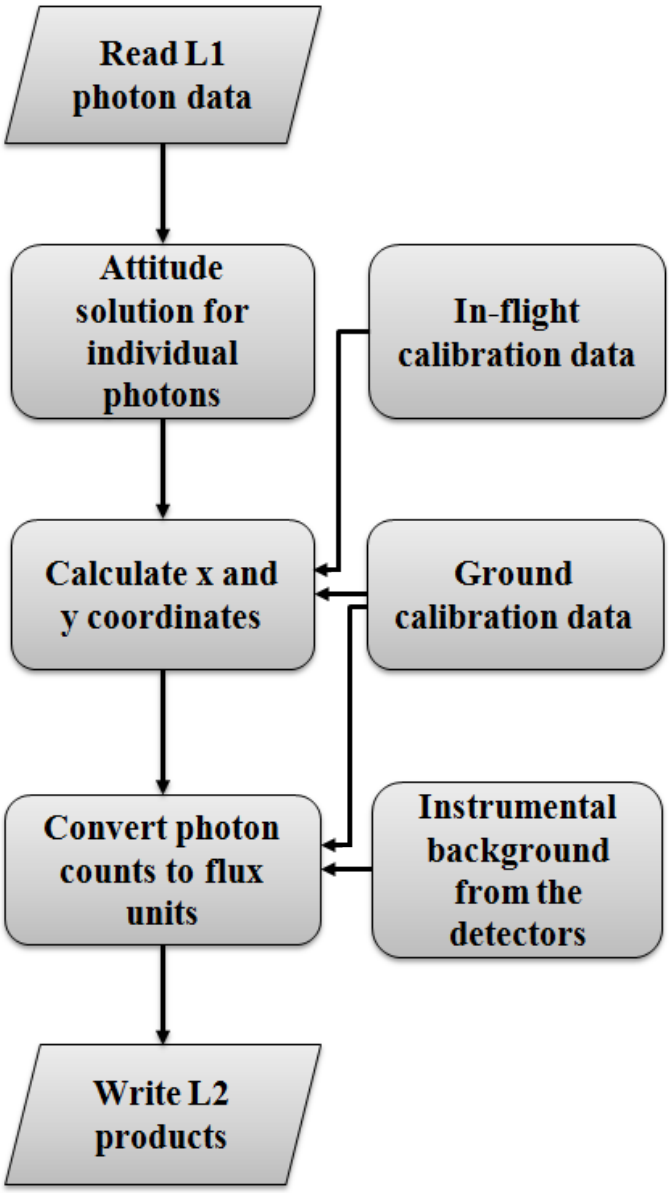

Figure 6.2: Flowchart of the PIONS pipeline

We are carrying out the optical alignment and calibration of the PIONS

instrument at the M. G. K. Menon laboratory. We will employ the procedures and techniques as explained in Mathew et al. (2018b) for the assembly and calibration of LUCI (Mathew et al., 2017). We use a theodolite for the coarse alignment, while the fine adjustments are done with a Zygo interferometer. The assembly of an F4 Newtonian telescope and monochromator is used for collimated light. The calibration steps will include the estimation of system throughput (effective area) and the optical performance (plate scale and point spread function). We will use the collimated light at 1 nm intervals, along with NIST calibrated photodiodes and SBIG cameras for the effective area measurements. The optical performance will be estimated by imaging a set of pinhole masks of varying sizes from different points in the field.

Once the ground-calibration and qualification of the payload are completed, we plan to commence the environmental tests. These will be conducted for the completed payload to minimize the test facilities and ground support equipment (GSEs) required. The carrier and instrument will undergo testing for EMI/EMC, acoustics, mass properties, vibration, thermal balance/thermal vacuum, and magnetic calibration.

Being a UV telescope, PIONS is extremely sensitive to contamination. The UVIT and LUCI missions tackled this problem with a one-time opening door. The door will be closed during the launch and opens after proper outgassing in the orbit. The design and the opening mechanism will be based on the existing systems on UVIT and LUCI.

Another important task for the payload is the development of the data pipeline and in-flight calibration techniques. The data produced by PIONS consist of the photon event lists logged during the observations. The data are registered as individual photons on the detector which will be assembled into a data stream containing the X-Y position and pulse height and transmitted to the ground. Time tags will be inserted at periodic intervals in the data, but are negligible in size compared to photon data. Assuming 20 minutes of observing time per orbit and an observation time of 12 hours at night, the data volume for the instrument is estimated to be $\sim$ 32 MB per day. We plan to

implement further data compression algorithms to reduce the data volume to around 5-10 MB/day.

After receiving at the ground station, an automated pipeline will convert the photon list into a 2-d image with the steps shown in Fig. 6.2. The pipeline software will draw on the previous software developed at IIA for missions such as Tauvex (Mohan, 2008) and UVIT (Murthy et al., 2017).

The photometric calibration of the instrument will also follow the procedures established by previous UV space missions such as HST (Bohlin, 1986), GALEX (Morrissey et al., 2007), and UVIT (Rahna et al., 2017). We will use a set of well studied standard stars, such as the UV-bright white dwarfs LB227 and HZ4, for the in-flight calibration of the instrument.

6.2.3 Development of technologies for future Far UV missions

Another major task for the future is the development of technologies for the fabrication of the far ultraviolet (912 - 1800 Å) CubeSat described in chapter 5. The FUV is one of the poorly understood bandpasses in the EM spectrum mainly due to technical limitations, especially the low reflectivity of mirror coatings.

The primary risks that our design will have to overcome is the low reflectivity of existing Silicon Carbide coatings and the contamination due to humidity and hydrocarbons. Development of environmentally resistant mirror coatings is essential to ensure good sensitivity for future missions. As a critical component, we plan to explore high-performance mirror coatings, that are alternatives to the SiC and can give good reflectivity all the way down to the Lyman limit. It is especially urgent for smaller missions such as SING, where the tradeoff between the limited bandwidth (> 1050 Å) of current LiF coatings and the low reflectivity of conventional SiC coatings significantly limits their scientific potential. Although Aluminum is capable of providing good reflectivity up to wavelengths as short as 900 Å, its reflectivity in UV is reduced by the

formation of an Aluminum Oxide layer upon atmospheric exposure. For wavelengths above 1200 Å, a thin MgF_2 protective coating is used. However, below 1200 Å, the reflectivity of MgF_2 drops significantly. Lithium Fluoride (LiF) coatings can provide good reflectivity up to 1000 Å. But as it is hygroscopic, we need to limit its exposure to water vapor. There are two ways to tackle this problem: one is to design a sealed spacecraft housing and purge it with dry Nitrogen to control the humidity. But this is difficult to implement for large missions. Even for smaller satellites such as CubeSats, maintaining the dry environment during the entire assembly, integration, and test phases is risky and extremely difficult. The second option to protect LiF coated mirrors is to deposit a thin film on top of the LiF. This is done with materials such as AlF_3 or MgF_2 and the film is made very thin, of the order of tens of Angstroms, to not affect the short wavelength performance (Fleming et al., 2017; Quijada et al., 2017).

The second key challenge is the development of sensitive and reliable microchannel plate (MCP) detectors (Siegmund et al., 2017). Carrying out high-precision ultraviolet astronomy across such a wide range of sources requires detector systems working below the atmospheric cut-off (900 – 4000 Å) with low-noise and/or photon-counting capability, high quantum detection efficiency, large format size, and high temporal resolution. In the shorter wavelengths, there is a lack of suitable materials with good transmission to be used as a protective window to the photocathode. This means that either the detector has to be protected from humidity and other contaminants, or we have to identify materials that are resilient to atmospheric exposure. We plan to test state-of-the-art Gallium Nitride (GaN) photocathodes with high quantum efficiency ($\sim 60\%$) in the SING bandpass, which is not possible to be achieved with traditional alkali halides across the 900 - 1800 Å region (Siegmund et al., 2008; Ulmer et al., 2001). To preserve the QE in LUV, we have to employ an open-faced configuration which will be kept in a sealed housing.

The development of a hermetically sealed spacecraft housing is another critical task for SING, as we are employing windowless detectors with a GaN

photocathode. It shows a lifetime of the order of seconds when exposed, as compared to a few minutes for alkali halide photocathodes. As there are already a number of planetary missions covering the LUV region, it will be interesting to adapt the existing sealing techniques to suit a CubeSat structure. The housing will be designed, fabricated, and tested to ensure that the exposed components are not contaminated. We plan to work in collaboration with the University of Tübingen, to develop the housing for the detector for use during the ground-based tests. We will also develop a sealed enclosure for the payload, to be used once the integration and calibration are complete.

Bibliography

Ambily, S., Mathew, J., Sarpotdar, M., et al. 2018, "PIONS: a CubeSat imager to observe variable UV sources", *Proc. SPIE*, 10699, 106993E

Ambily, S., Sarpotdar, M., Mathew, J., et al. 2017, "Development of Data Acquisition Methods for an FPGA-Based Photon Counting Detector", *J. of Astron. Instr.*, 6, 1750002

Austin, D. R., Witting, T., and Walmsley, I. A., 2009, "Broadband astigmatism-free Czerny-Turner imaging spectrometer using spherical mirrors," *Appl. Opt.*, 48, 19

Bellis, J. G., Bone, D. A., & Fordham, J. L. A. 1991, "A new real time centroiding technique for photon counting detectors", *Pub. Astron. Soc. Pac.*, 103, 253

Blair, W. P., Sankrit, R., & Tulin, S. 2002, "Far Ultraviolet Spectroscopic Explorer and Hopkins Ultraviolet Telescope Observations of Radiative Shocks in the Cygnus Loop", *Astrophys. J. Suppl.*, 140, 2

Boggess, A., Carr, F. A., Evans, D. C., et al. 1978, "The IUE spacecraft and instrumentation", *Nature*, 275, 372

Bohlin, R. C. 1986, "The ultraviolet calibration of the Hubble Space Telescope. I - Secondary standards of absolute ultraviolet flux and the recalibration of IUE", *Astrophys. J.*, 308, 1001

Boksenberg, A., Evans, R. G., Fowler, R. G., et al. 1973, "The ultra-violet sky-survey telescope in the TD-IA satellite.", *Mon. Not. R. Astron. Soc.*, 163, 291

Bolcar, M. R., Balasubramanian, K., Crooke, J., et al. 2016, "Technology gap assessment for a future large-aperture ultraviolet-optical-infrared space telescope", *J. Astron. Tel. Instr. Sys.*, 2, 041209

Bolcar, M. R., Feinberg, L., France, K., et al. 2016, "Initial technology assessment for the Large-Aperture UV-Optical-Infrared (LUVOIR) mission concept study", *Proc. SPIE*, 9904, 99040J

Bonanno, G., Belluso, M., Cali, A., et al. 2001, "Photon Counting system based on intensified CMOS-APS PC-lAPS", *Proc. SPIE*, 4498, 173

Borucki, W. J., Koch, D., Basri, G., et al. 2010, "Kepler Planet-Detection Mission: Introduction and First Results", *Science*, 327, 977

Bowyer, S., & Malina, R. F. 1991, "The Extreme Ultraviolet Explorer Mission", Extreme Ultraviolet Astronomy, 397

Bowyer, C. S., Field, G. B., & Mack, J. E. 1968, "Detection of an Anisotropic Soft X-ray Background Flux", *Nature*, 217, 32

Broadfoot, A. L., Sandel, B. R., Shemansky, D. E., et al. 1977, "Ultraviolet spectrometer experiment for the Voyager mission", *Space Sci. Rev.,*, 21, 183

Brosch, N., Davies, J., Festou, M. C., & Gérard, J. 2006, "A View to the Future: Ultraviolet Studies of the Solar System", *Astrophys. Space Sci.*, 303, 1

Brosch, N., Balabanov, V. & Behar, E. 2014, "Small observatories for the UV", *Astrophys. Space Sci.*, 354, 205

Byram, E. T., Chubb, T. A., Friedman, H., & Kupperian, J. E., Jr. 1957, "Rocket observations of extraterrestrial far-ultraviolet radiation", *Astron. J.*, 62, 9

Cabrera, B., Clarke, R. M., Colling, P., et al. 1998, "Detection of single infrared, optical, and ultraviolet photons using superconducting transition edge sensors", *App. Phy. Let.*, 73, 735

Carruthers, G. R. 1968, "Far-Ultraviolet Spectroscopy and Photometry of Some Early-Type Stars", *Astrophys. J.*, 151, 269

Chakrabarti, S., Mendillo, C. B., Cook, T. A., et al. 2016, "Planet Imaging Coronagraphic Technology Using a Reconfigurable Experimental Base (PICTURE-B): The Second in the Series of Suborbital Exoplanet Experiments", *J. of Astron. Instr.*, 5, 1640004-595

Cenko, S. B., Krimm, H. A., Horesh, A., et al. 2012, "Swift J2058.4+0516: Discovery of a Possible Second Relativistic Tidal Disruption Flare?", *Astrophys. J.*, 753, 77

Cockell, C. S., Bush, T., Bryce, C., et al. 2016, "Habitability: A Review", Astrobiology, 16, 89

Code, A. D., Houck, T. E., McNall, J. F., Bless, R. C., & Lillie, C. F. 1970, "Ultraviolet Photometry from the Orbiting Astronomical Observatory. I. Instrumentation and Operation", *Astrophys. J.*, 161, 377

Coleman, C. I. 1981, "Imaging detectors for the ultraviolet," *Appl. Opt.*, 20, 21

Conti, L., Barnstedt, J., Hanke, L., et al. 2018, "MCP detector development for UV space missions", *Astrophys. Space Sci.*, 363, 63

Czerny, M., and Turner, A., "Ueber den Astigmatimus bei Spiegelspektrometern," *Z. Phys.*, 61, 792 (1930).

Denvir, D. J., & Conroy, E. 2003, "Electron-multiplying CCD: the new ICCD", *Proc. SPIE*, 4796, 164

Dixon, W. V. D., Davidsen, A. F., & Ferguson, H. C. 1996, "Discovery of O VI Emission from the Galactic Corona with the Hopkins Ultraviolet Telescope", *Astrophys. J.*, 465, 288

Edelstein, J., Korpela, E. J., Adolfo, J., et al. 2006, "The SPEAR Instrument and On-Orbit Performance", *Astrophys. J. Let.*, 644, L159

Fidouh, F., Blazit, A., & Lelievre, G. 1993, "Real time photo centrold detection for photon counting and wavefront sensing cameras", *Proc. SPIE*, 1982, 288

Fleming, B. T., McCandliss, S. R., Redwine, K., et al. 2013, "Calibration and flight qualification of FORTIS", *Proc. SPIE*, 8859, 88590Q

Fleming, B. T., Quijada, M., Hennessy, J., et al. 2017, "Advanced Environmentally Resistant Lithium Fluoride Mirror Coatings for the Next-Generation of Broadband Space Observatories", Applied Optics, 56, 9941

Fleming, B. T., France, K., Nell, N., et al. 2018, "Colorado Ultraviolet Transit Experiment: a dedicated CubeSat mission to study exoplanetary mass loss and magnetic fields", *J. Astron. Tel. Instr. Sys.*, 4, 014004

France, K., Froning, C. S., Linsky, J. L., et al. 2013, "The Ultraviolet Radiation Environment around M dwarf Exoplanet Host Stars", *Astrophys. J.*, 763, 149

France, K., Hoadley, K., Fleming, B. T., et al. 2016, "The SLICE, CHESS, and SISTINE Ultraviolet Spectrographs: Rocket-Borne Instrumentation Supporting Future Astrophysics Missions", *J. of Astron. Instr.*, 5, 1640001

Ganot, N., Gal-Yam, A., Ofek, E. O., et al. "The Detection Rate of Early UV Emission from Supernovae: A Dedicated Galex/PTF Survey and Calibrated Theoretical Estimates", 2016, *Astrophys. J.*, 820, 57

Gaudi, B. S., & Habitable Exoplanet Imaging Mission Science and Technology Definition Team 2017, American Astronomical Society Meeting Abstracts , 229, 405.02

Gezari, S., Chornock, R., Rest, A., et al. 2012, "An ultraviolet-optical flare from the tidal disruption of a helium-rich stellar core", *Nature*, 485, 217

Gezari, S., Martin, D. C., Forster, K., et al. 2013, "The GALEX Time Domain Survey. I. Selection and Classification of Over a Thousand Ultraviolet Variable Sources", *Astrophys. J.*, 766, 60

Gladstone, G. R., Persyn, S. C., Eterno, J. S., et al. 2017, "The Ultraviolet Spectrograph on NASA's Juno Mission", *Space Sci. Rev.,*, 213, 447

Green, J. C., Froning, C. S., Osterman, S., et al. 2012, "The Cosmic Origins Spectrograph", *Astrophys. J.*, 744, 60

Hamden, E. T., Greer, F., Hoenk, M. E., et al. 2011, "Ultraviolet antireflection coatings for use in silicon detector design", *Appl. Opt.*, 50, 4180

Hennessy, J., Balasubramanian, K., Moore, C. S., et al. 2016, "Performance and prospects of far ultraviolet aluminum mirrors protected by atomic layer deposition", *J. Astron. Tel. Instr. Sys.*, 2, 041206

Hibbitts, C. A., Young, E., Kremic, T. and Landis, R., "Science measurements and instruments for a planetary science stratospheric balloon platform", *Aerospace Conference, IEEE, Big Sky, MT*, pp. 1-9 (2013).

Hutchings, J. B., Postma, J., Asquin, D., & Leahy, D. 2007, "Photon Event Centroiding with UV Photon-counting Detectors", *Pub. Astron. Soc. Pac.*, 119, 1152

Ivezić, Ž., Kahn, S. M., Tyson, J. A., et al. 2008, "LSST: from Science Drivers to Reference Design and Anticipated Data Products", arXiv:0805.2366

Jammal, N., Rai, R., Triloki, & Singh, B. K. 2018, "Structural and optical properties of CsI thin films: Influence of film thickness and humidity", *Physica B Condensed Matter*, 546, 21

Jenkins, E. B., & Meloy, D. A. 1974, "A survey with Copernicus of interstellar O VI absorption", *Astrophys. J. Let.*, 193, L121

Johnson, J. 2008, "Selection of Materials for UV Optics", *OPTI521*, 12, 1

Joseph, C. L., Argabright, ",. S., Abraham, J., et al. 1995, "Performance Results of the STIS Flight MAMA Detectors", *Proc. SPIE*, 2551, 248

Joseph, C. L. 1995, "UV Image Sensors and Associated Technologies", *Exp. Astron.*, 6, 97

Kaaret, P. 2017, "HaloSat - A CubeSat to Study the Hot Galactic Halo", American Astronomical Society Meeting Abstracts, 229, 328.03

Kaiser, N., Aussel, H., Burke, B. E., et al. 2002, "Pan-STARRS: A Large Synoptic Survey Telescope Array", *Proc. SPIE*, 4836, 154

Kaltenegger, L., Traub, W. A., & Jucks, K. W. 2007, "Spectral Evolution of an Earth-Like Planet", *Astrophys. J.*, 658, 598

Kameswara Rao, N., Sutaria, F., Murthy, J., et al. 2018, "Planetary nebulae with UVIT: Far ultra-violet halo around the Bow Tie nebula (NGC 40)", *Astron. Astrophys.*, 609, L1

Kameswara Rao, N., De Marco, O., Krishna, S., et al. 2018, "Planetary Nebulae with UVIT II: Revelations from FUV vision of Butterfly Nebula NGC 6302", arXiv:1810.02217

Kimble, R. A., Abraham, J., Argabright, V. S., et al. 1999, "In-flight performance of the MAMA detectors on the Space Telescope Imaging Spectrograph", *Proc. SPIE*, 3764, 209

Kimble, R. A., Pain, B., Ortiz, M., et al. 2003, "A high-speed event-driven active pixel sensor readout for photon-counting microchannel plate detectors", *Proc. SPIE*, 4854, 203

Knapp, M., & Seager, S. 2015, "ASTERIA: A CubeSat for Exoplanet Transit and Stellar Photometry", AAS/Division for Extreme Solar Systems Abstracts, 3, 106.08

Kouveliotou, C., Agol, E., Batalha, N., et al. 2014,", "Enduring Quests-Daring Visions (NASA Astrophysics in the Next Three Decades)", arXiv:1401.3741

Kramer, G., Barnstedt, J., Eberhard, N., et al. 1990,", "Far and extreme ultraviolet astronomy with ORFEUS", IAU Colloq. 123: Observatories in Earth Orbit and Beyond, 166, 177

Kumar, A., Ghosh, S. K., Hutchings, J., et al. 2012, "Ultra Violet Imaging Telescope (UVIT) on ASTROSAT", *Proc. SPIE*, 8443, 84431N

Kumar, B. S., Nagendra, N., Ojha, D. K., et al. 2014, "Development of Ultra-Thin Polyethylene Balloons for High Altitude Research upto Mesosphere", *J. of Astron. Instr.*, 3, 1440002

Maiolino, R., Russell, H. R., Fabian, A. C., et al. 2017, "Star formation inside a galactic outflow", *Nature*, 544, 202

Martin, D. C., Fanson, J., Schiminovich, D., et al. 2005, "The Galaxy Evolution Explorer: A Space Ultraviolet Survey Mission", *Astrophys. J.*, 619, L1

Martin, D. C., Chang, D., Matuszewski, M., et al. 2014, "Intergalactic Medium Emission Observations with the Cosmic Web Imager. I. The Circum-QSO Medium of QSO 1549+19, and Evidence for a Filamentary Gas Inflow", *Astrophys. J.*, 786, 106

Mason, K. O., Breeveld, A., Much, R., et al. 2001, "The XMM-Newton optical/UV monitor telescope", *Astron. Astrophys.*, 365, L36

Mathew, J., Prakash, A., Sarpotdar, M., et al. 2017, "Prospect for UV observations from the Moon. II. Instrumental Design of an Ultraviolet Imager LUCI", *Astrophys. Space Sci.*, 362, 37

Mathew, J., Ambily, S., Prakash, A., et al. 2018, "Wide-field Ultraviolet Imager for Astronomical Transient Studies", *Exp. Astron.*, 45, 201

Mathew, J., Nair, B. G., Sriram, S., et al. 2018, "Opto-mechanical assembly and ground calibration of LUCI", Space Telescopes and Instrumentation 2018: Ultraviolet to Gamma Ray, 10699, 106992V

McClintock, W. E., Schneider, N. M., Holsclaw, G. M., et al. 2015, "The Imaging Ultraviolet Spectrograph (IUVS) for the MAVEN Mission", *Space Sci. Rev.,*, 195, 75

McPhate, J. B., Siegmund, O. H. W., Gaines, G. A., Vallerga, J. V., Hull, J. S., 2000, "Cosmic Origins Spectograph FUV detector", *Proc. SPIE*, 4139, 4139

Milliard, B., Martin, D. C., Schiminovich, D., et al. 2010, "FIREBALL: the Faint Intergalactic medium Redshifted Emission Balloon: overview and first science flight results", *Proc. SPIE*, 7732, 773205

Mohan, R. 2008, "TAUVEX observatory activities - Software tools", *Bulletin of the Astronomical Society of India Proceedings*, 25, 77

Moos, H. W., Cash, W. C., Cowie, L. L., et al. 2000, "Overview of the Far Ultraviolet Spectroscopic Explorer Mission", *Astrophys. J. Let.*, 538, L1

Morrissey, P., Conrow, T., Barlow, T. et al., 2007, "The on-orbit performance of the galaxy evolution explorer", *Astrophys. J. Suppl.*, 173, 682

Murthy, J., Rahna, P. T., Sutaria, F., et al. 2017, "JUDE: An Ultraviolet Imaging Telescope pipeline", *Astronomy and Computing*, 20, 120

Murthy, J. 2009, "Observations of the near and far ultraviolet background", *Astrophys. Space Sci.*, 320, 21

Mushotzky, R. F., Edelson, R., Baumgartner, W., & Gandhi, P. 2011, "Kepler Observations of Rapid Optical Variability in Active Galactic Nuclei", *Astrophys. J. Let.*, 743, L12

Nikzad, S., Jewell, A. D., Hoenk, M. E., et al. 2017, "High-efficiency UV/optical/NIR detectors for large aperture telescopes and UV explorer

missions: development of and field observations with delta-doped arrays", *J. Astron. Tel. Instr. Sys.*, 3, 036002

Nikzad, S., Hoenk, M. E., Grunthaner, P. J., et al. 1994, "Delta-doped CCDs: high QE with long-term stability at UV and visible wavelengths", *Proc. SPIE*, 2198, 907

Nirmal, K., Sreejith, A. G., Mathew, J., et al. 2016, "Pointing System for the Balloon-Borne Astronomical Payloads", *J. Astron. Tel. Instr. Sys.*, 2, 047001

Nowak, M., Lacour, S., Lapeyrère, V., et al. 2016, "Reaching sub-milimag photometric precision on Beta Pictoris with a nanosat: the PicSat mission", *Proc. SPIE*, 9904, 99044L

O'Connell, R. W. 1987, "Ultraviolet detection of very low-surface-brightness objects", *Astron. J.*, 94, 876

Oke, J. B., & Gunn, J. E. 1983, "Secondary standard stars for absolute spectrophotometry", *Astrophys. J.*, 266, 713

Peacock, A., Verhoeve, P., Rando, N., et al. 1996, *Nature*, "Single optical photon detection with a superconducting tunnel junction", 381, 135

Platt, U., Perner, D., & PäTz, H. W., "Simultaneous measurement of atmospheric CH2O, O3, and NO2 by differential optical absorption", *J. Geophys. Res.*, 84, 6329 (1979).

Quijada, M. A., del Hoyo, J., Boris, D. R., & Walton, S. G. 2017, "Improved mirror coatings for use in the Lyman Ultraviolet to enhance astronomical instrument capabilities", Society of Photo-Optical Instrumentation Engineers (SPIE) Conference Series, 10398, 103980Z

Rahna, P. T., Murthy, J., Safonova, M., et al. 2017, "Investigating the in-flight performance of the UVIT payload on AstroSat", *Mon. Not. R. Astron. Soc.*, 471, 3028

Rai, R., Triloki, Singh, B. K., & Jammal, N. F. A. 2017, "Correlation between photoemissive and morphological properties of KBr thin film photocathodes", arXiv:1709.05643

Rai, R., Triloki, T., & Singh, B. K. 2016, "X-ray diffraction line profile analysis of KBr thin films", *Applied Physics A: Materials Science & Processing*, 122, 774

Rai, R., Triloki, Ghosh, N., & Singh, B. K. 2015, "Effect of humid air exposure on photoemissive and structural properties of KBr thin film photocathode", *Nucl. Instr. Meth. Phys. Res. A*, 787, 125

Rau, A., Kulkarni, S. R., Law, N. M., et al. 2009, "Exploring the Optical Transient Sky with the Palomar Transient Factory", *Pub. Astron. Soc. Pac.*, 121, 1334

Ricker, G. R., Winn, J. N., Vanderspek, R., et al. 2015, "Transiting Exoplanet Survey Satellite (TESS)", *J. Astron. Tel. Instr. Sys.*, 1, 014003

Ridden-Harper, R., Tucker, B. E., Sharp, R., Gilbert, J., & Petkovic, M. 2017, "Capability of detecting ultraviolet counterparts of gravitational waves with GLUV", *Mon. Not. R. Astron. Soc.*, 472, 4521

Roming, P. W. A., Kennedy, T. E., Mason, K. O., et al. 2005, "The Swift Ultra-Violet/Optical Telescope", *Space Sci. Rev.,*, 120, 95

Safonova, M., Mohan, R., Sreejith, A. G., & Murthy, J. 2013, "Predicting UV sky for future UV missions", *Astronomy and Computing*, 1, 46

Safonova, M., Nayaky, A., Sreejith, A. G., et al. 2016, "An Overview of High-Altitude Balloon Experiments at the Indian Institute of Astrophysics", Astronomical and Astrophysical Transactions, 29, 397

Sagiv, I., Gal-Yam, A., Ofek, E. O., et al. 2014 , "Science with a Wide-field UV Transient Explorer", *Astron. J.*, 147, 79

Sahnow, D. J., Moos, H. W., Ake, T. B., et al. 2000, "On-Orbit Performance of the Far Ultraviolet Spectroscopic Explorer Satellite", *Astrophys. J. Let.*, 538, L7.

Sankrit, R., Blair, W. P., & Raymond, J. C. 2006, "FUSE Observations of Supernova Remnants", Astrophysics in the Far Ultraviolet: Five Years of Discovery with FUSE, 348, 319

Sarpotdar, M., Mathew, J., Safonova, M., & Murthy, J. 2016, "A generic FPGA-based detector readout and real-time image processing board", *Proc. SPIE*, 9915, 99152K

Sarpotdar, M., Mathew, J., Sreejith, A. G., et al. 2017, "A software package for evaluating the performance of a star sensor operations", *Exp. Astron.*, 43, 99

Shkolnik, E. L. 2018, "On the verge of an astronomy CubeSat revolution", *Nature Astronomy*, 2, 374

Shelton, R. L. 2003, "Surprisingly Little O VI Emission Arises in the Local Bubble", *Astrophys. J.*, 589, 261

Shkolnik, E. L., Ardila, D., Barman, T., et al. 2018, "Monitoring the High-Energy Radiation Environment of Exoplanets Around Low-mass Stars with SPARCS (Star-Planet Activity Research CubeSat)", American Astronomical Society Meeting Abstracts, 231, 228.04

Shustov, B., Sachkov, M., Gómez de Castro, A. I., et al. 2011, "World space observatory-ultraviolet among UV missions of the coming years", *Astrophys. Space Sci.*, 335, 273

Siegmund, O. H. W., Welsh, B. Y., Martin, C., et al. 2004, "The GALEX mission and detectors", *Proc. SPIE*, 5488, 13

Siegmund, O. H. W., Tremsin, A. S., Vallerga, J. V., et al. 2008, "Gallium nitride photocathode development for imaging detectors," *Proc. SPIE*, 7021, 70211B

Siegmund, O. H. W., Ertley, C., Vallerga, J. V., et al. 2017, "Microchannel plate detector technology potential for LUVOIR and HabEx", *Proc. SPIE*, 10397, 1039711

Smith, A. M. 1967, "Stellar Photometry from a Satellite Vehicle", *Astrophys. J.*, 147, 158

Smith, R. M., Dekany, R. G., Bebek, C., et al. 2014, "The Zwicky transient facility observing system", *Proc. SPIE*, 9147, 914779

Spitzer, L., Jr. 1956, "On a Possible Interstellar Galactic Corona", *Astrophys. J.*, 124, 20

Sreejith, A. G., Mathew, J., Sarpotdar, M., et al. 2014, "A Raspberry Pi-Based Attitude Sensor", *J. of Astron. Instr.*, 3, 1440006

Sreejith, A. G., Safonova, M., & Murthy, J. 2015, "Near ultraviolet spectrograph for balloon platform", *Proc. SPIE*, 9654, 96540D

Sreejith, A. G., Mathew, J., Sarpotdar, M., et al. 2016, "Measurement of limb radiance and Trace Gases in UV over Tropical region by Balloon-Borne Instruments – Flight Validation and Initial Results", *Atmos. Meas. Tech. Discuss.*

Sreejith, A. G., Mathew, J., Sarpotdar, M., et al. 2016, "Balloon UV Experiments for Astronomical and Atmospheric Observations", *Proc. SPIE*9908, 99084E

Sreejith, A. G. 2017, "Studies of earth's atmosphere from space and near space", *Ph.D. Thesis*, University of Calcutta.

Stecher, T. P., & Milligan, J. E. 1962, "Stellar Spectrophotometry from above the Atmosphere", *Astrophys. J.*, 136, 1

Steidel, C. C., Erb, D. K., Shapley, A. E., et al. 2010, "The Structure and Kinematics of the Circumgalactic Medium from Far-ultraviolet Spectra of z = 2-3 Galaxies", *Astrophys. J.*, 717, 289

Stern, S. A., Slater, D. C., Scherrer, J., et al. 2008, "ALICE: The Ultraviolet Imaging Spectrograph Aboard the New Horizons Pluto-Kuiper Belt Mission", *Space Sci. Rev.,*, 140, 155

Tremsin, A. S., Vallerga, J. V., Siegmund, O. H. W., & Hull, J. S. 2003, "Centroiding algorithms and spatial resolution of photon counting detectors with cross-strip anodes", *Proc. SPIE*, 5164, 113

Triloki, Dutta, B., & Singh, B. K. 2012, "Influence of humidity on the photoemission properties and surface morphology of cesium iodide photocathode", *Nucl. Instr. Meth. Phys. Res. A*, 695, 279

Triloki, Garg, P., Rai, R., & Singh, B. K. 2014, "Structural characterization of "as-deposited" cesium iodide films studied by X-ray diffraction and transmission electron microscopy techniques", *Nucl. Instr. Meth. Phys. Res. A*, 736, 128

Triloki, Rai, R., Gupta, N., Jammal, N. F. A., & Singh, B. K. 2015, "Photoemission and optical constant measurements of a Cesium Iodide thin film photocathode", *Nucl. Instr. Meth. Phys. Res. A*, 787, 161

Triloki, Rai, R., & Singh, B. K. 2015, "Optical and structural properties of CsI thin film photocathode", *Nucl. Instr. Meth. Phys. Res. A*, 785, 70

Tumlinson, J., Aloisi, A., Kriss, G., et al. 2012, "Unique Astrophysics in the Lyman Ultraviolet", arXiv:1209.3272

Tumlinson, J., Thom, C., Werk, J. K., et al. 2013, "The COS-Halos Survey: Rationale, Design, and a Census of Circumgalactic Neutral Hydrogen", *Astrophys. J.*, 777, 59

Ulmer, M. P., Wessels, B. W., Shahedipour, F., et al. 2001, "Progress in the fabrication of GaN photocathodes", *Proc. SPIE*, 4288, 246

Ulmer, M. P., Manijeh Razeghi, Erwan Bigan, "Ultraviolet detectors for astrophysics: present and future," 1995, *Proc. SPIE*, 2397, Optoelectronic Integrated Circuit Materials, Physics, and Devices.

Uslenghi, M. C., Bonanno, G., Belluso, M., et al. 2003, "Progress on Photon Counting Intensified APS", *Proc. SPIE*, 4854, 583

Vallerga, J. V., & Siegmund, O. H. W. 2000, "2Kx2K resolution element photon counting MCP sensor with 200 kHz event rate capability", *Nucl. Instr. Meth. Phys. Res. A*, 442, 159

Vallerga, J., McPhate, J., Tremsin, A., & Siegmund, O. 2009, "The current and future capabilities of MCP based UV detectors", *Astrophys. Space Sci.*, 320, 247

Vidal-Madjar, A., Lecavelier des Etangs, A., Désert, J.-M., et al. 2003, "An extended upper atmosphere around the extrasolar planet HD209458b", *Nature*, 422, 143

Weiss, W. W., Rucinski, S. M., Moffat, A. F. J., et al. 2014, "BRITE-Constellation: Nanosatellites for precision photometry of bright stars", *Pub. Astron. Soc. Pac.*, 126, 573

Woodgate, B. E., Kimble, R. A., Bowers, C. W., et al. 1998, "The Space Telescope Imaging Spectrograph Design", *Pub. Astron. Soc. Pac.*, 110, 1183